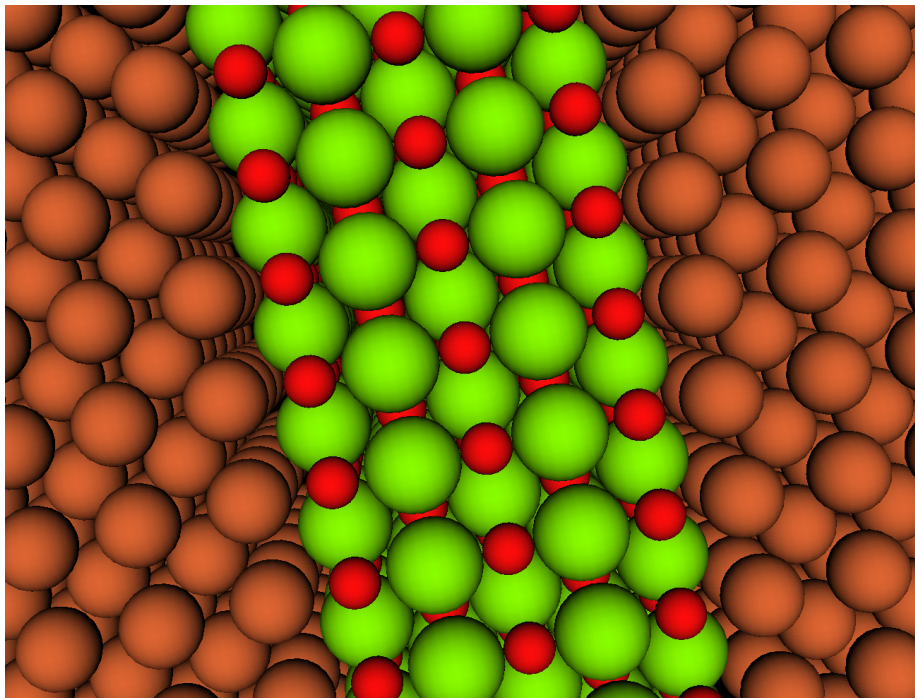


Magnetoresistance in MgO-based Magnetic Tunnel Junctions with Fe, Co, and FeCo Electrodes

Ph.D. thesis



Ph.D. Student Morten Stilling

Faculty of Science
University of Copenhagen

May 30th 2008

The title page shows the geometry of the Fe/MgO/Fe magnetic tunnel junction, consisting of five atomic layers of insulating MgO sandwiched between ferromagnetic Fe electrodes.

An online version of this thesis is available in PDF-format at <http://phd.mortenstilling.com>.

Abstract

We use spin-density functional theory and non-equilibrium Green's functions to estimate the structure and low-bias current/voltage characteristics of magnetic tunnel junctions (MTJs) consisting of five-layer MgO barriers sandwiched between Fe, Co and FeCo electrodes in both the parallel and anti-parallel magnetization configurations. The calculated tunneling magnetoresistance (TMR) decreases with increasing bias voltage in all three MTJs in the bias range considered (0–0.5 V). In the FeCo/MgO system it remains constant below $V \approx 0.3$ V. While the calculated value of the TMR is roughly a factor of 10 larger than found in experiments, the decrease in TMR with bias is in agreement with experimental observations. The tunneling mechanisms behind this bias dependence are discussed in terms of the electronic structure of the electrodes.

For my parents
— always there, always supportive

Preface

The Fe/MgO/Fe magnetic tunnel junction has received significant academic and industrial attention since the beginning of 2001 [1, 2, 3, 4]. Related systems with FeCo [5], FeCoB [6], and similar electrode materials are currently emerging in the next generation of hard disk drive read heads and novel magnetic random access memory (MRAM) devices [7, 8, 9, 10, 11].

This thesis documents the findings of first-principles studies of the spin-transport properties of such systems. Emphasis is on the tunneling mechanisms and the voltage dependence of the tunneling magnetoresistance (TMR). Magnetic tunnel junctions with MgO barriers and Fe, Co, and FeCo electrodes are studied. In the case of FeCo electrodes Co/MgO interfaces are examined.

The thesis is organized as follows.

Chapter 1 describes the motivation for this work and provides an introduction to magnetic tunnel junctions and tunneling magnetoresistance, the Julliere model of TMR in such systems, the current status of the research field, and the applications currently being developed by the industry. The chapter also discusses the objectives of the work.

Chapter 2 provides an introduction to the theory behind many-electron systems, including a discussion of the Hartree method, Hartree-Fock theory, and density functional theory. It also provides an introduction to quantum transport, including a discussion of the Landauer picture of quantum transport and an outline of a non-equilibrium Green's functions method for calculating spin-transport properties.

Chapter 3 investigates the bulk properties of the elements used in this work, and describes a benchmark study of the spin-transport properties of the Fe/MgO/Fe systems investigated in Reference [1]. The chapter also serves to introduce the conceptual framework used.

Chapter 4 describes the set up and optimization of three magnetic tunnel junctions and discusses their structural, charge redistribution, and surface magnetic properties.

Chapter 5 examines the zero-bias conductance and TMR in the three systems and discusses the tunneling mechanisms giving rise to these properties.

Chapter 6 investigates the voltage dependence of the current and the TMR and relates these to the voltage dependence of the tunneling mechanisms.

Chapter 7 summarizes, draws conclusions, and sets the work in perspective.

Chapters 1 and 2 introduce the subject and the theories used to describe physical phenomena, and Chapter 3 describes the properties of materials of interest and the generic Fe/MgO/Fe magnetic tunnel junctions analyzed in the original work [1]. Chapter 4 describes the set up and structural properties of the systems analyzed in this work, and Chapters 5 and 6 discuss the spin-transport properties of the systems. These chapters describe the main results. Finally, Chapter 7 summarizes the main results, draws conclusions, and provides perspectives.

The industrial Ph.D. project, of which this thesis is a product, has been made in collaboration with the Nano-Science Center at Copenhagen University and Atomistix. Karsten Flensberg (from the Nano-Science Center) has been university supervisor to the project and Kurt Stokbro and Jeremy Taylor (from Atomistix) have been company supervisors.

Ph.D. Student Morten Stilling
May 30th 2008

Acknowledgements

Many people have been of great help to me over the course of this Ph.D. project, and I feel very much indebted to them all. I would particularly like to thank Dr. Mera for picking me up when things looked hopeless, The Guru for lots of good advice and quite a bit of convergence help, Mister E for essential convergence help, JarJar for stepping in and stepping up, and Kurt for showing me the finish line and pushing me across.

I wish to thank Karsten Flensburg for constructive criticism and insights, and for sticking around to the end of what has been, I believe, an unusual and somewhat chaotic project.

I would like to thank Atomistix for giving me the opportunity to evolve in the direction of my choice, and for believing in me and supporting me. I am particularly grateful to Thomas Magnussen for his infinite support, encouragement, and positive energy, to Klaus Melchior for invaluable sparring and good advice, and to Jeremy Taylor for giving me a foundation from which to grow, for his coaching and sparring, and for being a mentor and a friend.

The people of Atomistix have made this time unforgettable for me, and I am grateful for the friendships offered me by my incredible colleagues. When all is said and done, the people is what I will remember.

Contents

1	Introduction	17
1.1	Motivation for thesis	17
1.2	Magnetic tunnel junctions with tunneling magnetoresistance . . .	19
1.3	The Julliere model	21
1.4	Overview of research field	22
1.5	Overview of commercial markets	25
1.6	Objective of thesis	27
1.7	Summary	27
2	Theoretical foundation	29
2.1	The many-body Schrödinger equation	29
2.2	The electronic Schrödinger equation	30
2.3	The variational principle for the energy of the ground state . . .	31
2.4	Wave function methods	31
2.4.1	The Hartree method	32
2.4.2	Hartree-Fock theory	33
2.4.3	Scaling problems associated with the wave function methods	35
2.5	Density functional theory	35
2.5.1	The Hohenberg-Kohn theorem	36
2.5.2	The Kohn-Sham equations	36
2.5.3	Approximations to DFT	38
2.5.4	Spin-dependent DFT	39
2.5.5	Reliability of DFT in describing physical properties . . .	40
2.6	DFT applied to quantum transport	40
2.6.1	The Landauer picture of quantum transport	41
2.6.2	The NEGF method for the modeling of quantum transport	44
2.6.3	Reliability of DFT in describing quantum transport . . .	46
2.7	Summary	49
3	Analyses of bulk materials and magnetic tunnel junctions	50
3.1	Analyses of bulk materials	50
3.1.1	Equations of state	51
3.1.2	Magnetic moments	53
3.1.3	Band structures	53
3.1.4	Densities of states	55
3.1.5	Electrode Bloch states with $\mathbf{k}_{\parallel} = 0$	57
3.2	Analyses of magnetic tunnel junctions	58
3.2.1	Charge redistribution and magnetic moments	59

3.2.2	Transmission spectra and transmission eigenstates	60
3.3	Summary	68
4	Structural properties of MgO-based tunnel junctions	70
4.1	Set up of three tunnel junctions	70
4.1.1	Set up of Fe/MgO tunnel junction	71
4.1.2	Set up of systems using Co and FeCo electrodes	73
4.2	Structural properties of the three systems	74
4.3	Charge redistribution and surface magnetic moments of the systems	75
4.4	Summary	76
5	Tunneling mechanisms in MgO-based tunnel junctions	77
5.1	Conductance trends of the three tunnel junctions	78
5.2	Tunneling mechanisms in the parallel configuration	80
5.3	Tunneling mechanisms in the anti-parallel configuration	84
5.4	Summary	87
6	Influence of a bias voltage in MgO-based tunnel junctions	88
6.1	Current/voltage characteristics of the three tunnel junctions . . .	89
6.2	Influence of a bias voltage in the parallel configuration	92
6.3	Influence of a bias voltage in the anti-parallel configuration . . .	92
6.4	Voltage dependence of the tunneling mechanisms	97
6.5	Summary	98
7	Conclusions and perspectives	100
7.1	Conclusions	101
7.2	Perspectives	105

Attached articles

The following articles are attached to this thesis.

- *Magnetoresistance in MgO-based tunnel junctions with Fe, Co, and FeCo electrodes*
by Morten Stilling, Héctor Mera, Davide Ricci, Søren Smidstrup, Jeremy Taylor, and Kurt Stokbro
Submitted to Physical Review B
(Reference [12])
- *First-principles Modeling of Magnetic Memory Components — Preliminary Results on the Effects of Interface Oxides*
by Morten Stilling and Kurt Stokbro
Proceedings of NSTI-Nanotech 2007, Volume 1, May 2007
(Reference [13])
- *Electronic transport in crystalline magnetotunnel junctions: effects of structural disorder*
by Morten Stilling, Kurt Stokbro, and Karsten Flensberg
Journal of Computer-Aided Materials Design, Volume 14, January 2007
(Reference [14])
- *Crystalline magnetotunnel junctions: Fe-MgO-Fe, Fe-FeOMgO-Fe and Fe-AuMgO-Au-Fe*
by Morten Stilling, Kurt Stokbro, and Karsten Flensberg
Molecular Simulation, Volume 33, Number 7, June 2007
(Reference [15])

The articles are located in the back of the thesis. (Not available in pdf version).

The coauthors of the articles hereby declare that the Ph.D. Student has been the main contributor to the work.

Kurt Stokbro	Karsten Flensberg	Héctor Mera	Davide Ricci	Søren Smidstrup	Jeremy Taylor
-----------------	----------------------	----------------	-----------------	--------------------	------------------

Who is happier than the philosopher who peruses with understanding that spacious book, which the Supreme has laid open to his intellectual faculties? The truths he discovers there are of infinite service to him. He thereby cultivates and improves his mind. He lives in peace and tranquility all his days.

- *Voltaire*

Chapter 1

Introduction

This chapter describes the motivation for the thesis and introduces the subjects of interest, including magnetic tunnel junctions, tunneling magnetoresistance (TMR), and the Julliere model of TMR in magnetic tunnel junctions. The chapter also provides an overview of the research field, commercial applications under development, and the projected markets for these. Finally, the chapter mentions the objectives of the work described in this thesis.

1.1 Motivation for thesis

Since the invention of the transistor in 1947 [16, 17, 18, 19], and particularly after the invention of the integrated circuit in 1958 [20, 21], the electronics industry has achieved remarkable results. Gordon Moore in 1965 observed an exponential increase in the number of transistors in the first five generations of integrated circuits [22] and predicted that this trend would continue for another ten years. This prediction, later known as Moore's Law, remain valid even today [23]: the latest generation of processors from Intel Corporation, introduced in 2007, incorporates 820 million transistors on a single chip, runs at a clock frequency of more than 3 GHz, and is based on manufacturing technology with a feature size of only 45 nm [24]; the next generation, targeted for production towards the end of 2008, incorporates two billion transistors! [25].

In terms of data storage, similar impressive results have been achieved. From their development in the early 1950s, magnetic core memory was used in computers until the introduction of static- and dynamic random access memory (SRAM and DRAM) in the late 1960s and early 1970s [26]. SRAM and DRAM are used in all computers today. As these memory technologies are "volatile", *i.e.* they depend on a constant power supply to maintain their data, other types of storage media, such as magnetic tapes and hard disk drives, have been and continue to be used for "permanent storage". The first hard disk drive, the IBM RAMAC from 1956, is shown in Figure 1.1.

Since the introduction of magnetoresistive (MR) read heads in hard disk drives in 1991 an annual increase in storage capacity of 60% was achieved, and with the introduction of read heads based on giant magnetoresistance (GMR) in 1997 this number accelerated to 100% [27]. The latest generation of 3.5" hard disk drives from Seagate Technologies, announced March 2008, has a capacity



Figure 1.1: The first hard disk drive, called RAMAC and introduced by IBM in 1956. The drive consisted of 50 24" disks, and had a total storage capacity of 5 megabytes and a data transfer rate of 0.0088 megabytes/second.

of 450 gigabytes and a data transfer rate of 164 megabytes/second [28].

The same technologies developed by the hard disk drive industry over the past 50 years have recently found new use in a totally new type of data storage system: magnetic random access memory (MRAM). As will be discussed later in this chapter, MRAM has the potential to become a universal memory and replace all the memory types discussed above. The technologies are also used in many other areas of science, research, and development [27], and a brand new research area called spintronics — an acronym for spin transport electronics [27] — has been developed. Technologies based on spintronics are expected to be worth hundreds of billions of dollars [29].

In recent years computer-aided materials design has become increasingly important in the continued development of data storage technologies. Due to the increasingly smaller dimensions of features experiments are becoming more expensive and more time consuming for each technology generation. Computer-aided materials design is simultaneously becoming cheaper, faster, and more capable. The hard disk drive industry is currently changing from using GMR devices in read heads to using TMR devices. This change is largely due to the phenomenological understanding of the tunneling processes in magnetic tunnel junctions developed from results of first-principles calculations [1].

At the end of this chapter, after introducing relevant subjects, we outline how we contribute to the understanding of systems relevant for the data storage and memory industries through the use of first-principles modeling of magnetic tunnel junctions.

1.2 Magnetic tunnel junctions with tunneling magnetoresistance

A system consisting of an insulating barrier sandwiched between two ferromagnetic electrodes is known as a magnetic tunnel junction. The electrodes can be made from Iron (Fe), Cobalt (Co), Iron-Cobalt (FeCo), Iron-Cobalt-Boron (FeCoB), or any other ferromagnetic alloy, and the barrier can be made from Aluminum-oxide (AlO_x), Titanium-oxide (TiO_x), Magnesium oxide (MgO), or any other insulator [10]. The electrodes can be magnetized in one of two configurations: the magnetization directions of the two electrodes can be parallel to each other (the “parallel magnetization configuration”) or they can be anti-parallel to each other (the “anti-parallel magnetization configuration”).

In such systems, illustrated in Figure 1.2, a current flows from one electrode

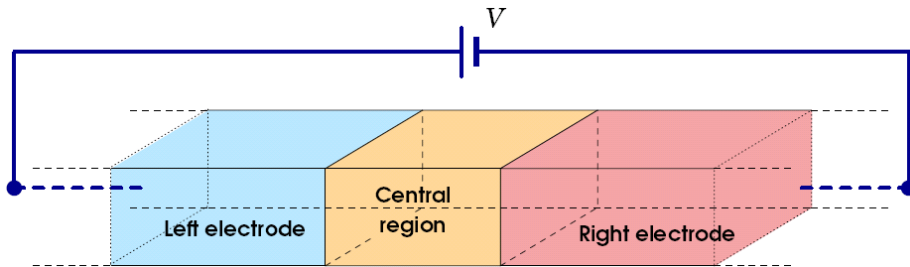


Figure 1.2: Illustration of a magnetic tunnel junction consisting of an insulating barrier sandwiched between ferromagnetic electrodes. (From Reference [30]).

to the other when a bias voltage is applied. If the applied voltage is small the relationship between the voltage and the current is assumed to be linear,

$$I(V) \approx G \cdot V \quad (1.1)$$

where G is the conductance (the inverse of the electrical resistance). In this work we shall deal with both situations where the applied bias voltage is small (the “zero-bias” regime), in which case we will calculate the conductance, and situations where it is not so small (the “finite-bias” regime), in which case we will calculate the current.

Since we use periodic boundary conditions in the plane perpendicular to the current flow in our calculations we consider the conductance or current *per area* rather than the conductance and current themselves. Throughout this thesis we will deal with the conductance density (in units of Siemens per square meter) and the current density (in units of Ampere per square meter) only, and will never discuss the conductance or current in absolute terms; we will, for convenience, use somewhat sloppy language and use the terms “conductance” and “current” in place of “conductance density” and “current density”.

For reasons to be discussed in the following section the conductance and current can depend — to a higher or lesser degree — on the magnetization configuration of the electrodes. For most magnetic tunnel junctions the conductance is higher in the case where the magnetic fields in the two electrodes are aligned parallel to each other (P) than in the case where they are aligned anti-parallel to each other (AP). We define the tunneling magnetoresistance (TMR)

as a measure of this effect,

$$\text{TMR} \equiv \frac{G_P - G_{AP}}{G_{AP}} \quad (1.2)$$

where G_P and G_{AP} are the conductances for the parallel- and anti-parallel magnetization configurations, respectively¹, or

$$\text{TMR} \equiv \frac{I_P - I_{AP}}{I_{AP}} \quad (1.3)$$

where I_P and I_{AP} are the corresponding currents.

In experiments the TMR is found by measuring magnetoresistance curves such as that shown for a Co/MgO magnetic tunnel junction in Figure 1.3. In this

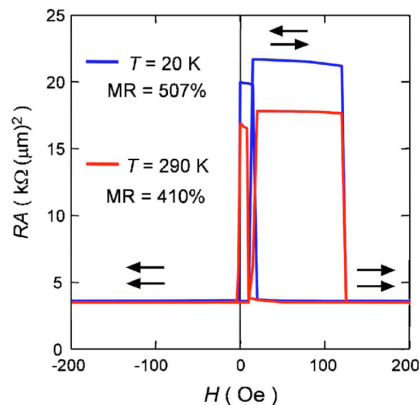


Figure 1.3: Magnetoresistance curves at a bias voltage of 10 mV for a Co/MgO magnetic tunnel junction with a barrier thickness of 2.2 nm. The magnetoresistance is approximately 410% at room temperature. (Adapted from Reference [31]).

measurement the resistance-area product, $R \cdot A$, (the inverse of the conductance density) is found to be approximately $3.5 \text{ k}\Omega \mu\text{m}^2$ in the parallel magnetization configuration at room temperature and $18 \text{ k}\Omega \mu\text{m}^2$ in the anti-parallel configuration. This results in a TMR of approximately 410%.

On a side note it can be mentioned that tunneling magnetoresistance in magnetic tunnel junctions is closely related to giant magnetoresistance (GMR) in spin valves, which is a similar effect for systems consisting of metallic barriers sandwiched between ferromagnetic electrodes. This technology has enabled the more than 30-fold increase in storage density on hard disk drives since IBM introduced the GMR head in its disk-drive products in 1997, and has been used in all of the world's total production of disk drives since then. The American Institute of Physics' Prize for Industrial Applications of Physics 1999/2000 was awarded to Stuart Parkin for *pioneering discoveries and original device demonstrations on giant magnetoresistive (GMR) read head technology for the magnetic recording industry* [32], and the Nobel Prize in Physics 2007 was awarded

¹Two different types of TMR are distinguished: current-perpendicular-to-plane TMR (CPP-TMR) and current-in-plane TMR (CIP-TMR). In the former the current flows through the barrier from one ferromagnetic electrode to the other, as depicted in Figure 1.2, while the current flows *in* the plane of the barrier in the latter. Technologically, the former is the most relevant, and we shall therefore limit ourselves to discussing this type.

to Albert Fert and Peter Grünberg for *the discovery of Giant Magnetoresistance* [33, 34, 35]. At this point in time, however, most of the hard disk drive companies have switched to CPP-TMR heads, which offer improved performance over GMR devices [36].

1.3 The Julliere model

Julliere in 1975 examined the low-temperature conductance differences of Fe-Ge-Co junctions [37] and arrived at the expression

$$\text{TMR} = \frac{2P_l P_r}{1 + P_l P_r} \quad (1.4)$$

where P_l and P_r are the spin-polarizations of the left- and right electrodes at the Fermi energy, respectively,

$$P = P(E_F) = \frac{n_\uparrow(E_F) - n_\downarrow(E_F)}{n_\uparrow(E_F) + n_\downarrow(E_F)} \quad (1.5)$$

where $n_\uparrow(E_F)$ and $n_\downarrow(E_F)$ are the spin-up and -down densities of states at the Fermi energy.

A cartoon-like representation of the tunneling of electrons from one density of states in the left electrode to another in the right is shown in Figure 1.4. The

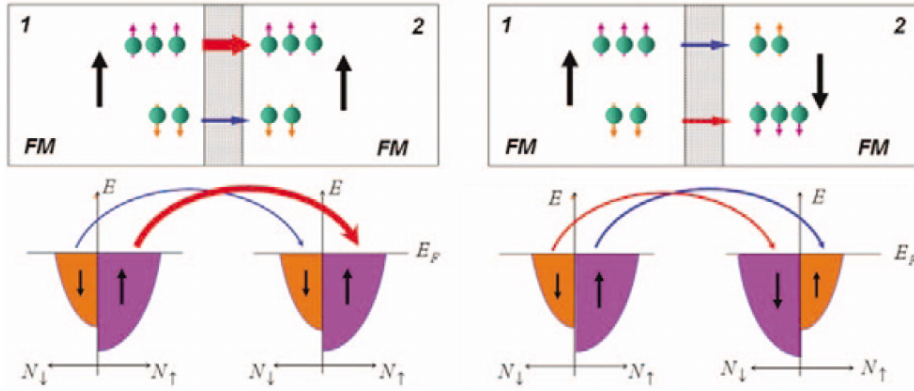


Figure 1.4: Illustration of tunneling through a magnetic tunnel junction in the parallel- (left) and anti-parallel magnetization configurations (right); the junction has identical electrodes. In the parallel configuration electrons of a given spin tunnel from a density of states in the left electrode to an identical density of states in the right, while electrons in the anti-parallel configuration tunnel from one density of states in the left electrode to another in the right. (Adapted from Reference [10]).

figure shows how majority- and minority-spin electrons tunnel from the left electrode to majority- and minority-spin states in the right electrode in the parallel configuration, while majority- and minority-spin electrons tunnel to minority- and majority-spin states in the anti-parallel configuration. Equation 1.4 follows immediately from the assumption that the tunneling probability is proportional to the product of the Fermi energy densities of states in the electrodes [38]. This assumption is too simplistic for the magnetic tunnel junctions discussed in this

work [1, 39] as it does not take differences in tunneling matrix elements into account. In systems employing MgO barriers different tunneling states decay at very different rates when propagating through the barrier [1], and more complex models — such as the one used in this work — must be employed, taking into account differences in transport mechanisms.

1.4 Overview of research field

In 2001 theoretical studies [1, 2] predicted significantly higher zero-bias TMR values for MTJs employing crystalline MgO barriers than for systems employing the widely used amorphous AlO_x barriers [10, 40, 41]. These theoretical predictions were verified by two independent experiments showing high room-temperature TMR in MgO-based MTJs in late-2004 [5, 42] (220% and 180%, respectively). Values up to 500% have been observed for systems employing Fe-CoB electrodes [43], while numerical studies of idealized systems predict values of several thousand percent [1, 2, 84, 85].

The reported TMR for magnetic tunnel junctions with AlO_x and MgO barriers is shown in Figure 1.5 for the period 1995–2006; the figure shows the dramatic

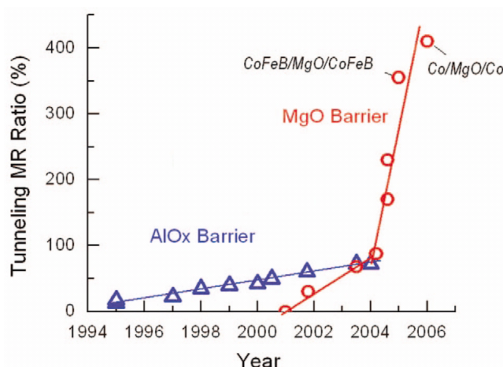


Figure 1.5: Reported room-temperature TMR for AlO_x and MgO-based magnetic tunnel junctions from 1994 to 2006. The introduction of the MgO barrier in 2001 led to a dramatic increase in TMR [31]. (From Reference [10]).

increase in room-temperature TMR since the introduction of MgO barriers². It is interesting to note that the use of MgO barriers in magnetic tunnel junctions was first proposed based on first-principles calculations like the ones discussed in this work, and that these calculations lead to such a dramatic increase in TMR due to a completely new understanding of the tunneling process.

The TMR is not the only important parameter when magnetic tunnel junctions are used in technological applications. The resistance of the junctions, measured by the resistance-area product, $R \cdot A$, is also of great importance. As discussed in the following section magnetic tunnel junctions are used in the read heads of hard disk drives and in a new type of solid-state memory called magnetic random access memory (MRAM). The junction resistance is of great importance in both technologies.

²The current record of 500% is for a system employing FeCoB electrodes [43].

Application of magnetic tunnel junctions in hard disk drives

The use of a magnetic tunnel junction in the read head of a hard disk drive is visualized in Figure 1.6. One electrode in the structure is “free” and switches

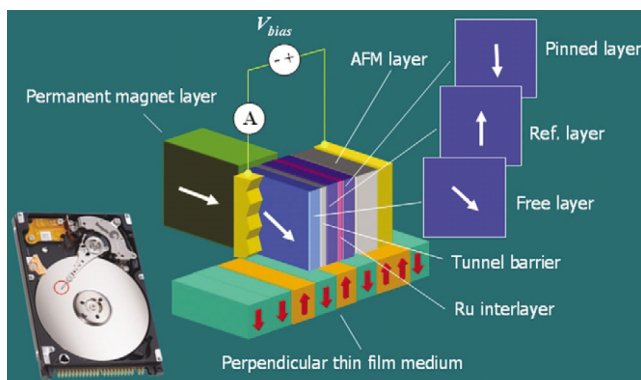


Figure 1.6: Illustration of a magnetic tunnel junction used in the read head of a hard disk drive. The junction consists of a free layer, a tunnel barrier, a reference layer, an interlayer, a pinned layer, and an antiferromagnetic layer. (From Reference [10]).

its magnetization direction when influenced by the magnetic fields associated with the magnetic domains on the disk medium, which rotates beneath it. A measurable change in device resistance results. The other electrode is “fixed” and does not change its magnetization direction. It consists of a reference layer, an interlayer, and a pinned layer, which together constitute what is referred to as a synthetic antiferromagnet (SAF). The magnetization direction of the pinned layer is constrained by an exchange bias field, which arises from the interface with the antiferromagnetic layer next to it, and the reference layer is constrained by a strong antiparallel coupling with the pinned layer [10]. The purpose of the pinned layer is to compensate for the stray fields from the reference layer. For applications in hard disk drives the resistance-area product of the junction must be sufficiently low, since higher read head resistance leads to increased Johnson- and shot noise as well as limiting the data rate [10].

The free layer in the read head of a hard disk drive must be sufficiently “free” to change its magnetization direction when influenced by the magnetic flux from the passing disk medium. The degree to which it is “free” is measured by the so-called magnetostriction coefficient. Materials with high spin-polarization, such as Fe, Co, and FeCoB, tend to also have high magnetostriction coefficient, so the free layer is sometimes made from a composite of a thin layer with high spin-polarization, positioned next to the barrier, and a thick layer with low magnetostriction coefficient, positioned away from the barrier. The two layers couple ferromagnetically and act as a single magnetic entity [10].

Application of magnetic tunnel junctions in MRAM

The use of a magnetic tunnel junction in the memory cell of a magnetic random access memory chip is visualized in Figure 1.7. In MRAM a data bit is stored in the free layer, which represents a zero or one depending on its magnetization direction relative to the direction of the fixed layer. A bit is read by measuring

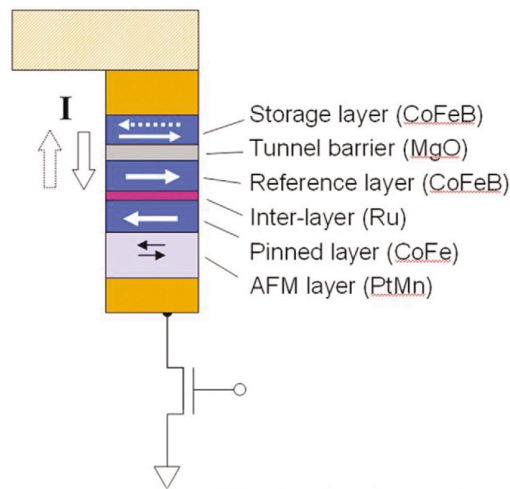


Figure 1.7: Illustration of a magnetic tunnel junction used in the memory cell of a magnetic random access memory chip. As was the case for the hard disk drive read head, the junction consists of a free layer, a tunnel barrier, a reference layer, an interlayer, a pinned layer, and an antiferromagnetic layer. This particular memory cell uses the spin-transfer torque effect to switch the free layer from one magnetization direction to the other. (From Reference [10]).

the device resistance and is written by switching the magnetization direction. The most promising technology for switching the magnetization in MRAM is the use of spin-transfer torque, in which a spin-polarized current through the junction induces a torque on the local magnetic moments in the free layer and in this way switches the layer from one polarization to the other. For applications in spin-transfer torque switched magnetic random access memory the resistance-area product of the junction must be sufficiently low to reach the necessary switching current without reaching the damaging breakdown voltage, which is usually on the order of 1 V [10].

Research & development challenges

The development of magnetic tunnel junctions suitable for commercial applications have met several challenges, the most important of which are listed below.

- Identification of electrode materials with high spin-polarization.
- Identification of electrode materials with low magnetostriction coefficient.
- Optimization of processing techniques.
- Utilization of symmetry-dependent tunneling effects.

The three former contributed to the increase in TMR in AlO_x based magnetic tunnel junctions and follow the Julliere model approach to development: if you can find electrode materials with high spin-polarization, and the electrodes can be easily switched by an external magnetic field, *and* you can grow junctions of high structural quality using these electrodes, you can develop high-TMR

systems. The latter added another level of sophistication to the field: all of the above remains true, but if you can *on top of these properties* find electrodes and barriers in which the symmetries of electrode Bloch states tunnel with different decay rates in the barrier, depending on their spin and symmetries, you can take advantage of symmetry-dependent tunneling effects and dramatically increase the TMR. This is the important result of the first-principles calculations carried out by Butler *et al.* [1] and the foundation of the work described in this thesis.

The industry is currently focusing on rather pragmatic issues: they know how to grow magnetic tunnel junctions of high structural quality using complex (and expensive!) growth techniques, such as molecular beam epitaxi, but need to find simpler (and cheaper!) ways of performing the processing to be able to compete in the commercial markets. As one researcher told me, when discussing the magnetic tunnel junctions used in their MRAM efforts: “what we’ve got is a big, dirty mess of all sorts of stuff; we’re just trying to make it work using our simple processing techniques”.

1.5 Overview of commercial markets

While scientists continue building on the basic understanding of magnetic tunnel junctions engineers are rapidly moving towards using these in hard disk drive read heads and novel magnetic memory systems, such as magnetic random access memory (MRAM). As mentioned in the previous section, the industry requires junctions with high TMR and low resistance-area product in order to enable such technologies, as well as systems that lend themselves to integration with existing solid-state technologies.

The hard disk drive industry, which since 1997 has been using current-in-plane GMR read heads, recently switched to current-perpendicular-to-plane TMR heads and are currently shipping drives using this technology. Some companies, such as Hitachi [44], are already in the process of switching to current-perpendicular-to-plane GMR heads, but most companies, including Fujitsu [36] and Seagate, are planning to continue the use of CPP-TMR read heads in their hard disk drive production until at least 2010.

Figure 1.8 shows the growth in hard disk drive sales for the years 2001 through 2005 as well as the projected growth for the years 2006 through 2010. At an average sale price of approximately USD 60 the projection amounts to a USD 53,000 million market in 2010, dominated by large sales for desktop computers, mobile computers, and consumer electronics.

Almost all major players in the electronics industry had MRAM programs five years ago, but most have quit pursuing this new memory and are awaiting technology- and market growth [46]. Fujitsu, Grandis, IBM, Samsung, Seagate, and Sony continue development, and have settled on spin-transfer torque switching after attempting a number of different switching approaches.

The potential of MRAM is compared to existing technologies in Table 1.1. The table shows that MRAM has the potential to become as fast as static random access memory (SRAM) and as dense as dynamic random access memory (DRAM), while at the same time offering the non-volatility of flash and hard disk drives at a significantly higher data rate. Tom Lee from Freescale Semiconductor³, who has compiled a similar table [47], claims that MRAM could someday

³Freescale on July 10th 2006 announced its volume production of the first commercially

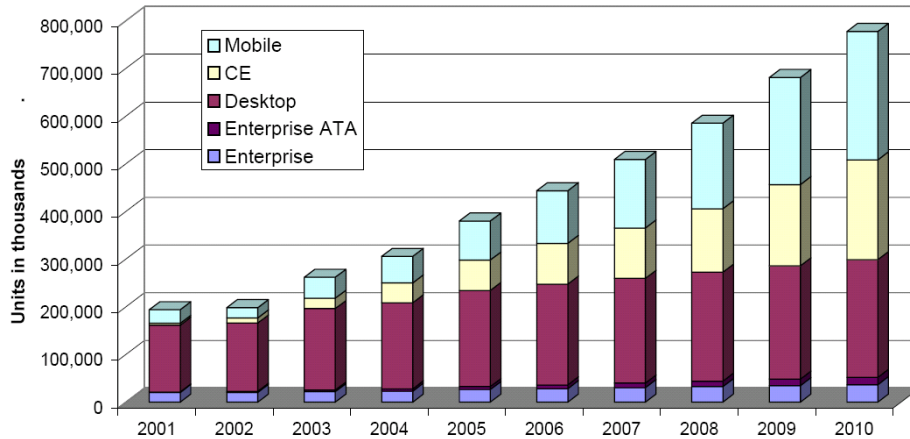


Figure 1.8: Growth in hard disk drive sales for 2001–2005 and projected growth for 2006–2010 (projected mid-2006). The total market has a projected size of USD 53,000 million in 2010. (From Reference [45]).

	DRAM	SRAM	Flash	MRAM
Write speed	Moderate	Fast	Slow	Fast
Read speed	Moderate	Fast	Fast	Fast
Density	High	Low	High	High
Durability	Good	Good	Poor	Good
Power	High	Low	Low	Low
Refresh	Yes	No	No	No
Retention	No	No	Yes	Yes
Scalability	Bad	Good	Good	Good
Cost	+25%	+0%	+25%	+25%

Table 1.1: Estimated performance of different memory technologies. MRAM has the potential to compete with all existing technologies, and may develop into a universal memory. (From Reference [46]).

be hailed as a universal memory, and a group of researchers from Philips in the Netherlands, after comparing MRAM with other novel non-volatile memory technologies, concludes that MRAM will give revolutionary advantages over the currently used silicon embedded memories [48].

Projections done by NanoMarkets indicate that the market for MRAM could reach USD 8,400 million by 2010 [49], and — according to market research company ISuppli — the annual market for a universal memory, combining the speed of SRAM, the density of DRAM, and the non-volatility of flash, could be USD 76,300 million by 2019 [50].

1.6 Objective of thesis

The objective of this thesis is to use computational models of magnetic tunnel junctions to understand and describe their spin-transport properties.

Specifically, we investigate the spin-transport properties of current-carrying magnetic tunnel junctions consisting of insulating MgO barriers sandwiched between Fe, Co, and FeCo ferromagnetic electrodes. By utilizing different electrodes we examine how the choice of electrode material influences the TMR, and consider the implications for achieving increased data storage capacity in hard disk drives and the development of MRAM devices.

In addition, we elaborate on the phenomenological description of tunneling mechanisms developed by Butler *et al.* [1], and consider their applicability to the three systems when a finite bias voltage is applied. We provide a thorough, consistent treatment of the magnetic tunnel junctions using the same calculation method and approach. Besides the physical insights this yields, our calculations provide useful benchmark data to the community.

In Chapter 3 we investigate the bulk properties of Fe and Co and conduct a benchmark study of the spin-transport properties of the Fe/MgO/Fe systems investigated in Reference [1]. In Chapter 4 we set up and optimize the three tunnel junctions mentioned above, and in Chapters 5 and 6 we analyze their spin-transport properties under zero-bias and finite-bias conditions.

1.7 Summary

Magnetic tunnel junctions are simple solid-state components, consisting of an insulating barrier sandwiched between ferromagnetic electrodes. The tunneling magnetoresistance (TMR) is a measure of the difference in conductance or current between the parallel- and anti-parallel configurations of the electrode magnetizations. This effect can be described by Julliere's model, which provides a simple equation for calculating the TMR based on the magnetic polarizations of the electrodes alone, but more complex models are necessary to properly

available MRAM device, the MR2A16A 4Mbit chip. They state that the device is appropriate for a range of applications, including networking, security, data storage, gaming and printers; it is engineered to be a reliable, economical, single-component replacement for present day battery-packed SRAM units. It is, as must be expected for a first-in-market product, not fast enough, dense enough, or cheap enough to compete with existing technologies in the general RAM market, and it presently serves only niche markets where these parameters are not the most important.

describe the effect for most systems of practical interest, including all systems discussed in this thesis.

Scientists are currently working on improving the understanding of such systems while engineers are working on using them in existing storage technologies and new memory technologies. The most promising memory technology, magnetic random access memory (MRAM), appears to have a huge market.

In this work we investigate the properties of MgO-based magnetic tunnel junctions with Fe, Co, and FeCo electrodes, and examine how differences in electrode material influence the spin-transport properties under both zero-bias and finite-bias conditions.

Chapter 2

Theoretical foundation

The theoretical description of many-electron systems forms the basis of the analyses in this work: in order to determine the physical properties of a system of interest, be it the structural, magnetic, or spin-transport properties, we must first determine its electronic structure.

To introduce the basic ideas and concepts this chapter outlines many-electron theory. It starts from the many-body Schrödinger equation and goes through the Born-Oppenheimer approximation to the electronic Schrödinger equation. The variational principle for the ground state energy is then discussed, and two wave function-based methods (the Hartree method and Hartree-Fock theory) are presented. Some problems associated with these methods when dealing with large systems are discussed, and density functional theory, a conceptually different type of method, is presented. Finally, the use of density functional theory for the modeling of quantum transport phenomena is outlined briefly, and the Landauer approach to transport is introduced along with a non-equilibrium Green's function method for the calculation of the current.

2.1 The many-body Schrödinger equation

In non-relativistic many-particle quantum mechanics, the Hamiltonian operator for a system consisting of many electrons bound to many nuclei is of the form

$$\hat{H} = \hat{T}_e + \hat{T}_n + \hat{V}_{ee} + \hat{V}_{en} + \hat{V}_{nn} \quad (2.1)$$

where the first two terms represent the kinetic energies of the electrons and the nuclei, and the last three terms represent the potential energies of the electron-electron interactions, the electron-nuclei interactions, and the nuclei-nuclei interactions. The different terms are given by

$$\hat{T}_e = - \sum_i \frac{\hbar^2}{2m_e} \nabla_{\mathbf{r}_i}^2 \quad (2.2)$$

$$\hat{T}_n = - \sum_j \frac{\hbar^2}{2M_j} \nabla_{\mathbf{R}_j}^2 \quad (2.3)$$

$$\hat{V}_{ee} = + \sum_i \sum_{k \neq i} \frac{1}{2} \frac{1}{4\pi\epsilon_0} \frac{e^2}{|\mathbf{r}_i - \mathbf{r}_k|} \quad (2.4)$$

$$\hat{V}_{en} = - \sum_i \sum_j \frac{1}{4\pi\epsilon_0} \frac{Z_j e^2}{|\mathbf{r}_i - \mathbf{R}_j|} \quad (2.5)$$

$$\hat{V}_{nn} = + \sum_j \sum_{l \neq j} \frac{1}{2} \frac{1}{4\pi\epsilon_0} \frac{(Z_j + Z_l) e^2}{|\mathbf{R}_j - \mathbf{R}_l|} \quad (2.6)$$

where the sums over i and k are over all electrons in the system, and the sums over j and l are over all nuclei. The signs of the potential energy terms clearly indicate which increase and which decrease the total energy. In the above, m_e is the electron mass, M_j is the mass of the j th nucleus, e is the elementary charge, ϵ_0 is the permittivity of vacuum, \mathbf{r} and \mathbf{R} are the positions of the electrons and the nuclei, respectively, and the Laplacians operate on these electronic- and nucleonic coordinates. Note that the operators $\hat{V}_{en} = \hat{V}_{en}(\{\mathbf{r}_i\}, \{\mathbf{R}_j\})$ and $\hat{V}_{nn} = \hat{V}_{nn}(\{\mathbf{R}_j\})$ both include the nucleonic position operator, $\{\mathbf{R}_j\}$; this fact is important in the derivation of the electronic Schrödinger equation.

2.2 The electronic Schrödinger equation

The many-particle quantum states and energy levels are found by solving the time-independent Schrödinger equation,

$$\hat{H} \Psi(\{\mathbf{x}_i\}, \{\mathbf{X}_j\}) = E \Psi(\{\mathbf{x}_i\}, \{\mathbf{X}_j\}) \quad (2.7)$$

where $\Psi(\{\mathbf{x}_i\}, \{\mathbf{X}_j\})$ and E are the wave function and energy, respectively, and $\mathbf{x}_i = (\mathbf{r}_i, s_i)$ and $\mathbf{X}_i = (\mathbf{R}_i, S_i)$ specify the positions and spins of electrons and nuclei. The notation emphasizes the fact that the wave function is a function of the positions and spins of all n electrons and N nuclei (it is a many-particle wave function),

$$\Psi(\{\mathbf{x}_i\}, \{\mathbf{X}_j\}) = \Psi(\mathbf{x}_1, \dots, \mathbf{x}_n, \mathbf{X}_1, \dots, \mathbf{X}_N) \quad (2.8)$$

Note that spin degrees of freedom do not appear in the Hamiltonian operator, Equation 2.1, and that spin therefore enters the non-relativistic equations only through the wave functions. Equation 2.7 is an eigenvalue equation: the resulting wave functions are eigenfunctions, and the resulting energies are eigenvalues.

For a given solution to the equation, $\Psi(\{\mathbf{x}_i\}, \{\mathbf{X}_j\})$, the quantity

$$\int_{v_1} \dots \int_{v_n} \int_{V_1} \dots \int_{V_N} |\Psi(\mathbf{x}_1, \dots, \mathbf{x}_n, \mathbf{X}_1, \dots, \mathbf{X}_N)|^2 d\mathbf{x}_1 \dots d\mathbf{x}_n d\mathbf{X}_1 \dots d\mathbf{X}_N \quad (2.9)$$

represents the probability of finding electron i in volume v_i with spin s_i and nucleus j in volume V_j with spin S_j , *i.e.* of finding all the particles at specific points in space with specific spins.

Since the time scales for electronic processes are far shorter than those for the nuclei, the wave function is separated into a wave function for the electrons, $\psi(\{\mathbf{x}_i\}; \{\mathbf{R}_j\})$, and a wave function for the nuclei, $\phi(\{\mathbf{X}_j\})$,

$$\Psi(\{\mathbf{x}_i\}, \{\mathbf{X}_j\}) = \psi(\{\mathbf{x}_i\}; \{\mathbf{R}_j\}) \phi(\{\mathbf{X}_j\}) \quad (2.10)$$

Note how the electronic wave function depends explicitly on the positions and spin of the electrons and parametrically on the positions of the nuclei, while the nucleonic wave function depends only on the positions and spins of the nuclei.

Applying the Hamiltonian operator, Equation 2.1, to the separated wave function, Equation 2.10, and invoking the Born-Oppenheimer approximation, the time-independent Schrödinger equation, Equation 2.7, can be split into two coupled equations,

$$\hat{T}_e \psi + \hat{V}_{ee} \psi + \hat{V}'_{en} \psi = E_e \psi \quad (2.11)$$

and

$$\hat{T}_n \phi + V'_{nn} \phi + E_e \phi = E \phi \quad (2.12)$$

where the simple notations $\psi = \psi(\{\mathbf{x}_i\}; \{\mathbf{R}_j\})$ and $\phi = \phi(\{\mathbf{X}_j\})$ are used.

In order to find the eigenenergies of the many-electron system, the electronic Schrödinger equation, Equation 2.11, must be solved to find the electronic energy, $E_e = E_e(\{\mathbf{x}_i\}; \{\mathbf{R}_j\})$, for a given configuration of the nuclei. Once E_e has been found, for a given electronic state, the nucleonic Schrödinger equation, Equation 2.12, can be solved to find the eigenenergies and the nucleonic dynamics of the system (for this particular electronic state).

Throughout the remainder of this thesis we will focus only on the electronic Schrödinger equation, and the nuclei will be treated as static point-like particles having no other effect than to set up an external potential in which the electrons move around. While this approach is common practice, other more complex methods, which include time-dependent electron-nuclei interactions, exist and are predicted to become important for the description of ultrafast phenomena in future nanotech devices [51].

2.3 The variational principle for the energy of the ground state

The eigenstate of the electronic Schrödinger equation that has the lowest energy is called the ground state, and has the useful property of obeying the variational principle. This principle states that the expectation value of the Hamiltonian operator with respect to *any* trial wave function, ψ_t , is greater or equal to that for the ground state, ψ_0 , *i.e.*

$$\int \cdots \int \psi_t^* \hat{H} \psi_t \, d\mathbf{x}_1 \cdots d\mathbf{x}_n \geq \int \cdots \int \psi_0^* \hat{H} \psi_0 \, d\mathbf{x}_1 \cdots d\mathbf{x}_n \quad (2.13)$$

where the integrations are over all position- and spin degrees of freedom. The equality is satisfied only for $\psi_t = \psi_0$, *i.e.* when the trial wave function *is* the ground state wave function.

The variational principle is very useful, since it allows us to find the electronic ground state wave function of a system by minimizing the energy functional $E_e[\psi_t]$ by varying the trial wave function; the principle is at the root of the methods described in the remainder of this chapter.

2.4 Wave function methods

In order to approximately solve the many-electron problem, it is converted into a one-electron problem by approximating the many-electron wave functions, $\psi(\{\mathbf{x}_i\}; \{\mathbf{R}_j\})$, by products of orthogonal one-electron wave functions, $\{\varphi_i(\mathbf{x}_i)\}$.

The wave functions include both spatial- and spin degrees of freedom, and are therefore sometimes referred to as spin orbitals [52].

The one-electron wave functions can — for example — be represented as linear combinations of atomic orbitals (the LCAO approach is the one implemented in the software used for this work¹). If the set of basis functions is complete the one-electron states are perfectly described, but using a less-than-complete basis set to describe the one-electron wave functions results in limited accuracy.

There are different ways of approximately solving the many-electron problem using one-electron orbitals, but only two generic approaches are discussed here: the Hartree method and Hartree-Fock theory.

2.4.1 The Hartree method

A simple way of finding an approximation to the many-electron problem is through the Hartree method, in which the many-electron wave function is represented by a product of orthogonal one-electron wave functions,

$$\psi(\{\mathbf{x}_i\};\{\mathbf{R}_j\}) = \prod_i \varphi_i(\mathbf{x}_i) \quad (2.14)$$

where the product incorporates a one-electron wave function for each electron in the system. The product wave function, known as a Hartree product, is a trial variational wave function, and the electronic coordinates are assumed to be separable.

Taking the expectation value of the many-electron Hamiltonian, Equation 2.1, with regard to the Hartree product, Equation 2.14, and applying the variational principle, we arrive at the set of Hartree equations

$$\hat{h}_i(\mathbf{x}_i) \varphi_i(\mathbf{x}_i) + \sum_k [J_k(\mathbf{x}_i)] \varphi_i(\mathbf{x}_i) = \varepsilon_i \varphi_i(\mathbf{x}_i) \quad (2.15)$$

where the sum runs over all electrons, and the core Hamiltonian, $\hat{h}_i(\mathbf{x}_i)$, and the Coulomb operator, $\hat{J}_k(\mathbf{x}_i)$, are defined through

$$\hat{h}_i(\mathbf{x}_i) \varphi_i(\mathbf{x}_i) = -\frac{\hbar^2}{2m_e} \nabla_{\mathbf{r}_i}^2 \varphi_i(\mathbf{x}_i) - \sum_j \frac{1}{4\pi\epsilon_0} \frac{Z_j e^2}{|\mathbf{r}_i - \mathbf{R}_j|} \varphi_i(\mathbf{x}_i) \quad (2.16)$$

$$\hat{J}_k(\mathbf{x}_i) \varphi_i(\mathbf{x}_i) = \frac{1}{4\pi\epsilon_0} \left[\int \frac{\varphi_k^*(\mathbf{x}_k) \varphi_k(\mathbf{x}_k)}{|\mathbf{r}_i - \mathbf{r}_k|} d\mathbf{x}_k \right] \varphi_i(\mathbf{x}_i) \quad (2.17)$$

The Hartree approximation takes into account the classic electrostatic repulsion between one electron and all the rest. Note that the Coulomb operator, which represents these electron-electron interactions, depends only on the density of the surrounding electrons (as opposed to \hat{V}_{ee} , which depends explicitly on the positions of all other electrons); for this reason, the Hartree method is referred to as a mean-field theory. Note also that the Coulomb operator operates on *all* one-electron wave functions, and that the electron therefore interacts with

¹Atomistix ToolKit, which is used for the studies in this work, uses SIESTA orbitals [53], which are pseudo-atomic orbitals of finite radius generated from pseudopotentials in spherical “cages”, *i.e.* with finite cut-off radii at which the potentials go to infinity.

itself (the reason for this will become clear in the next section, where the self-interaction is canceled out).

The Hartree equations must be solved self-consistently, as the equations depend on their own solutions through the Coulomb operator. The self-consistent field (SCF) procedure consists of three steps [54]:

1. Make a guess at the Hartree product that best represents the electronic ground state wave function. If the one-electron wave functions are expanded in a basis of atomic orbitals, this step amounts to choosing sensibly the expansion coefficients.
2. Set up the single-electron Hamiltonian based on the guess made in step 1.
3. Solve the Hartree equations to find the one-electron states that contribute to the Hartree product.

Once these three steps have been undertaken, the resulting Hartree product (found in step 3) is compared with the initial Hartree product (guessed in step 1): if their difference is *not* within a specified tolerance, the two Hartree products are “mixed” and steps 2 and 3 are executed again with the new guess; if the difference *is* within this tolerance, a self-consistent approximation to the electronic ground state has been found.

The Hartree equations have an infinite number of solutions, but only the lowest-energy wave functions are relevant since we are only interested in the ground state of the system. In step 3, only the n single-electron solutions with the lowest corresponding values of ε_i are used to construct the many-electron wave function (n is the number of electrons).

As mentioned earlier, the accuracy of results is limited by the number of basis states used: a small number of basis states gives limited accuracy, while a complete set of basis states gives perfect accuracy (within the Hartree method, of course). By adding more and more basis states to the basis sets describing the one-electron wave functions, therefore, the variational principle ensures convergence towards to the true ground state energy from above, as the calculated Hartree product comes closer and closer to the exact Hartree product.

As discussed in Reference [52], the Hartree method, while simple and intuitive in nature, has one major short-coming: it is not anti-symmetric under the interchange of identical particles, as it must be for electrons since they are fermions; introducing the Pauli principle into the description, as done in *e.g.* Hartree-Fock theory to be described next, introduces spin correlations, in the sense that no two electrons with identical spin can share the same spacial orbital.

2.4.2 Hartree-Fock theory

A logical extension of the Hartree method is Hartree-Fock theory, which includes the use of anti-symmetric many-electron trial variational wave functions and a number of methods for solving the electronic Schrödinger equation. The latter is done through a simplified Hamiltonian operator, which leads to the Hartree-Fock equations.

In Hartree-Fock theory the many-electron wave function is represented by a

Slater determinant,

$$\psi(\{\mathbf{x}_i\};\{\mathbf{R}_j\}) = \frac{1}{\sqrt{n!}} \det \left(\begin{bmatrix} \varphi_1(\mathbf{x}_1) & \varphi_2(\mathbf{x}_1) & \cdots & \varphi_n(\mathbf{x}_1) \\ \varphi_1(\mathbf{x}_2) & \varphi_2(\mathbf{x}_2) & \cdots & \varphi_n(\mathbf{x}_2) \\ \vdots & \vdots & \ddots & \vdots \\ \varphi_1(\mathbf{x}_n) & \varphi_2(\mathbf{x}_n) & \cdots & \varphi_n(\mathbf{x}_n) \end{bmatrix} \right) \quad (2.18)$$

i.e. by an anti-symmetrized product of one-electron wave functions. As in the Hartree method, a one-electron wave function for each electron in the system is incorporated in the approximation of the many-electron wave function.

Anti-symmetrizing a Hartree product to obtain a Slater determinant introduces exchange effects, as the anti-symmetry requirement on the electronic wave function is fulfilled. The Slater determinant correlates the motions of electrons with identical spins, and in that way incorporates *exchange correlation*, while the motions of electrons with different spins remain uncorrelated. Since two electrons with identical spin cannot occupy the same region of space, a *Fermi hole* is said to exist around electrons [52].

Taking the expectation value of the many-electron Hamiltonian, Equation 2.1, with regard to the Slater determinant, Equation 2.18, and applying the variational principle, we arrive at the set of Hartree-Fock equations²

$$\hat{h}_i(\mathbf{x}_i) \varphi_a(\mathbf{x}_i) + \sum_u [J_u(\mathbf{x}_i) - K_u(\mathbf{x}_i)] \varphi_a(\mathbf{x}_i) = \varepsilon_a \varphi_a(\mathbf{x}_i) \quad (2.19)$$

where the sum runs over all electrons, and the core Hamiltonian, $\hat{h}_i(\mathbf{x}_i)$, the Coulomb operator, $\hat{J}_u(\mathbf{x}_i)$, and the exchange operator, $\hat{K}_u(\mathbf{x}_i)$, are defined

$$\hat{h}_i(\mathbf{x}_i) \varphi_a(\mathbf{x}_i) = -\frac{\hbar^2}{2m_e} \nabla_{\mathbf{r}_i}^2 \varphi_a(\mathbf{x}_i) - \sum_j \frac{1}{4\pi\epsilon_0} \frac{Z_j e^2}{|\mathbf{r}_i - \mathbf{R}_j|} \varphi_a(\mathbf{x}_i) \quad (2.20)$$

$$\hat{J}_u(\mathbf{x}_i) \varphi_a(\mathbf{x}_i) = \frac{1}{4\pi\epsilon_0} \left[\int \frac{\varphi_u^*(\mathbf{x}_k) \varphi_u(\mathbf{x}_k)}{|\mathbf{r}_i - \mathbf{r}_k|} d\mathbf{x}_k \right] \varphi_a(\mathbf{x}_i) \quad (2.21)$$

$$\hat{K}_u(\mathbf{x}_i) \varphi_a(\mathbf{x}_i) = \frac{1}{4\pi\epsilon_0} \left[\int \frac{\varphi_u^*(\mathbf{x}_k) \varphi_a(\mathbf{x}_k)}{|\mathbf{r}_i - \mathbf{r}_k|} d\mathbf{x}_k \right] \varphi_u(\mathbf{x}_i) \quad (2.22)$$

As discussed in Reference [54], the Coulomb operator takes into account the Coulombic repulsion between electrons, and the exchange operator takes into account the modifications to this interaction due to the effects of spin correlations. Note that $\hat{J}_a(\mathbf{x}_i) \varphi_a(\mathbf{x}_i) = \hat{K}_a(\mathbf{x}_i) \varphi_a(\mathbf{x}_i)$, and that the electron self-interaction mentioned in the previous section is naturally left out in Hartree-Fock theory.

Just as with the Hartree equations, the Hartree-Fock equations must be solved self-consistently, and the calculated energy decreases towards the exact ground state energy when more and more basis states are used to describe the one-electron wave functions; a limit is reached before getting all the way there, however, at what is known as the Hartree-Fock limit, which is the limit of accuracy intrinsic in the theory itself.

²The treatment of Slater determinants in Hartree-Fock theory is completely analogous to the treatment of Hartree products in the previous section, and we will not go into the details here. Thorough treatments can be found in References [52] and [54].

Rather than going into the details of Hartree-Fock theory³, we will describe a totally different approach to many-electron physics, an approach in which the struggle to find the ground state wave function is reduced to the computation of the ground state electron density, which — in principle — is all that is needed to calculate the ground state properties of a system; this approach is known as density functional theory, and is the one implemented in Atomistix ToolKit. First, however, we will take a little detour, and briefly discuss some problems associated with the wave function methods discussed in the preceding two sections.

2.4.3 Scaling problems associated with the wave function methods

As discussed by Walter Kohn in his Nobel price address in 1998⁴, solving the electronic Schrödinger equation becomes increasingly difficult when the number of electrons grows. The problems arise due to the large number of parameters needed to achieve satisfactory results. To perform calculations and store results for a system consisting of, say, $N = 100$ chemically active electrons with an accuracy requiring just $p = 3$ parameters per variable, the total number of parameters required is $M \approx 10^{150}$! Minimizing the energy in a space of 10^{150} dimensions is a daunting task, and the way the total number of parameters increases with the number of electrons ($M = p^{3N}$) gives rise to what Kohn refers to as an “exponential wall”.

Due to these “scaling problems”, traditional wave function methods are not useful for describing the electronic structure of systems of practical interest, and other methods must be put to use. Kohn himself argues for the value in considering the electron density as the basic parameter of methods, and received the Nobel price for his work in developing density functional theory.

2.5 Density functional theory

The last method of describing many-electron systems to be discussed here, and the method used as a mean-field-like theory to describe the electronic structure and electron transport properties of magnetic tunnel junctions in this work, is density functional theory (DFT), developed in the mid-1960’s.

Density functional theory offers a description in which the complicated many-electron wave function, $\psi(\{\mathbf{x}_i\};\{\mathbf{R}_j\})$, and the associated Schrödinger equation are replaced by the much simpler electron density, $n(\mathbf{r})$, and its associated calculation scheme, known as the Kohn-Sham equations [56]. The simplification achieved is immense, and density functional theory therefore provides a means

³A number of theories are based on the Slater determinants used in Hartree-Fock theory, and can be considered more complex versions of this. As an example can be mentioned *configuration interaction*, in which many-electron wave functions are represented by linear combinations of Slater determinants [52, 54].

⁴Walter Kohn shared the Nobel price in Chemistry with John Pople, and his address (captured in Reference [55]) is a real gem. It provides an extremely elegant discussion of the phenomenological and practical problems associated with applying traditional multi-particle wave function methods to systems of practical interest, and goes as far as to state that the many-electron wave function is not a legitimate scientific concept for such systems.

of treating system sizes of relevance to this work using standard computational resources.

Very briefly, DFT is a formal theory for the ground state electron density and -energy, and makes use of a set of single-electron orbitals. These can (in principle) be used to describe the ground state density and -energy exactly, and can (pragmatically) be used to describe other physical properties, such as electron transport. It should be emphasized from the very beginning, however, that DFT is formally only valid for the ground state density and -energy, and that there is absolutely no guarantee that other properties are correctly described.

2.5.1 The Hohenberg-Kohn theorem

The Hohenberg-Kohn theorems [57] state that the full many-electron ground state of an interacting inhomogeneous electron gas in a static external potential, $v(\mathbf{r})$, is a unique functional of the ground state electron density of this system. In other words: if you know the ground state electron density, you can — in principle — find all other ground state properties.

The Hohenberg-Kohn theorems also state that there exists a universal functional of the electron density, $G[n]$, such that the non-degenerate ground state energy of such an electron gas satisfies

$$E_0 \leq E[n(\mathbf{r})] \quad (2.23)$$

where

$$E[n(\mathbf{r})] = \int v(\mathbf{r})n(\mathbf{r}) \, d\mathbf{r} + \frac{1}{2} \frac{e^2}{4\pi\epsilon_0} \iint \frac{n(\mathbf{r})n(\mathbf{r}')}{|\mathbf{r} - \mathbf{r}'|} \, d\mathbf{r} \, d\mathbf{r}' + G[n] \quad (2.24)$$

and the equality in Equation 2.23 is satisfied only when the expression is evaluated at the ground state electron density, *i.e.* $E_0 = E[n_0(\mathbf{r})]$. The ground state energy can, therefore, be found from a variational principle based on the electron density.

The first term on the right hand side of Equation 2.24 represents the classical interaction between the electrons and the external potential, and the second represents the classical Coulombic interaction between the electrons. The kinetic energy and all other interactions are by definition included in $G[n] = G[n(\mathbf{r})]$, which is in general unknown. The functional $G[n]$ is system-independent, in the sense that it depends only on the electron density (not on the positions of the atomic nuclei). Note that the positions of the nuclei — indeed, the concept of nuclei altogether — is non-existent in the description above; the only role of nuclei is as a source of a static external potential⁵. Again, the Born-Oppenheimer approximation is used to simplify the equations.

2.5.2 The Kohn-Sham equations

The Kohn-Sham equations [59] take this line of thought one step further, and prove that the ground state electron density and -energy can be found by solving a one-electron Schrödinger equation. The variational nature of the energy-density relationship described by Equation 2.23, *i.e.* the fact that the ground

⁵In multicomponent DFT [58], the nuclei and electrons are treated on an equal footing, *i.e.* the full many-particle problem is handled without the use of the Born-Oppenheimer approximation.

state electron density minimizes the energy functional, allows us to find these ground state properties by solving the system of equations known as the Kohn-Sham orbital equations [56],

$$\left\{ -\frac{\hbar^2}{2m_e} \nabla_{\mathbf{r}_i}^2 + v_{eff}(\mathbf{r}) \right\} \psi_i(\mathbf{r}) = E_i \psi_i(\mathbf{r}) \quad (2.25)$$

using the effective potential

$$v_{eff}(\mathbf{r}) = v(\mathbf{r}) + v_H(\mathbf{r}) + v_{xc}(\mathbf{r}) \quad (2.26)$$

with the density

$$n(\mathbf{r}) = \sum_i |\psi_i(\mathbf{r})|^2 \quad (2.27)$$

where the summation runs over all occupied electronic states.

The “wave functions” $\psi_i(\mathbf{r})$ are known as Kohn-Sham orbitals. While they appear as one-electron wave functions, they have no such physical interpretation. What Kohn and Sham showed is that there is a one-to-one correspondence between solving the full many-electron system to find the ground state electron density and solving the one-electron Kohn-Sham equations; the resulting ground state electron density is the same. It is tempting to think of the Kohn-Sham orbitals as one-electron wave functions, and we will make use of exactly such ideas. It is, however, important to always remember that there *is* no such physical interpretation included in Kohn-Sham theory, and that extreme care must therefore be taken when doing so. We choose to use this theory, in spite of the above-mentioned shortcomings, since it is the best tool available for the system sizes discussed in this work, and often provides reasonable results.

Equation 2.25 appears like a one-electron Schrödinger equation, with the exception that the one-electron potential has been replaced by an effective potential, $v_{eff}(\mathbf{r})$. The first term in the effective potential represents the external potential set up by the nuclei, and the second term represents the potential caused by the classical Coulomb interactions between the electrons; it is given by

$$v_H(\mathbf{r}) = \frac{e^2}{4\pi\epsilon_0} \int \frac{n(\mathbf{r}')}{|\mathbf{r} - \mathbf{r}'|} d\mathbf{r}' \quad (2.28)$$

and is known as the Hartree potential. The third term is known as the exchange-correlation potential, and is given by

$$v_{xc}(\mathbf{r}) = \frac{\delta E_{xc}[n]}{\delta n(\mathbf{r})} \quad (2.29)$$

where $E_{xc}[n] = G[n] - T[n]$ is the exchange-correlation energy, and $T[n]$ represents the one-electron kinetic energy; this term is discussed in some detail in the next section. The total electronic energy is

$$E = \sum_i E_i - \frac{1}{2} \int v_H(\mathbf{r}) n(\mathbf{r}) d\mathbf{r} + E_{xc}[n] - \int v_{xc}(\mathbf{r}) n(\mathbf{r}) d\mathbf{r} \quad (2.30)$$

where the summation again runs over all occupied states; it is *not* merely the sum of one-electron energies [56].

Like the Hartree equations, Equations 2.25, 2.26, and 2.27 must be solved self-consistently, since each depends on the other. Often, one makes a guess at the density, calculates the effective potential, inserts this into Equation 2.25, and solves to find the Kohn-Sham orbitals. These can, in turn, be used to calculate a new density, and the procedure begins all over again. This continues until convergence is reached, *i.e.* until the output density equals the input density.

2.5.3 Approximations to DFT

The third term in the effective potential in Equation 2.26 is known as the exchange-correlation potential; together with the Hartree potential, these two terms include all electron-electron interactions. Were this term known, DFT would be an exact theory for the ground state electron density and -energy of a many-electron system (within, of course, the limit of the Born-Oppenheimer approximation). No exact representation of the term is known, however, and DFT is therefore in practice only an approximate theory. Many different approximations to the exchange-correlation potential exist, the most generic of which are the local density approximation (LDA) and the generalized gradient approximations (GGA).

Local density approximation, LDA

In the local density approximation [59], the exchange-correlation potential depends only on the local electron density; it is taken as that calculated for a homogeneous electron gas (HEG),

$$v_{xc}^{\text{LDA}}(\mathbf{r}) = \frac{\delta E_{xc}^{\text{LDA}}[n]}{\delta n(\mathbf{r})} = \varepsilon_{xc}^{\text{HEG}}[n(\mathbf{r})] + n(\mathbf{r}) \frac{\partial \varepsilon_{xc}^{\text{HEG}}[n(\mathbf{r})]}{\partial n(\mathbf{r})} \quad (2.31)$$

where

$$E_{xc}^{\text{LDA}}[n] = \int \varepsilon_{xc}^{\text{HEG}}[n(\mathbf{r})] n(\mathbf{r}) \, d\mathbf{r} \quad (2.32)$$

is the exchange-correlation energy of a homogeneous electron gas of density n , and $\varepsilon_{xc}^{\text{HEG}}[n(\mathbf{r})]$ is the exchange-correlation energy per electron in such a system [56]. In the local density approximation, in other words, accurate expressions for the homogeneous electron gas are applied locally to inhomogeneous systems. While this approximation is very simple, it is surprisingly accurate for many systems, especially for the prediction of geometrical properties [54].

Generalized gradient approximation, GGA

In the generalized gradient approximation [54, 60], the LDA exchange-correlation potential is modified by a semi-local correction involving the gradient of the electron density, thus providing an — in principle — improved description of inhomogeneous systems.

Error sources in DFT

Generally, there are three sources of errors when using DFT:

1. Using the theory beyond its limits of applicability.

2. Approximating the exchange-correlation potential.
3. Numerical inaccuracies (due to using less-than-perfect model parameters).

As DFT only describes the ground state electron density and -energy, properties such as band gaps, excited states, and transport properties are not formally covered by the theory⁶. Furthermore, as no exact representation of the exchange-correlation potential is known, even the ground state electron density and -energy can only be found approximately. In spite of these severe limitations of the theory, DFT gives surprisingly good results for many systems [52, 54, 55, 56, 61, 62], including systems in which electron transport across barriers is important [1, 38, 63, 64, 65, 66].

2.5.4 Spin-dependent DFT

In the above, the spin degrees of freedom of electrons have not been mentioned. Spin-polarized DFT calculations can be performed using the same formalism if the Kohn-Sham equations are split into one set for each electron spin [56]

$$n(\mathbf{r}) \rightarrow \{n^\uparrow(\mathbf{r}), n^\downarrow(\mathbf{r})\} \quad (2.33)$$

$$\psi_i(\mathbf{r}) \rightarrow \{\psi_i^\uparrow(\mathbf{r}), \psi_i^\downarrow(\mathbf{r})\} \quad (2.34)$$

The Hartree potential is a function of the sum of the spin-densities,

$$v_H(\mathbf{r}) = \frac{e^2}{4\pi\epsilon_0} \int \frac{n^\uparrow(\mathbf{r}') + n^\downarrow(\mathbf{r}')}{|\mathbf{r} - \mathbf{r}'|} d\mathbf{r}' \quad (2.35)$$

since the Coulomb interaction is independent of spin, while the exchange-correlation potential for a given spin depends on the electron densities for both spins,

$$v_{xc}^\uparrow(\mathbf{r}) = \frac{\delta E_{xc}^\uparrow[n^\uparrow(\mathbf{r}), n^\downarrow(\mathbf{r})]}{\delta n^\uparrow(\mathbf{r})} \quad (2.36)$$

$$v_{xc}^\downarrow(\mathbf{r}) = \frac{\delta E_{xc}^\downarrow[n^\uparrow(\mathbf{r}), n^\downarrow(\mathbf{r})]}{\delta n^\downarrow(\mathbf{r})} \quad (2.37)$$

The spin-dependent Kohn-Sham equations, *i.e.* spin-dependent versions of Equations 2.25, 2.26, and 2.27, then become

$$\left\{ -\frac{\hbar^2}{2m_e} \nabla_{r_i}^2 + v_{eff}^\sigma(\mathbf{r}) \right\} \psi_i^\sigma(\mathbf{r}) = E_i^\sigma \psi_i^\sigma(\mathbf{r}) \quad (2.38)$$

with the spin-dependent effective potential

$$v_{eff}^\sigma(\mathbf{r}) = v(\mathbf{r}) + v_H(\mathbf{r}) + v_{xc}^\sigma(\mathbf{r}) \quad (2.39)$$

where σ represents spin-up or -down, $\sigma = \{\uparrow, \downarrow\}$, and

$$n(\mathbf{r}) = n^\uparrow(\mathbf{r}) + n^\downarrow(\mathbf{r}) = \sum_\sigma \sum_i |\psi_i^\sigma(\mathbf{r})|^2 \quad (2.40)$$

⁶The application of DFT to calculate electron transport properties is discussed in some detail in the next chapter.

i.e. the total electron density is the sum of the two spin-densities. It is clear from Equation 2.39 that all spin-dependent interactions are described by the exchange-correlation potential, the approximation to which must therefore include such interactions. The local spin-density approximation (LSDA) [67], an extension of the local density approximation, is used throughout this work.

While the spin degrees of freedom are included in the DFT method implemented in Atomistix ToolKit, the effects of external magnetic fields, local magnetic fields set up by electron flow, and spin-orbit coupling are neglected.

2.5.5 Reliability of DFT in describing physical properties

The systems of interest to us are all solid-state materials and combinations of these. The electronic structure of such solids are generally well described by LSDA-DFT, since their valence electron densities vary slowly [61]; this is especially true for metals [61, 62].

The reliability of LSDA-DFT in describing the geometric properties of these systems is generally good. Calculations usually find bond lengths of constituent materials with fairly good accuracy, with lattice constants normally underestimated by a few percent relative to experimental values [61, 62, 68]. Similarly, calculations provide good results for the magnetic moments of ferromagnetic metals [69, 70, 71], with values within ten percent of experimental data [70]. The bulk moduli are, however, typically overestimated by 15 – 20% [61, 68].

Kohn-Sham DFT significantly underestimates band gaps in semiconductors and insulators [72, 73] relative to experimental data. Most of the error is intrinsic to the theory itself (approximately 70% for Silicon [73]), but the use of local exchange-correlation potentials, such as LSDA, also contributes to the error. The band structures of relevant metals are, however, well described by LSDA-DFT [71], as are densities of states [71].

2.6 DFT applied to quantum transport

As discussed in the previous section, density functional theory is a ground state theory, and cannot formally be used to predict properties other than the ground state density and -energy. The Kohn-Sham orbitals have no physical interpretation, and there is no formal basis for using them to describe electron transport phenomena. Methods have, however, been developed to model the electronic properties of mesoscopic systems using a density functional theory description of the electronic structure [63, 64, 65, 74]. These methods use DFT pragmatically: while there is no formal basis for using the theory for transport calculations, results are reasonable for some systems, and no other theory offers a better compromise between reliability and computational efficiency.

This section briefly describes density functional theory as applied to quantum transport phenomena. The Landauer picture of quantum transport is outlined, the non-equilibrium Green's function (NEGF) method for the modeling of quantum transport is introduced, and the reliability of DFT in describing quantum transport phenomena is discussed.

2.6.1 The Landauer picture of quantum transport

Ohm's law relates the current through a macroscopic system, I , with the applied voltage, V ,

$$I = G \cdot V, \quad (2.41)$$

where the conductance, G , is given by

$$G = \sigma \frac{A}{L} \quad (2.42)$$

and σ is the conductivity, A is the area of the system perpendicular to the current flow, and L is the length of the system; the resistance is simply the inverse of the conductance, $R = 1/G$, and the resistivity is the inverse of the conductivity, $\rho = 1/\sigma$. For a given system, the conductivity is a measure of the average number of electronic scattering events per unit length; as electrons propagate through the system, they are scattered by material impurities *etc.*, and the current is limited. The conductivity enables a macroscopic description of electron transport, in which the discrete, microscopic scattering phenomena are represented by an average scattering rate.

When the dimensions of the system decreases below a certain size, the Ohmic description of conduction given by Equation 2.42 is no longer valid, since the statistical averaging over scattering events is no longer accurate. For such systems, coherent quantum mechanical descriptions must be put to use, which describe the scattering phenomena individually without any form of averaging. The results of conductance measurements on such a system is shown in Figure 2.1. The figure shows the results for the quantum point contact studied

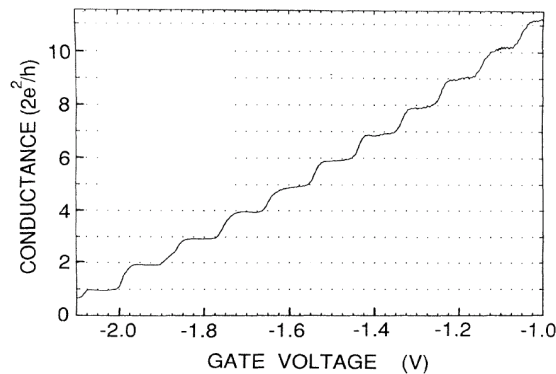


Figure 2.1: Conductance as function of gate voltage in a quantum point contact (QPC). When the gate voltage becomes increasingly smaller, the width of the QPC becomes increasingly smaller, and the conductance falls off in steps of the conductance quantum, $2e^2/h$. (From Reference [75]).

in Reference [75], which — by the way — offers a very good introduction to ballistic transport. When the gate voltage becomes increasingly smaller, the width of the QPC becomes increasingly smaller, and the number of conducting channels decreases. This leads to a step-wise decrease in conductance, which falls off in steps of the conductance quantum, $2e^2/h$. This system, which has dimensions comparable to the Fermi wavelength (see below), clearly demonstrates a non-Ohmic behavior: the conductance does *not* change linearly with

the lateral size of the conductor. Another example of non-Ohmic behavior is reported in Reference [76], in which a Gold wire is stretched until it consists of single atoms, and a constant conductance of $2e^2/h$ is measured while the wire is stretched until it breaks. In this example, the conductance does *not* change linearly with the length of the conductor.

The dimensions at which such quantum mechanical descriptions must be used are related to some characteristic length scales [63, 77]:

The screening length The distance at which a perturbation is screened by the electrons in a bulk. The screening length is on the order of Angstrom for relevant systems.

The Fermi wavelength The De Broglie wavelength for electrons at the Fermi energy. For systems with dimensions comparable to the Fermi wavelength, the wave nature of electrons is significant and cannot be ignored. The Fermi wavelength is on the order of Angstrom for relevant systems.

The mean free path The average distance an electron travels before losing its momentum in a scattering event. The mean free path is on the order of micrometers for relevant systems.

The phase-coherence length The average distance an electron travels before losing its phase information in a scattering event. Static scatterers, such as impurities without internal degrees of freedom, do not contribute to the phase-relaxation limiting the phase-coherence length, as they preserve a definite phase relationship between different electron paths. Dynamic scattering processes, such as electron-electron- and electron-phonon scattering, on the other hand, do contribute. The phase-coherence length is on the order of micrometers for relevant systems.

The systems of interest in this work have dimensions that are far smaller than the mean free path and the phase-coherence length, so transport can be described as happening without loss of momentum or phase-coherence. The dimensions of the screening layers, discussed in Section 4.1, are comparable to the screening length, so the scattering region is well screened. Finally, the dimensions are larger than the Fermi wavelength, so a quantum mechanical treatment of electron transport is appropriate. When transport occurs without loss of momentum and phase-coherence, it is referred to as ballistic, coherent, or phase-coherent. Good introductions to coherent transport phenomena, including discussions of characteristic length scales, are available in *e.g.* References [63] and [77].

Coherent electron transport is often visualized as shown in Figure 2.2, and can be described using the Landauer approach [77]. The figure shows an open system consisting of two infinitely wide electron reservoirs, each with its own electrochemical potential, μ_L and μ_R , smoothly joined to each other by a narrow constriction that acts as a scattering barrier. When the reservoirs have different electrochemical potentials, as is the case when a finite bias voltage is applied, electrons flow from one reservoir to the other. The infinite width of the reservoirs ensures that they can maintain a finite current with an infinitesimally small current density, and that each reservoir can therefore be regarded as in

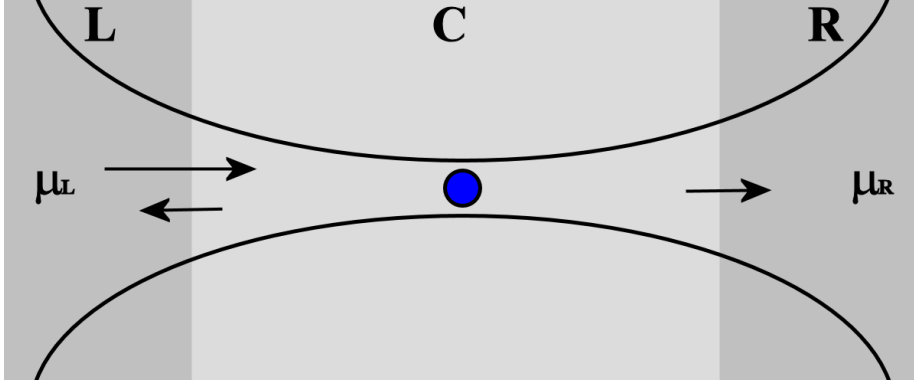


Figure 2.2: Illustration of a scattering mechanism between two electron reservoirs, each with its own electrochemical potential, μ_l and μ_r .

equilibrium⁷.

Electrons incident from one reservoir are scattered off the scattering mechanism, and are either reflected back into the same reservoir or transmitted across to the other. In the Landauer approach the current for a single spin-channel, σ , is given by

$$I_\sigma(V) = \frac{e}{h} \int_{-\infty}^{\infty} T_\sigma(V, E) [f_R(E; \mu_R + eV/2) - f_L(E; \mu_L - eV/2)] dE \quad (2.43)$$

where e is the elementary charge, h is Planck's constant, $T_\sigma(V, E)$ is the transmission coefficient, and $f_L(E; \mu_L - eV/2)$ and $f_R(E; \mu_R + eV/2)$ are the Fermi distributions of the left- and right electrodes, respectively. A positive bias voltage, V , is defined as having the effect of lowering the electrochemical potential in the left electrode by $eV/2$ while increasing the electrochemical potential in the right electrode by the same amount. Consequently, the current is defined as positive when flowing from the left reservoir to the right (electrons flow from right to left). The total current is, of course, the sum of the current in the two spin-channels, $I = I_\uparrow + I_\downarrow$. For low-temperature current calculations the Fermi distributions become step functions and the transmission is integrated over the energy integration window $-eV/2 < E < eV/2$.

The transmission coefficient, $T_\sigma(V, E)$, the calculation of which will be discussed in the following section, can be found by treating the non-equilibrium effects at a given bias voltage self-consistently. An approximation to the current can be obtained by using the transmission coefficient calculated for zero-bias,

$$I_\sigma(V) \approx \frac{e}{h} \int_{-\infty}^{\infty} T_\sigma(0, E) [f_R(E; \mu_R + eV/2) - f_L(E; \mu_L - eV/2)] dE \quad (2.44)$$

For systems in which the electronic structure changes only little with an applied bias voltage this approximation can be acceptable and allow for a significant

⁷The systems discussed in this thesis are not shaped as Figure 2.2, but consist of infinitely wide barriers of finite thickness sandwiched between infinitely wide and infinitely thick reservoirs. The transmission through the barriers is very small, and we consider only equilibrium- and near-equilibrium situations. The reservoirs can therefore "absorb" the small current while remaining (approximately) in equilibrium.

reduction in calculation time. Equation 2.44 is used to calculate the current in magnetic tunnel junctions in this thesis. For analyses of zero-bias electronic properties the conductance for a single spin-channel is given by

$$G_\sigma = \frac{e^2}{h} T_\sigma(0, E_F) \quad (2.45)$$

where $T_\sigma(0, E_F)$ is the zero-bias transmission at the Fermi energy for the given spin. Equation 2.45 is used to calculate zero-bias conductances in magnetic tunnel junctions in this thesis. The total conductance is the sum of the spin-conductances, $G = G_\uparrow + G_\downarrow$.

Our studies involve the use of crystalline, bulk-like electrodes. For such systems the transmission at a given energy can be found for a specific k-vector in the 2D Brillouin zone perpendicular to the transport direction, \mathbf{k}_\parallel , and the total transmission is the integral over the zone,

$$T_\sigma(V, E) = \frac{A}{(2\pi)^2} \int T_\sigma^k(V, E, \mathbf{k}_\parallel) d\mathbf{k}_\parallel \quad (2.46)$$

where A is the area of the central cell in the plane perpendicular to the transport direction and the transmission coefficient is averaged over the two-dimensional Brillouin zone. The Hermitian transmission probability matrix at a given energy and k-vector, $\bar{t}^\dagger \bar{t}$, can be diagonalized [78]

$$\bar{U}_L^\dagger \bar{t}^\dagger \bar{t} \bar{U}_L = \text{diag}(\tau_1, \tau_2, \dots) \quad (2.47)$$

where \bar{U}_L is a unitary matrix and τ_i is a transmission eigenvalue (the transmission probability matrix is defined in the next section). For each transmission eigenvalue, a corresponding transmission eigenstate can be found [78]. The total transmission at a given energy and k-vector can in this way be split into contributions from individual transmission eigenstates,

$$T_\sigma^k(V, E, \mathbf{k}_\parallel) = \sum_i \tau_{\sigma,i}(V, E, \mathbf{k}_\parallel) \quad (2.48)$$

where the spin, voltage, energy, and k-vector dependencies are explicitly written. These analysis options offer a description of conductance useful for interpretation of results [65].

2.6.2 The NEGF method for the modeling of quantum transport

The transmission coefficient, discussed in the previous section, and the electron density, required in the self-consistent procedure used in density functional theory, can be calculated for open systems using non-equilibrium Green's functions (NEGFs) [79]. A brief summary of a NEGF method is presented here, and the reader is referred to the literature for a more complete treatment [63, 64, 65, 77]. The method is based on the partitioned approach by Caroli *et al.* [79], in which the central cell and the two electrodes are disconnected and in equilibrium⁸ before the coupling between the three regions is “turned on” adiabatically [80],

⁸ The electrodes can be biased relative to one another before the coupling is turned on, and the difference in electrochemical potential is maintained after the coupling.

after which the electrodes perturb the central cell, while they themselves are assumed to be unperturbed by the coupling.

The retarded Green's function, \bar{G}^r , for an open system — represented in a basis of localized orbitals — satisfies

$$[(E + i\eta)\bar{S} - \bar{H}]\bar{G}^r = \bar{I} \quad (2.49)$$

where \bar{H} and \bar{S} are the Hamiltonian and overlap matrices, respectively, E is the energy, \bar{I} is a unit matrix, and η is an infinitely small, positive number ($\eta \rightarrow 0^+$). The matrices are infinitely large, as the two electrodes extend to infinity. Equation 2.49 can be written

$$\begin{bmatrix} \bar{\mathcal{H}}_{LL} & \bar{\mathcal{H}}_{LC} & 0 \\ \bar{\mathcal{H}}_{CL} & \bar{\mathcal{H}}_{CC} & \bar{\mathcal{H}}_{CR} \\ 0 & \bar{\mathcal{H}}_{RC} & \bar{\mathcal{H}}_{RR} \end{bmatrix} \begin{bmatrix} \bar{G}_{LL}^r & \bar{G}_{LC}^r & \bar{G}_{LR}^r \\ \bar{G}_{CL}^r & \bar{G}_{CC}^r & \bar{G}_{CR}^r \\ \bar{G}_{RL}^r & \bar{G}_{RC}^r & \bar{G}_{RR}^r \end{bmatrix} = \begin{bmatrix} \bar{I}_{LL} & 0 & 0 \\ 0 & \bar{I}_{CC} & 0 \\ 0 & 0 & \bar{I}_{RR} \end{bmatrix} \quad (2.50)$$

where $\bar{\mathcal{H}}_{\alpha\beta} \equiv (E + i\eta)\bar{S}_{\alpha\beta} - \bar{H}_{\alpha\beta}$ and the block form of the matrices is emphasized: matrices with indices LL , CC , and RR represent sets of matrix elements between non-orthogonal orbitals centered at the left- (L), central- (C), and right (R) regions, respectively, while matrices with indices LC , CL , RC , CR , LR , and RL represent the coupling between the three regions. Note that $\bar{\mathcal{H}}_{\alpha\beta}$ and therefore all other matrices discussed in the following paragraphs are functions of the energy, $\bar{\mathcal{H}}_{\alpha\beta} = \bar{\mathcal{H}}_{\alpha\beta}(E)$; the explicit energy dependence is left out for notational convenience.

Only the central cell block of the retarded Green's function, \bar{G}_{CC}^r , is required to describe the relevant properties of the system [63]. This can be found from

$$\bar{G}_{CC}^r = [\bar{\mathcal{H}}_{CC} - \bar{\Sigma}_{CC}^L - \bar{\Sigma}_{CC}^R]^{-1} \quad (2.51)$$

where

$$\bar{\Sigma}_{CC}^L \equiv \bar{\mathcal{H}}_{CL}\bar{\mathcal{H}}_{LL}^{-1}\bar{\mathcal{H}}_{LC} \quad (2.52)$$

$$\bar{\Sigma}_{CC}^R \equiv \bar{\mathcal{H}}_{CR}\bar{\mathcal{H}}_{RR}^{-1}\bar{\mathcal{H}}_{RC} \quad (2.53)$$

are the retarded self energies for the left- and right regions, respectively. The retarded Green's function describes the coherent evolution of the electron from it is injected into the central cell until it disappears into one of the electrodes [77]. The self energies describe the coupling between the electrodes and the central cell, and the unperturbed electrode Green's functions $\bar{\mathcal{H}}_{LL}^{-1}$ and $\bar{\mathcal{H}}_{RR}^{-1}$ are known as the surface Green's functions. The self energy $\bar{\Sigma}_{CC}^L$ can be interpreted as follows: $\bar{\mathcal{H}}_{CL}$ scatters the electron from the central cell to the left electrode, $\bar{\mathcal{H}}_{LL}^{-1}$ propagates the electron in the electrode, and $\bar{\mathcal{H}}_{LC}$ scatters the electron back into the central cell; a similar interpretation exists for $\bar{\Sigma}_{CC}^R$.

A few quantities, which can be derived from the retarded Green's function and the self energies, are needed to calculate the electron density and the transmission coefficient: The advanced Green's function of the central cell is the Hermitian of the retarded Green's function

$$\bar{G}_{CC}^a = (\bar{G}_{CC}^r)^\dagger \quad (2.54)$$

The advanced Green's function describes the opposite of the retarded Green's function, namely the coherent evolution of the electron as it appears in the central cell (from one of the electrodes). The two Green's functions are well suited

for calculating a physical response, and contain information about densities of states, scattering states, *etc.* [81]. The quantity $\bar{\Sigma}_{CC}^<$, which can be viewed as an electron in-scattering function [77], can be found from

$$\Sigma_{CC}^< = -2i \text{Im} \{ f_L(E) \bar{\Sigma}_{CC}^L + f_R(E) \bar{\Sigma}_{CC}^R \} \quad (2.55)$$

where $f_L(E)$ and $f_R(E)$ are again the Fermi distributions [64]. With these quantities defined, the lesser Green's function, which is directly linked to observables and kinetic properties such as the electron density [81], can be found from

$$\bar{G}_{CC}^< = \bar{G}_{CC}^r \Sigma_{CC}^< \bar{G}_{CC}^a \quad (2.56)$$

and the quantities Γ_{CC}^L and Γ_{CC}^R can be found as the imaginary parts of the self energies,

$$\Gamma_{CC}^L = -2 \text{Im} \{ \bar{\Sigma}_{CC}^L \} \quad (2.57)$$

$$\Gamma_{CC}^R = -2 \text{Im} \{ \bar{\Sigma}_{CC}^R \} \quad (2.58)$$

These quantities are related to the lifetimes of states, *i.e.* to the average time an electron remains in the central cell before escaping out into the electrodes [77].

The electron density of the central cell can now be calculated from

$$n_{CC} = \int_{-\infty}^{\infty} \bar{G}_{CC}^< dE \quad (2.59)$$

and the transmission coefficient can be found from

$$T_{\sigma}^k(V, E, \mathbf{k}_{\parallel}) = \text{Tr} \{ \Gamma_{CC}^L \bar{G}_{CC}^r \Gamma_{CC}^R \bar{G}_{CC}^a \} \quad (2.60)$$

The quantities in this equation are all functions of σ , V , E , and \mathbf{k}_{\parallel} . The transmission probability matrix discussed in relation to the transmission eigenstates is defined $\bar{t}^{\dagger} \bar{t} \equiv \Gamma_{CC}^L \bar{G}_{CC}^r \Gamma_{CC}^R \bar{G}_{CC}^a$. As summarized in Reference [77], the Green's functions, \bar{G}_{CC}^r and \bar{G}_{CC}^a , describe the dynamics of the electrons inside the conductor, taking the effects of the electrodes into account through the self energies, $\bar{\Sigma}_{CC}^L$ and $\bar{\Sigma}_{CC}^R$, while the quantities Γ_{CC}^L and Γ_{CC}^R describe the coupling between the conductor and the electrodes.

The numerical subtleties involved in the implementation of a non-equilibrium Green's function method are far from trivial, and the details are beyond the scope of this thesis. Documentation of the method used in this work can be found in References [63, 64, 65, 74], in which the calculation schemes for the different matrices discussed above are defined. A schematic of the basic calculation flow is shown in the flow chart in Figure 2.3.

2.6.3 Reliability of DFT in describing quantum transport

The NEGF-DFT method used in this work has been implemented in the academic packages McDCal and TranSIESTA, as well as in the commercial packages TranSIESTA-C, Atomistix ToolKit, and Atomistix Virtual NanoLab⁹.

⁹TranSIESTA-C was the name introduced when the company Atomistix was founded to market the method. The package later changed its name to Atomistix ToolKit, and a graphical user interface — called Atomistix Virtual NanoLab — was developed. McDCal continues to be developed at McGill University, and TranSIESTA continues to be developed at the Technical University of Denmark.

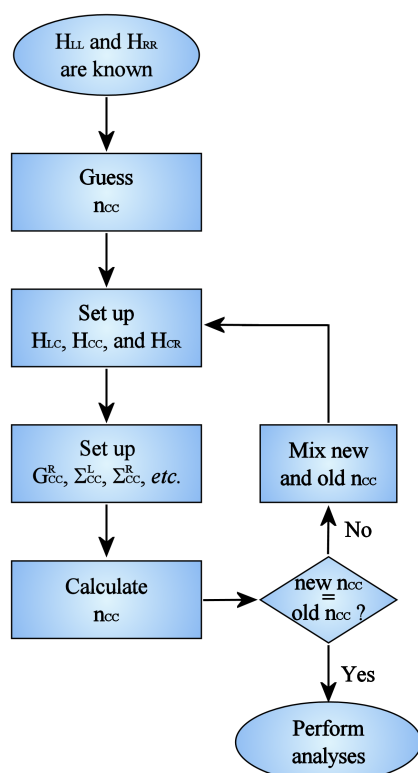


Figure 2.3: Flow chart for the self-consistent field (SCF) treatment of open systems. The electrodes are first treated as bulk systems, providing the Hamiltonian matrices and the corresponding overlap matrices (not shown in the chart) for these. A guess for the electron density of the central cell is then made, and the Hamiltonian matrices (and overlap matrices) for the cell and its coupling to the electrodes are set up. The Green's functions, self energies, *etc.* are then set up, and the electron density is calculated. If the calculated density is identical to the guessed density, the SCF loop is finished and analyses of physical properties can begin. If it is not, the two densities are mixed, the matrices are set up again, and the loop continues until the density converges.

An extensive list of applications of these software packages is available from Atomistix' website [82]. As the packages were developed by groups working within the field of molecular electronics, most references deal with systems relevant for this field. Reference [83] compares calculation results for Gold- and Platinum atomic wires with experimental results, and find a good agreement. The same reference compares results for phenyl-ethynylene oligomers (OPE) sandwiched between Gold electrodes, and find that the device trends are in good agreement, while the calculated conductance is three orders of magnitude larger than the experimental value. These results are representative for comparisons between experiments and calculations: modeling cannot claim to perform numerical investigations of the experimental setups, but can be used to extract general properties of systems, which can shed light on the experimentally observed phenomena [83].

The reason for the failure of modeling to reproduce the quantitative results of experiments within the field of molecular electronics is two-fold: the software does not provide a perfect description of the systems modeled, due to the limitations in the methods used, and the experiments do not provide information about ideal, pure systems, due to the difficulties in achieving perfect experimental conditions. As a consequence, modeling software can be used to predict device trends and understand physics phenomena, but quantitative predictions are presently not reliable.

For the types of systems relevant to this work (magnetic tunnel junctions with Magnesium oxide barriers), it is interesting to note that most of the numerical studies performed to date were done using methods based on density functional theory: Waldron *et al.* [84] and Rungger *et al.* [85] used local-basis NEGF-DFT methods similar to the method used in our work; Wortmann *et al.* [86] used a plane-wave DFT method for the calculation of the electronic structure, and an embedded Green's function method for conductance calculations; Heiliger *et al.* [87] used a DFT method incorporating a screened Korringa-Kohn-Rostoker (KKR) Green's function approach and the atomic sphere approximation (ASA); Butler *et al.* [1, 66, 88, 89] used a layer Korringa-Kohn-Rostoker (KKR) Green's function approach incorporating the local density approximation for the description of the exchange-correlation potential; Belashchenko *et al.* [90] used a tight-binding linear muffin-tin orbital (TB-LMTO) method incorporating the local density approximation and a principal-layer Green's function technique to calculate the conductance; Mathon and Umerski [2] used a tight-binding method for the description of the electronic structure and a Green's function approach for conductance calculations.

As discussed in Reference [91], the "standard" Kohn-Sham density functional theory approach, while approximating non-trivial interactions beyond the electrostatic Hartree interaction, has many limitations when applied to electron transport phenomena (and otherwise). Primarily, one has to accept the Kohn-Sham orbitals as legitimate single particle states, useful in the calculation of scattering phenomena, despite the fact that the orbitals have no such physical interpretation. For practical purposes, however, the use of such methods is advantageous due to the possibility of studying systems of technologically relevant dimensions. The use of the "advanced machinery of quantum chemistry" for such studies currently appears out of reach [91]. It is our goal in this work to give a qualitative, mean-field-like, account of device trends in magnetic tunnel junctions. We use the "standard approach" outlined above, and compare results

with available numerical- and experimental data from the literature.

2.7 Summary

The basic ideas and concepts behind the treatment of many-electron systems have been outlined, starting from the many-body Schrödinger equation, going through the Born-Oppenheimer approximation, the electronic Schrödinger equation, and the variational principle for the ground state energy. The Hartree method and Hartree-Fock theory were then discussed, along with some problems associated with these methods when dealing with large systems. Density functional theory was then introduced, and its reliability in describing systems relevant to this work was discussed. Its use for the modeling of quantum transport phenomena was discussed briefly, and a non-equilibrium Green's function method was outlined.

The chapter serves as a brief introduction to the methods used in this work, and the reader is referred to the references for more in-depth treatments.

Chapter 3

Analyses of bulk materials and magnetic tunnel junctions

In order to understand the properties of the materials and systems of relevance to this work, and simultaneously investigate the reliability of results of calculations performed using Atomistix ToolKit, we have performed a number of analyses and compared results with reference values from the literature.

The analyses consist of calculations of the bulk properties of body-centered cubic Iron (Fe), body-centered cubic Cobalt (Co)¹, and rock salt Magnesium oxide (MgO), as well as a benchmark study of the spin-transport properties of the Fe/MgO/Fe magnetic tunnel junctions investigated by Butler *et al.* [1]. The chapter provides insights into the physical properties of the materials and systems relevant for this thesis, as well as the reliability of the method used.

All calculations are performed using the density functional theory method implemented in Atomistix ToolKit, which uses a linear combination of atomic orbitals (LCAO) basis. The local spin-density approximation (LSDA) is used to approximate the exchange-correlation potential, and the polarized double-zeta (DZP) basis set is used for all elements.

3.1 Analyses of bulk materials

To understand the bulk properties of relevant materials a number of analyses have been performed. Comparisons with results from the literature serve to evaluate the reliability of the software used. The analyses include calculations of equations of state, magnetic moments, band structures, and densities of states for body-centered cubic Fe and Co as well as rock salt MgO, the crystal structures of which are shown in Figure 3.1. Also, the Bloch states propagating in the [001] direction of electrodes and barriers made from these materials, which

¹The room-temperature phase of Co is face-centered cubic, but the body-centered cubic phase is the most relevant for this work, since the magnetic tunnel junctions discussed are grown using this phase.

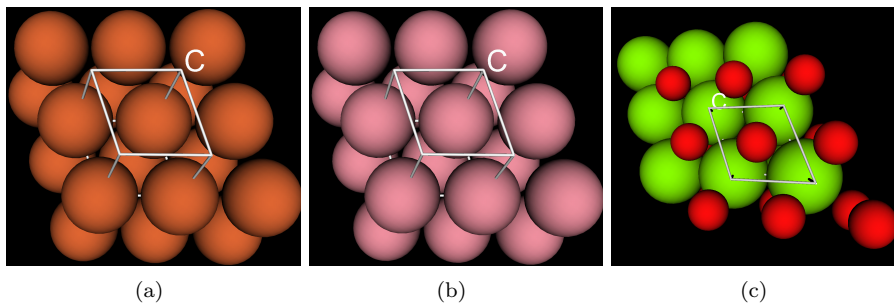


Figure 3.1: Visualizations of body-centered cubic Fe (a), body-centered cubic Co (b), and rock salt MgO (c); $3 \times 3 \times 2$ repetitions of the unit cells are shown along with the cells themselves. Here and throughout the thesis, Fe atoms are shown in brown, Co atoms in purple, Mg atoms in green, and O atoms in red.

turn out to be of great importance for the spin-transport properties of relevant magnetic tunnel junctions, have been studied.

3.1.1 Equations of state

The equations of state, *i.e.* the energy/lattice constant relations, have been calculated for the materials shown in Figure 3.1, and the results are shown in Figure 3.2.

The bulk moduli of the crystals, a measure of their compressibility, can be calculated from the second derivatives of the equations of state, which have been fitted to fourth order polynomial expansions of the calculation data; the results are listed in Table 3.1. Density functional methods employing LDA, including

	Experiment	Theory	This work
Fe	168 GPa [71]	235 GPa [71]	238 GPa
Co	173 GPa [92]	278 GPa [93]	273 GPa
MgO	164 GPa [94]	162 GPa [94]	177 GPa

Table 3.1: Calculated- and reference values (experimental and numerical) of the bulk moduli at the equilibrium lattice constants for body-centered cubic Fe, body-centered cubic Co, and rock salt MgO. The software significantly overestimates the values for Fe and Co, and slightly overestimates the value for MgO.

those used in References [71] and [93] and in this work, significantly overestimate the bulk moduli for Fe and Co, and our method slightly overestimates the value for MgO. These discrepancies are only of minor importance for the analyses in this work, since the distances between atoms in all systems are very close to the equilibrium distances, which — as described presently — are found to be close to the experimental values.

The equilibrium lattice constants, found at the energy minima of the equations of state, are listed in Table 3.2 along with experimental- and numerical reference data from the literature. LDA-DFT methods, including those used in References [71], [93], and [94] and in this work, slightly underestimate the lattice

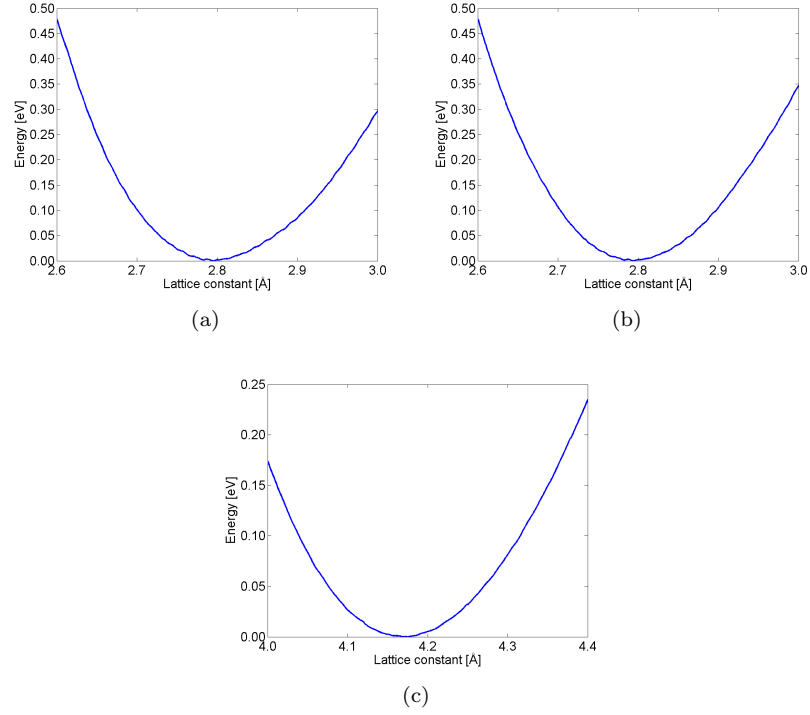


Figure 3.2: Equations of state for body-centered cubic Fe (a), body-centered cubic Co (b), and rock salt MgO (c). Energies are relative to equilibrium values. The calculated values of bulk moduli overestimate the experimental values reported, while the calculated lattice constants slightly underestimate the experimental values.

	Experiment	Theory	This work
Fe	2.87 Å [71]	2.76 Å [71]	2.795 Å
Co	2.82 Å [93]	2.76 Å [93]	2.794 Å
MgO	4.22 Å [94]	4.16 Å [94]	4.180 Å

Table 3.2: Calculated- and reference values (experimental and numerical) of the equilibrium lattice constants for body-centered cubic Fe, body-centered cubic Co, and rock salt MgO. The software slightly underestimates the lattice constants.

constants. The calculation results are all within 3% of the experimental value, which is acceptable for our purposes (and better than the numerical reference data). The calculated lattice constants are used to define the geometries of all systems of interest, as described in Chapter 4.1.

3.1.2 Magnetic moments

The magnetic moments on the atoms in the two magnetic solids can be found from calculations of the Mulliken populations [74] by subtracting the minority-spin population from the majority-spin population. They have been calculated at the respective equilibrium lattice constants, and the results are listed in Table 3.3. LDA-DFT methods, including those used in Reference [93] and this

	Experiment	Theory	This work
Fe	2.22 μ_B [71]	2.05 μ_B [71]	2.01 μ_B
Co	1.7 μ_B [95]	1.726 μ_B [93]	1.68 μ_B

Table 3.3: Calculated- and reference values (experimental and numerical) of the magnetic moments for body-centered cubic Fe and Co. Results are good for Co and reasonable for Fe.

work, provide a good description of the magnetic moment for Co, and the methods used in Reference [71] and this work provide a reasonable description for Fe (both methods slightly underestimate the value). A reasonable description of the magnetic moments of relevant materials is essential, as it is a prerequisite for calculating the (spin-dependent) electronic structure of systems of interest; the calculated values are considered acceptable.

3.1.3 Band structures

The spin-dependent band structures of the three crystals have been calculated at the respective equilibrium lattice constants; the results are shown in Figure 3.3. The calculated band structures for Fe and Co appear qualitatively similar to the ones in References [71] and [96], respectively. The calculated occupied bandwidths (the distances from the Fermi energy to the bottom of the lowest valence bands) are listed in Table 3.4; they are slightly higher than

	Theory (maj/min)	This work (maj/min)
Fe	8.5 eV / 8.1 eV [71]	9.23 eV / 8.83 eV
Co	9.26 eV / 7.42 eV [96]	9.81 eV / 9.51 eV

Table 3.4: Calculated- and reference values (numerical) of the majority- and minority-spin occupied bandwidths for body-centered cubic Fe and Co. The calculation results are reasonable.

the values reported in the references, but the exchange splitting (the difference between the occupied bandwidth of majority- and minority-spin electrons) for Fe is in good quantitative agreement. The exchange splitting for Co is significantly lower than the reference value, although closer to the experimental value

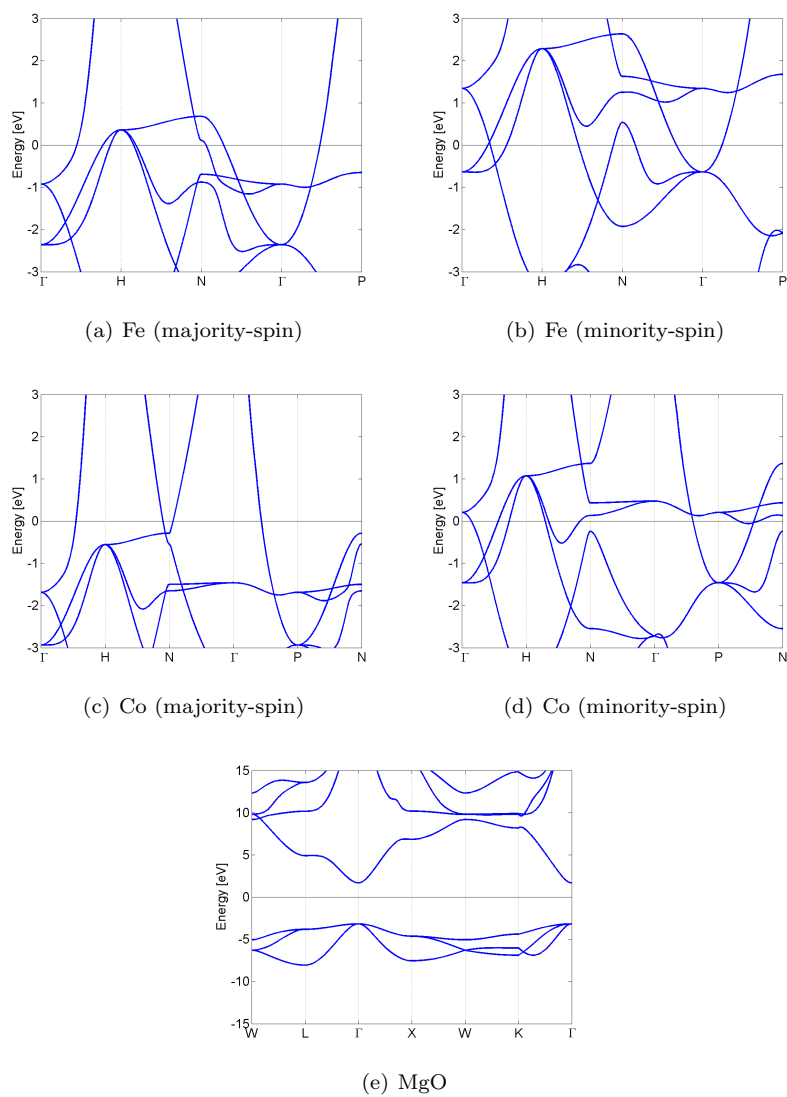


Figure 3.3: Band structures for majority- and minority-spin electrons in body-centered cubic Fe (a and b), body-centered cubic Co (c and d), and rock salt MgO (e). Energies are relative to the Fermi energy. The band structures are in good qualitative agreement with those reported in the literature.

of 0.85 eV [96]. These differences are due to differences in methods and the basis sets used.

The band structure for MgO is in good qualitative agreement with that reported in Reference [97], but the shape of high-energy conduction bands disagrees slightly with that in Reference [98]. This disagreement can be attributed to the different methodologies and perhaps to the limitations of the basis set², but as we are mainly interested in calculating the zero- and low bias conductance and current the details of high energy bands (far away from the Fermi energy) are not critical. As for quantitative results, the calculated band gap of MgO is 4.86 eV, which is significantly smaller than the experimental value of 7.8 eV. This discrepancy is typical for LDA calculations [98] and — as discussed in Section 2.5 — for Kohn-Sham DFT calculations in general. The calculated width of the valence band is 4.88 eV, which is consistent with the results in Reference [98].

For our purposes, the shape and position of band structures near the Fermi energy are important, since all zero- and low-bias electronic properties of open systems depend critically on these. As the results for Fe and Co appear similar to those from the references near the Fermi energy, we are confident that the software provides a reasonable description of the materials. Also, the Bloch states found to be propagating perpendicular to the interfaces in relevant open systems are, as discussed in Section 3.1.5, consistent with those described in the literature. The calculated band gap of MgO is, as mentioned, significantly smaller than the experimental value. It is, however, sufficiently large to ensure severe damping of Bloch states propagating through the material with energy near the Fermi energy, and therefore ensures that the transmission through barriers of such material is very low; this is of vital importance, as described in Section 3.2.2.

3.1.4 Densities of states

At the time of writing, there is no feature available for calculating densities of states in Atomistix ToolKit. The data can, however, be extracted from band structure calculations, in which the Brillouin zone has been fully sampled, by counting the number of states with energies within each of a number of finely distributed energy intervals.

The spin-dependent densities of states of the three crystals have been calculated at the respective equilibrium lattice constants, and the results are shown in Figure 3.4; they are in agreement with the ones in References [99], [93], and [100], respectively. Also shown in Figure 3.4 is the spin polarization of the two magnetic crystals, defined as

$$P(E) = \frac{n_{\uparrow}(E) - n_{\downarrow}(E)}{n_{\uparrow}(E) + n_{\downarrow}(E)} \quad (3.1)$$

where $n_{\uparrow}(E)$ and $n_{\downarrow}(E)$ are the majority- and minority-spin densities of states, respectively. As mentioned in Section 1.3, the Julliere model relates the tunneling magnetoresistance with the polarization at the Fermi energy.

²We have performed band structure calculations using different exchange-correlation potentials, basis sets, mesh cut-offs, and energy shifts without observing significant changes in the shape of the conduction bands.

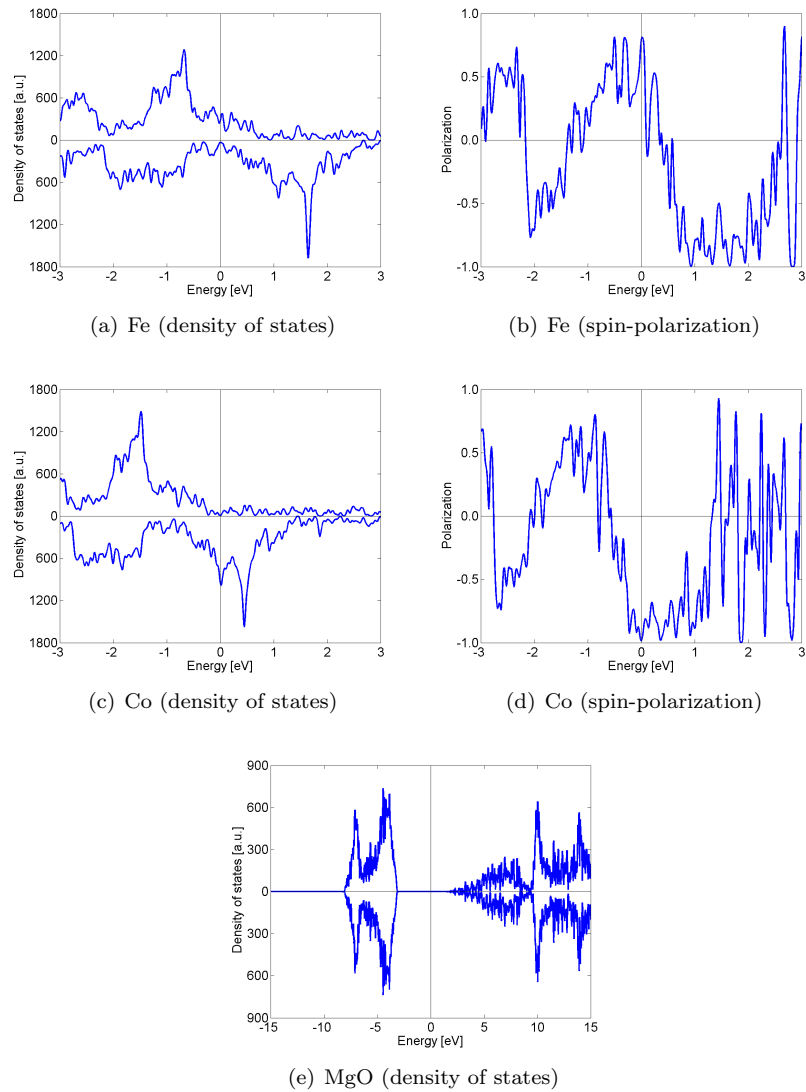


Figure 3.4: Densities of states for majority- and minority-spin electrons (plotted on the negative axis) in body-centered cubic Fe (a), body-centered cubic Co (c), and rock salt MgO (e), along with the spin polarization of Fe (b) and Co (d). The densities of states are in good qualitative agreement with those reported in the references. Note the high Fermi-energy polarization for Fe and Co (negative for the latter).

3.1.5 Electrode Bloch states with $\mathbf{k}_{\parallel} = 0$

The magnetic tunnel junctions discussed in this thesis are based on body-centered cubic Iron (Fe), Cobalt (Co), or Iron-Cobalt (FeCo) electrodes, set up with the (001) surfaces interfacing system barriers³. The unit cells of these electrodes are shown in Figure 3.5. The properties of Bloch states propagat-

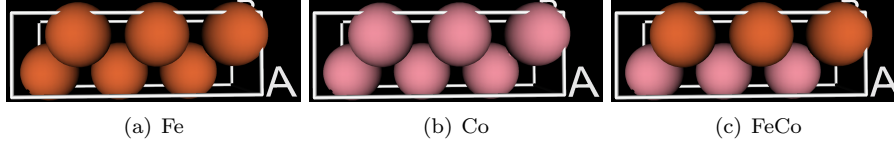


Figure 3.5: Body-centered cubic Fe, Co, and FeCo electrodes with six atoms in the unit cells and the (001) surfaces arranged parallel to the xy -plane. The dimensions of the unit cells are denoted by $a \times a \times c$. These electrodes are used throughout this work.

in the [001] direction (*i.e.* perpendicular to the (001) surfaces) in these electrodes are, as discussed in Section 3.2.2, of critical importance and will be described here.

The spin-dependent band structures of the body-centered cubic Fe, Co, and FeCo electrodes along the [001] direction (with $\mathbf{k}_{\parallel} = (\mathbf{k}_x, \mathbf{k}_y) = 0$) are shown in Figure 3.6⁴. Four bands cross the Fermi energy for both majority- and minority-

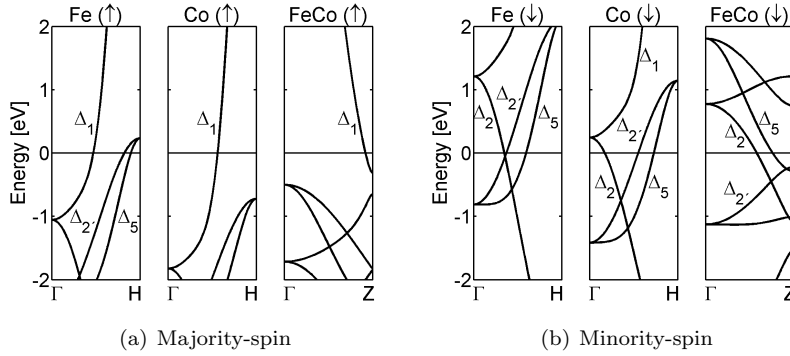


Figure 3.6: Majority- and minority-spin band structures of the Fe, Co, and FeCo electrodes in the [001] direction for $\mathbf{k}_{\parallel} = \mathbf{0}$. The energies are relative to the Fermi energy.

spin electrons in Fe⁵, and eight Bloch states with $E = E_F$ and $\mathbf{k}_{\parallel} = 0$ therefore propagate in the [001] direction. These states are visualized in Figure 3.7. The [001] direction is known as the Δ direction, and the states are therefore referred to as Δ_1 , Δ_5 , *etc.* [101]. Only Δ_1 bands cross the Fermi energy for

³The FeCo electrode actually has B2 strukturbericht structure, which is identical to the body-centered cubic structure with two different atomic elements.

⁴The band structures are calculated from the Γ point, (0,0,0), to the H point, (0.5, -0.5, 0.5), for the body-centered cubic Fe and Co electrodes and from the Γ point to the Z point, (0, 0, 0.5), for the B2 FeCo electrode. In all three cases the energies of the states

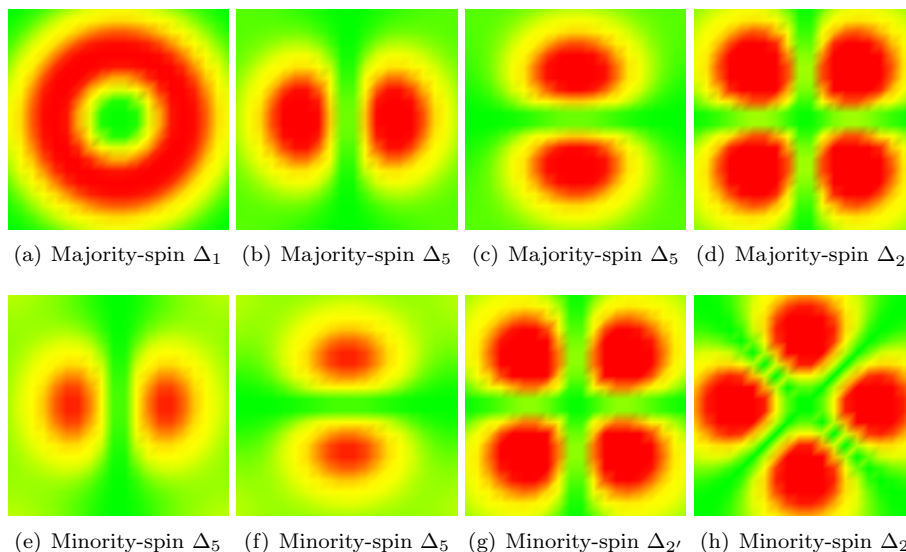


Figure 3.7: Bloch states with $E = E_F$ and $\mathbf{k}_{\parallel} = 0$, visualized on the xy -plane through the left-most Fe atom in the electrode unit cell (only a quarter of the unit cell is shown). Red color indicates high absolute value of the wave function, yellow indicates medium value, and green indicates zero value. The four majority-spin states have Δ_1 , Δ_5 , and $\Delta_{2'}$ symmetry, while the minority-spin states have Δ_5 , $\Delta_{2'}$, and Δ_2 symmetry [1].

majority-spin electrons in the Co and FeCo electrodes, and Δ_5 and Δ_2 bands cross for minority-spin electrons. In the Co electrode a minority-spin $\Delta_{2'}$ band also crosses. As discussed in Section 3.2.2 the symmetries of the states are very important for their spin-transport properties when the electrodes are used in magnetic tunnel junctions; the Δ_1 state turns out to be the dominant source of conduction. The four types of states are visualized three-dimensionally in Figure 3.8. All of the above calculation results are consistent with the results in References [1], [66] and [31] (the minority-spin Δ_2 state in Co is mentioned in Reference [31] but not in [66]).

3.2 Analyses of magnetic tunnel junctions

To understand the properties of magnetic tunnel junctions a number of analyses have been performed on the Fe/MgO systems studied extensively by Butler *et al.* [1]. Comparisons with results from the original work and other references serve to evaluate the reliability of the software used. Analyses include calculations of charge redistribution, surface magnetic moments, transmission spectra, and transmission eigenstates. A brief analysis of tunneling of free electrons across a simple potential barrier further illustrates the basic physics, as does a brief analysis of the effects of increasing the number of barrier layers in the system.

propagating perpendicular to the electrode/barrier interfaces are found.

⁵The Δ_5 bands are doubly degenerate.

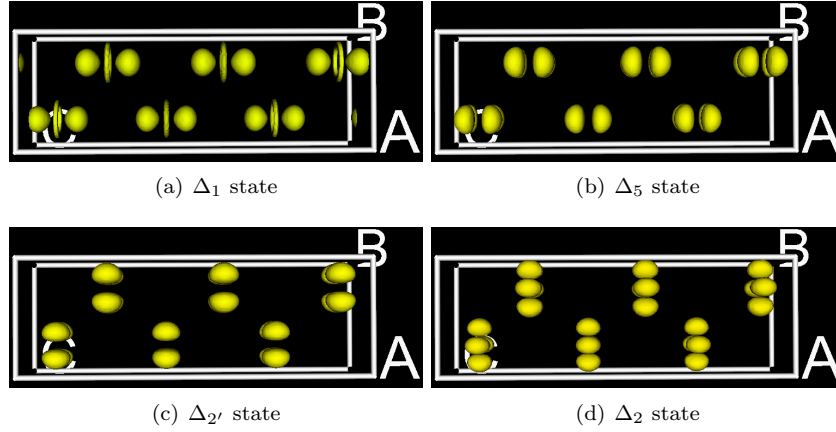


Figure 3.8: Three-dimensional visualization of Δ_1 , Δ_5 , $\Delta_{2'}$, and Δ_2 states. The states are plotted as iso-surfaces at appropriate wave function amplitudes. The different symmetries of the states are responsible for their different spin-transport properties in magnetic tunnel junctions; the Δ_1 state dominates conduction.

The unit cell of the system is shown in Figure 3.9. The system consists of four

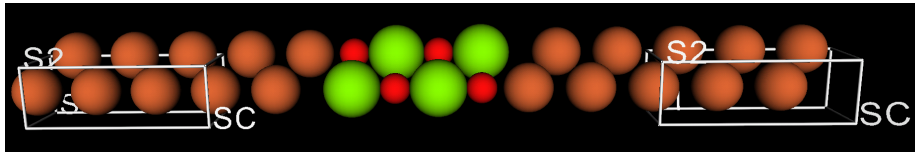


Figure 3.9: Fe/MgO magnetic tunnel junction, consisting of four MgO layers sandwiched between body-centered cubic Fe electrodes arranged with the (001)-surfaces facing the (001)-surfaces of the barrier. (Geometry courtesy of Professor Butler).

layers of MgO sandwiched between six-atom body-centered cubic Fe electrodes, and four screening layers are included on each side of the barrier; the unit cell is repeated indefinitely in the xy -plane. While this perfect in-plane crystallinity is somewhat idealized, such systems can be grown with very high epitaxial quality using molecular beam epitaxy (MBE) and microfabrication techniques [11, 42], and the use of periodic boundary conditions is therefore reasonable. As a consequence, the in-plane linear momentum is conserved during tunneling, *i.e.* \mathbf{k}_{\parallel} remains unaltered across the system for a given transmission eigenstate. The geometry is based on coordinates received from Professor Butler, and the original work also include analyses of systems with eight and 12 barrier layers; comparison with these results are mentioned briefly at the end of the chapter.

3.2.1 Charge redistribution and magnetic moments

Figure 3.10 shows the self-consistently calculated charge redistribution in the system. Only the charge on the central region atoms is calculated, so the figure shows the charge for the four screening layers (Fe) on each side of the four barrier

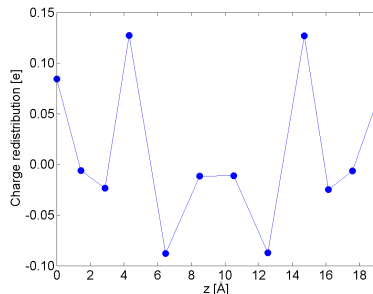


Figure 3.10: Charge redistribution in the system. There is only little charge transfer between the Fe electrodes and the MgO barrier.

layers (MgO). The redistribution is necessary to correctly offset the bands of the MgO barrier relative to those of the Fe electrodes [1]; it is calculated as the difference between the charge on each layer and the charge of the corresponding neutral atoms (negative values correspond to extra electrons).

The figure looks qualitatively similar to the results in the original work in the center of the barrier, while there are differences near the outer Fe atoms, most likely due to differences in methodology⁶. The conclusion is consistent: there is only little charge transfer between the Fe electrodes and the MgO barrier [1], which is also consistent with the results in [102].

The calculated magnetic moment of the Fe atoms closest to the MgO barrier is $2.92 \mu_B$, consistent with the results in References [1, 102], and close to the value of a free Fe surface ($2.96 \mu_B$ [102]). This surface-like magnetic moment, along with the small charge transfer, indicates a weak electronic interaction between the electrodes and the barrier [1, 102].

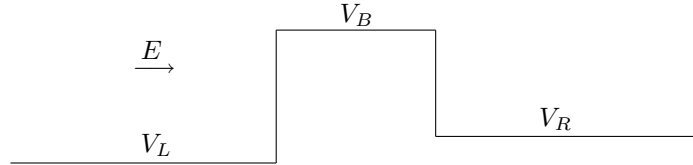
3.2.2 Transmission spectra and transmission eigenstates

Analyses of the transmission for different values of the in-plane k-vector (\mathbf{k}_\parallel) at the Fermi energy provide an understanding of the zero-bias electronic properties of magnetic tunnel junctions. To establish such an understanding, the transmission spectra, $T(\mathbf{k}_\parallel)$, for the magnetic tunnel junction in the parallel- and anti-parallel magnetization configurations have been calculated, and the transmission eigenstates contributing to spin-transport with $\mathbf{k}_\parallel = \mathbf{0}$ (which turn out to dominate the conductance in the parallel magnetization configuration) have been analyzed. The results are described presently, after a brief discussion of a simple and illustrative free-electron model.

Simple free-electron model

Consider the simple one-dimensional potential landscape below,

⁶Calculation results are consistent with results for the systems with eight and 12 barrier layers discussed in Section 3.2.2.



representing the potential for a single spin channel. The potential can, for example, represent a three-dimensional homogeneous insulating slab sandwiched between semi-infinite homogeneous metallic leads (such as a magnetic tunnel junction described macroscopically). Free electrons with energy E propagate from infinity to the potential barrier, in which their wave functions decay, before the electrons exit and propagate towards infinity on the other side.

As discussed in Reference [38] the transmission through this system is

$$T(\mathbf{k}_{\parallel}) = \frac{16k_1\kappa^2k_2e^{2d\kappa}}{[\kappa(k_1+k_2)(1+e^{2d\kappa})]^2 + [(\kappa^2-k_1k_2)(1-e^{2d\kappa})]^2} \quad (3.2)$$

where

$$k_1 = k_{z,L}(\mathbf{k}_{\parallel}) = \sqrt{\frac{2m_e}{\hbar^2}(E - V_L - \mathbf{k}_{\parallel}^2)} \quad (3.3)$$

$$\kappa = \kappa_{z,B}(\mathbf{k}_{\parallel}) = \sqrt{\frac{2m_e}{\hbar^2}(V_B - E + \mathbf{k}_{\parallel}^2)} \quad (3.4)$$

$$k_2 = k_{z,R}(\mathbf{k}_{\parallel}) = \sqrt{\frac{2m_e}{\hbar^2}(E - V_R - \mathbf{k}_{\parallel}^2)} \quad (3.5)$$

are the z -component of the \mathbf{k} -vector on the left side, the damping coefficient in the barrier, and the z -component of the \mathbf{k} -vector on the right side, respectively, d is the thickness of the barrier, and $E > V_L$, $E < V_B$, and $E > V_R$. When the transmission is small the equation can be approximated by

$$T(\mathbf{k}_{\parallel}) \approx \frac{16k_1\kappa^2k_2e^{-2d\kappa}}{[\kappa(k_1+k_2)]^2 + [(\kappa^2-k_1k_2)]^2} \quad (3.6)$$

since $d\kappa \gg 1$.

Equation 3.6 is plotted in Figure 3.11 for $V_L = V_R = 0.00$ eV, $V_B = 1.30$ eV, $E = 0.92$ eV, and $d \approx 6.1$ Å; the thickness corresponds to the width of the barrier in the system, and the potentials are chosen to fit the data in Section 3.2.2. The figure shows that the transmission is strongest in the center of the spectrum (near $\mathbf{k}_{\parallel} = \mathbf{0}$), and that it quickly falls to zero when moving away from the center. Phenomenologically, this result is intuitive: electrons with a certain energy have a greater probability of penetrating the barrier if their momentum is perpendicular to the interface than if the momentum is at an odd angle. While spin-transport in realistic systems is more complex this simple and intuitive model provides a very good starting point for understanding the electronic properties of magnetic tunnel junctions; a more complex treatment follows presently.

Magnetic tunnel junction in parallel magnetization configuration

An understanding of the spin-transport properties of a magnetic tunnel junction naturally begins with the study of the transmission spectra of the system

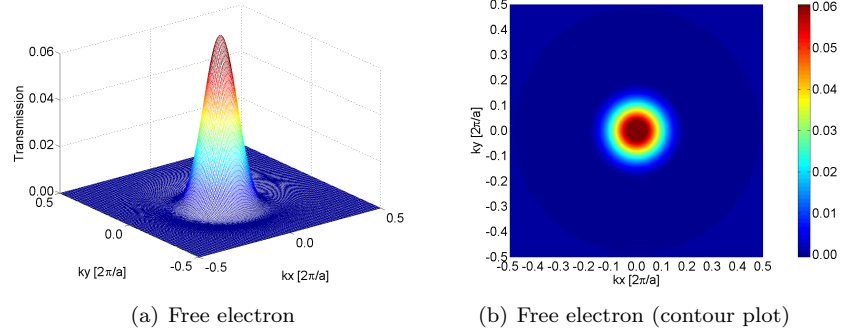


Figure 3.11: Transmission spectrum for free electrons incident on a simple potential barrier. Spin-transport is dominated by electrons with small k -vectors in the plane of the interfaces.

of interest. Figure 3.12 shows the calculated zero-bias transmission spectra for the system in the parallel magnetization configuration, *i.e.* in the setup where the electrodes have been magnetized in the same direction⁷. Consistent with

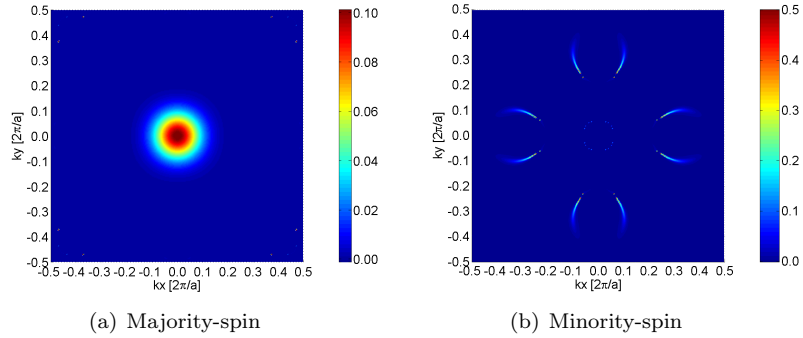


Figure 3.12: Transmission spectra for the system in the parallel magnetization configuration for majority- (a) and minority-spin electrons (c). The majority-spin spectrum is dominated by a peak near $\mathbf{k}_{\parallel} = \mathbf{0}$, while the minority-spin spectrum is dominated by a number of sharp spikes.

the results in the original work, majority-spin conductance (*i.e.* conductance of electrons aligned parallel to the electrode magnetizations) is found to be dominated by electrons with small k -vectors in the plane of the interfaces, *i.e.* by electrons with $\mathbf{k}_{\parallel} \approx \mathbf{0}$, while minority-spin conductance (*i.e.* conductance of electrons aligned opposite to the electrode magnetizations) is dominated by a number of sharp spikes. The majority-spin spectrum strongly resembles the spectrum found for free electrons, indicating that spin-transport occurs through a simple tunneling process, while the spikes in the minority-spin spectrum are

⁷Atomistix ToolKit treats electron spins in a collinear approximation, and the magnetization is therefore either parallel or anti-parallel. Angles other than 0 and π are not possible in the current version of the software.

indicative of tunneling through complex interface resonance states [1]. Qualitatively, both the majority- and minority-spin transmission spectra look similar to those found by Butler *et al.*; quantitatively, the height of the majority-spin peak is found to be ≈ 0.10 , in good agreement with the reported value of ≈ 0.07 .

By evaluating the transmission eigenstates contributing to conductance we can develop an understanding of the underlying tunneling mechanisms. Figure 3.13 shows the eight transmission eigenstates contributing to conduction with $\mathbf{k}_{\parallel} = \mathbf{0}$. Consistent with the findings in the original work the results show

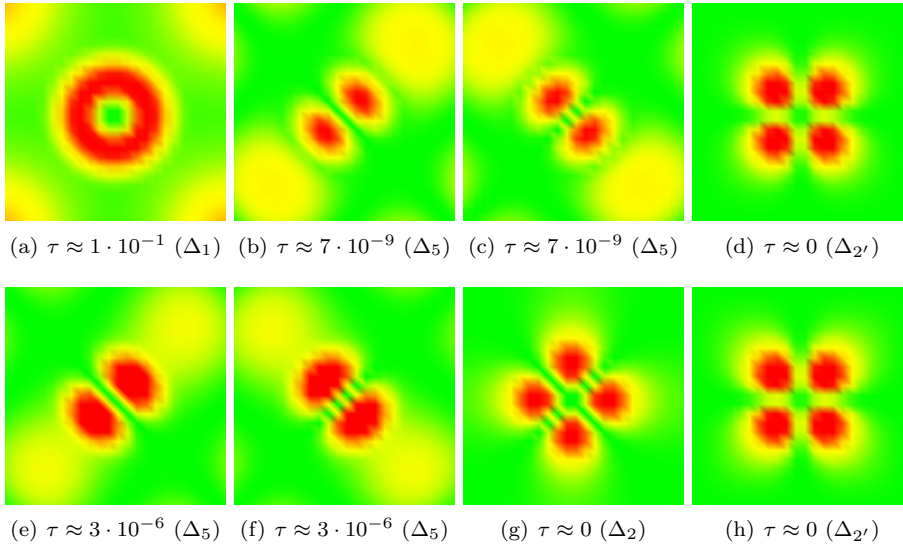


Figure 3.13: Transmission eigenstates for the system in the parallel magnetization configuration for majority- (a,b,c,d) and minority-spin electrons (e,f,g,h), calculated for $E = E_F$ and $\mathbf{k}_{\parallel} = \mathbf{0}$ and plotted on the xy -plane through the left-most Fe atom in the central region. The transmission eigenvalues of the states are given below each visualization; eigenvalues smaller than $\tau \approx 10^{-9}$ are represented by $\tau \approx 0$, as the finite numerical accuracy of calculations renders the exact calculated values meaningless. The Δ_1 mode visualized in (a) is the biggest contributor to the conductance.

that four modes are available for each of the electron spins: for majority-spin electrons one mode with Δ_1 symmetry conducts much better than the others, while two degenerate modes with Δ_5 symmetry conduct relatively poorly and one mode with $\Delta_{2'}$ symmetry almost does not conduct at all; for minority-spin electrons two degenerate modes with Δ_5 symmetry conduct relatively poorly, and two modes with Δ_2 and $\Delta_{2'}$ symmetry almost do not conduct at all. These differences in conduction can be understood from the description in Reference [101], in which the curvature of wave functions in the plane of the electrode/barrier interfaces is shown to lead to increased decay rates when tunneling through the barrier. Basically, the more nodes a mode has in this plane the faster it decays. In this way tunneling with in-plane curvature is like tunneling with non-zero \mathbf{k}_{\parallel} . The Δ_5 modes (with one node per unit cell) therefore decay faster than Δ_1 states (with no nodes), and $\Delta_{2'}$ and Δ_2 states (with two nodes per unit cell) decay even faster.

It should be noted that the calculation of minority-spin conductance in the parallel magnetization configuration is difficult. Due to the sharpness of the spikes in the transmission spectra an extremely high k-point resolution must be used to properly sample the Brillouin zone. We have reported on results of convergence studies in Reference [15]. In this work a resolution of 301×301 k-points is used. Fortunately, the sharpness of the spikes also means that they contribute only little to the total conductance, and that the importance of the resulting lack of precision is therefore limited. The conductance in the parallel configuration is completely dominated by the majority-spin channel. It should also be noted that the interface resonance states giving rise to these spikes appear to be very sensitive to the details of the Fe/MgO interfaces [1, 86], and that introducing “disorder” in the system geometry may have significant effects on the calculated conductances. We have reported on results of investigations of such effects in Reference [14].

Magnetic tunnel junction in anti-parallel magnetization configuration

Analogous to Figure 3.12 Figure 3.14 shows the zero-bias transmission spectra for the magnetic tunnel junction in the anti-parallel magnetization configuration, *i.e.* the configuration in which the electrodes are magnetized in opposite directions. Consistent with the findings in the original work conductance in

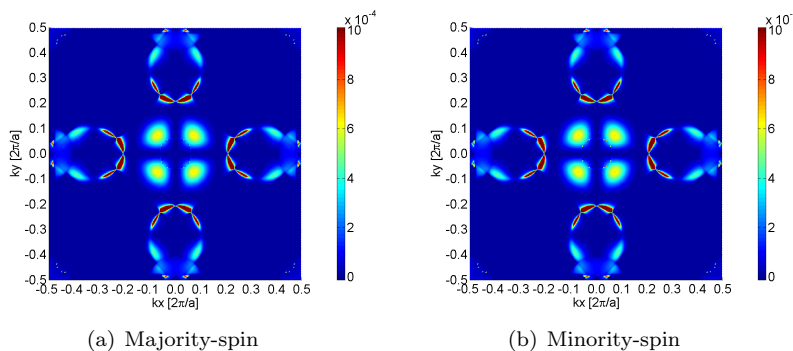


Figure 3.14: Transmission spectra for the two spin-channels in the anti-parallel magnetization configuration. Both spectra are dominated by a number of sharp spikes.

this configuration is found to occur through a combination of the features observed for majority- and minority-spin electrons in the parallel magnetization configuration. The spectra are dominated by a number of sharp spikes. The spectra are identical due to the mirror symmetry of the system, and the designations “majority-” and “minority-spin” refer, by definition, to the left electrode (majority-spin electrons in the left electrode are minority-spin electrons in the right and *vice versa*).

Figure 3.15 shows the eight transmission eigenstates with $\mathbf{k}_{\parallel} = \mathbf{0}$ contributing to conduction in this configuration. Consistent with the original findings the results show that the degenerate Δ_5 states remain available for spin-transport, while the Δ_1 state conducts extremely poorly in this configuration. The Δ_5

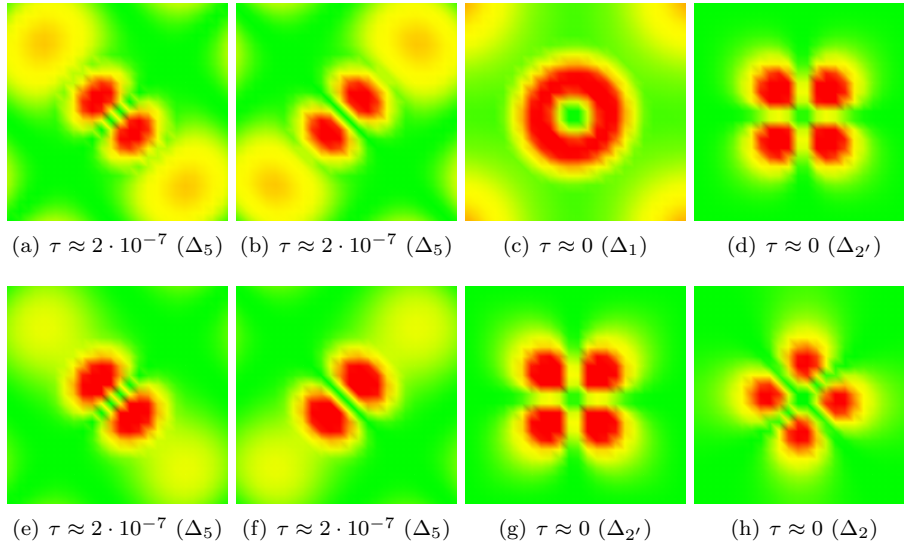


Figure 3.15: Transmission eigenstates for the system in the anti-parallel magnetization configuration for majority- (a,b,c,d) and minority-spin electrons (e,f,g,h), calculated for $E = E_F$ and $\mathbf{k}_{\parallel} = \mathbf{0}$ and plotted on the xy -plane through the left-most Fe atom in the central region. All the eigenstates conduct very poorly.

modes exist in the bulk electrodes for both electron spins, and can therefore tunnel from one electrode to the other. The same goes for the $\Delta_{2'}$ mode. The Δ_1 mode, on the other hand, exists only for majority-spin electrons and cannot couple into a state of the same symmetry when arriving at the opposite electrode, why it continues to decay in this⁸. The same goes for the Δ_2 state. The total conductance for the anti-parallel configuration is therefore much lower than for the parallel configuration: the dominating Δ_1 mode is “killed”, and only the poorly conducting Δ_5 and $\Delta_{2'}$ modes are left (along with the interface resonances). This is why the Fe/MgO magnetic tunnel junction and similar systems has such high tunneling magnetoresistance. As will be discussed in Chapters 5 and 6 the spin-transport properties in the anti-parallel configuration are more complex than indicated in the above (especially when a finite bias voltage is applied), and we emphasize the importance of tunneling with $\mathbf{k}_{\parallel} \neq \mathbf{0}$.

Systems with eight and 12 barrier layers

Figure 3.16 shows the majority-spin transmission spectra for the three systems in the parallel magnetization configuration along with results calculated using the free-electron model for barriers of identical thicknesses. The results found using Atomistix ToolKit are consistent with results in the original work and show trends very similar to those for the free electron model.

We observe the following: 1) the majority-spin conductance in the parallel magnetization configuration decreases exponentially with the thickness of the

⁸For $\mathbf{k}_{\parallel} = \mathbf{0}$ only states of the same symmetry couple. For $\mathbf{k}_{\parallel} \neq \mathbf{0}$, as discussed later in the chapter, there is no such symmetry conservation.

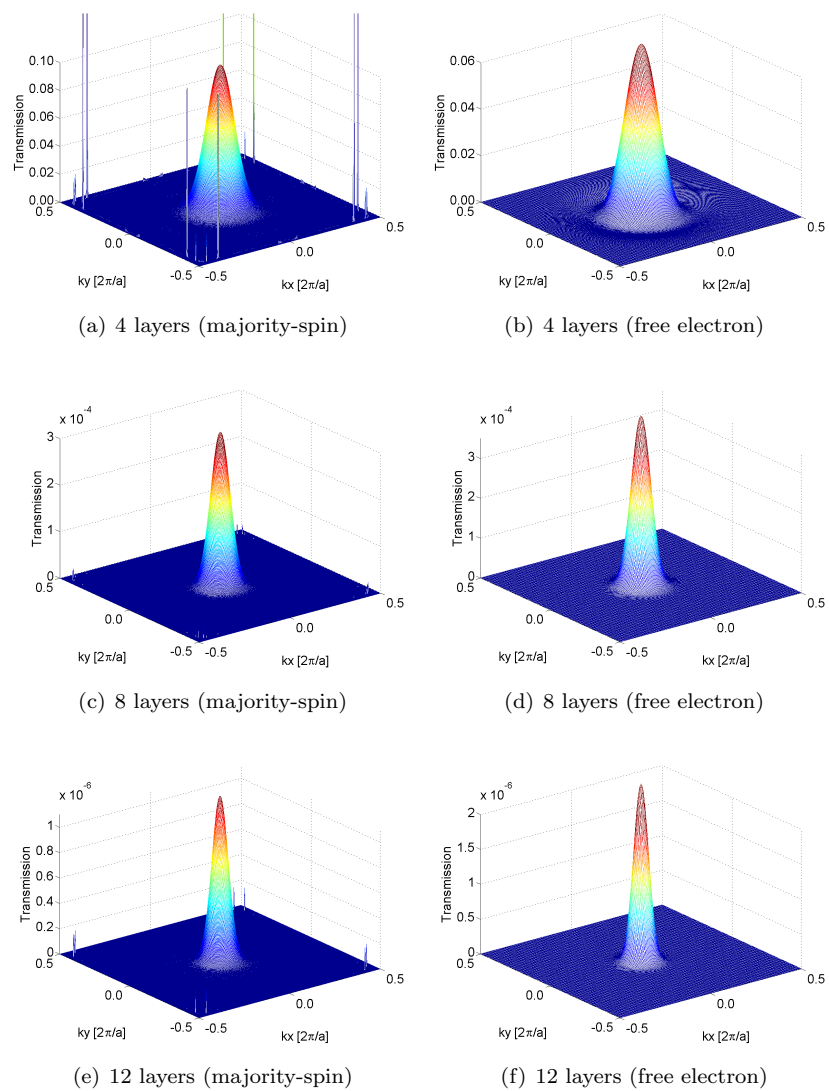


Figure 3.16: Majority-spin transmission spectra for the systems with four- (a), eight- (c), and 12 barrier layers (e) in the parallel magnetization configuration, along with spectra calculated using the free-electron model for barriers of identical thicknesses (b,d, and f). Figures (a) and (b) are identical to Figures 3.12a and 3.11a, respectively.

barrier, 2) the majority-spin conductance is much larger than minority-spin conductance in the parallel magnetization configuration, and 3) the conductance in the parallel magnetization configuration is much larger than the conductance in the anti-parallel magnetization configuration (the tunneling magnetoresistance is found to be thousands of percent for all systems). These statements are in agreement with the original work.

Transmission with $\mathbf{k}_{\parallel} \neq \mathbf{0}$

The preceding analyses in this chapter have focused on transmission with $\mathbf{k}_{\parallel} = \mathbf{0}$, for which the symmetry of Bloch states incident on a barrier is maintained throughout the tunneling process [101]. For $\mathbf{k}_{\parallel} \neq \mathbf{0}$ the situation is more complicated: the states in the barrier consist of linear combinations of tunneling states which decay at different rates when propagating through the barrier [101].

Reference [103] captures some of this complexity in a simple analytic model, which can be seen as an extension of the free-electron model discussed earlier in this section. The transmission away from $\mathbf{k}_{\parallel} = \mathbf{0}$ is found to be determined by the balance between the strength of the exponential decay factor and the interface band coupling, both of which are functions of \mathbf{k}_{\parallel} . The former increases with \mathbf{k}_{\parallel} , as described in Equation 3.4. The latter is unity in the parallel magnetization configuration and proportional to \mathbf{k}_{\parallel} in the anti-parallel configuration [103] (which gives rise to a $|\mathbf{k}_{\parallel}|^2$ dependence in the transmission); it is a measure of the coupling between states of different symmetry across the electrode/barrier interfaces. The transmission as function of \mathbf{k}_{\parallel} for the system with 12 barrier layers, calculated using Equation 3.6 modified by a $|\mathbf{k}_{\parallel}|^2$ dependence, is shown in Figure 3.17. The figure clearly shows how the influence of the interface band

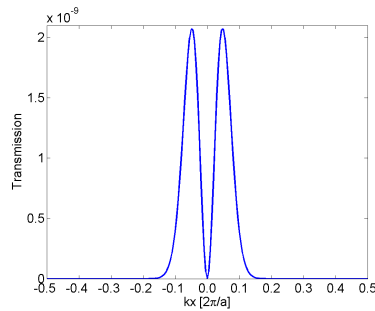


Figure 3.17: Transmission as function of \mathbf{k}_{\parallel} in the system with 12 barrier layers. The transmission is calculated using the free-electron model modified by a \mathbf{k}_{\parallel}^2 dependence due to the influence of interface band coupling. The spectrum shows clear evidence of a transmission peak at $\mathbf{k}_{\parallel} \neq \mathbf{0}$.

coupling shifts the transmission peak to a finite value of \mathbf{k}_{\parallel} .

Figure 3.18 shows the transmission spectrum for the anti-parallel magnetization configuration of the system with 12 barrier layers, calculated using Atomistix ToolKit. As expected from the discussion above, and consistent with the results in the original work, the spectrum shows clear evidence of tunneling with $\mathbf{k}_{\parallel} \neq \mathbf{0}$ as it has four relatively wide peaks located at $\mathbf{k}_{\parallel} \approx (0.075, 0.075)$ and its three symmetry points. These peaks are much wider than the spikes

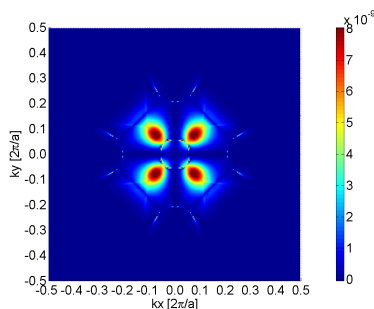


Figure 3.18: Transmission spectrum for the anti-parallel magnetization configuration of the system with 12 barrier layers. Spin-transport occurs largely through states with $\mathbf{k}_{\parallel} \neq \mathbf{0}$, and the spectrum has four relatively wide peaks located at $\mathbf{k}_{\parallel} \approx (0.075, 0.075)$ and its three symmetry points along the lines where $|\mathbf{k}_x| = |\mathbf{k}_y|$.

caused by interface resonance states, and they appear qualitatively like the Δ_1 peak for majority-spin electrons in the parallel magnetization configuration. Their height is, however, approximately two orders of magnitude smaller than that of the Δ_1 peak. In the systems analyzed in Chapters 5 and 6 the peaks are the main contributors to the conductance and current in the anti-parallel configuration.

Note that the analytic model discussed above does *not* account for the variation in transmission for different values of k_x and k_y at a given value of $|\mathbf{k}_{\parallel}|$. Due to the free-electron nature of the description, which does not take into account the atomic geometry of systems, the model does *not* capture the existence of the four peaks in the transmission spectrum for the anti-parallel configuration but merely identifies the fact that interface band coupling leads to finite transmission away from $\mathbf{k}_{\parallel} = \mathbf{0}$.

3.3 Summary

The properties of materials and systems of interest to this work have been investigated, and results have been compared with the literature. We find that Atomistix ToolKit generally provides a good description of relevant properties, and that it in particular finds results consistent with the original work on the three magnetic tunnel junctions.

The zero-bias spin-transport properties of Fe/MgO/Fe magnetic tunnel junctions are found to be dominated by tunneling of Δ_1 states, which decay much slower than Δ_5 , $\Delta_{2'}$, and Δ_2 states inside the barrier. All of these states propagate perpendicular to the interfaces with $E = E_F$ and $\mathbf{k}_{\parallel} = \mathbf{0}$. The Δ_1 states are available for majority-spin electrons in body-centered cubic Fe, but are not available for minority-spin electrons. The zero-bias conductance is therefore much larger for majority- than for minority-spin electrons in the parallel magnetization configuration, and the conductance in the parallel magnetization configuration is much larger than in the anti-parallel magnetization configuration. While the spin-transport properties in the parallel configuration are dominated by states with $\mathbf{k}_{\parallel} = \mathbf{0}$ tunneling of states with $\mathbf{k}_{\parallel} \neq \mathbf{0}$ contribute significantly to conductance in the anti-parallel configuration.

The “tools” available for analyzing such systems are mainly transmission spectrum calculations and analyses of transmission eigenstates. These will be used to investigate the spin-transport properties of other magnetic tunnel junctions in the following chapters.

Chapter 4

Structural properties of MgO-based tunnel junctions

The set up of three magnetic tunnel junctions with Magnesium oxide (MgO) barriers and Iron (Fe), Cobalt (Co), and Iron-Cobalt (FeCo) electrodes is described in this chapter along with results for their structural, charge redistribution, and magnetic properties. The systems are:

- Fe/MgO/Fe (referred to as Fe/MgO).
- Co/MgO/Co (referred to as Co/MgO).
- FeCo/MgO/CoFe with Co/MgO interfaces (referred to as FeCo/MgO).

The electrodes have body-centered cubic symmetry with the (001) planes interfacing the (001) planes of the barriers. The [001] direction in the electrodes is parallel to the [110] direction in the barriers [1].

The Fe/MgO system has been extensively studied and numerical references discussing structural optimizations [1, 84, 86] are available in the literature. No optimizations exist for the Co/MgO and FeCo/MgO systems.

4.1 Set up of three tunnel junctions

The process of setting up each of the three systems requires four steps, namely

1. Define electrode geometry.
2. Define initial central region geometry.
3. Optimize central region geometry.
4. Sandwich central region between electrodes.

Each step is described in detail for the Fe/MgO system in the following sections. The setup of the remaining systems follows an analogous process, and only system-specific details are discussed.

4.1.1 Set up of Fe/MgO tunnel junction

The setup of the Fe/MgO system proceeds from where the analyses of bulk properties of relevant materials left off in the previous chapter. The calculated equilibrium lattice constant of Fe is used to set up an electrode cell, after which an initial central region geometry is constructed based on experimental data. The central region includes the MgO barrier and a number of electrode layers used for screening the electrodes from the barrier. The geometry is optimized, and the resulting central region is sandwiched between two instances of the electrode to form the two-probe system.

Defining electrode geometry

In Section 3.1.1 the equilibrium lattice constant of Fe was found to be 2.795 Å. Based on this result the electrode cell shown in Figure 3.5a was set up in Section 3.1.5. The electrode is shown again in Figure 4.1. The electrode includes six

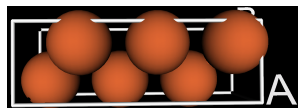


Figure 4.1: Electrode cell used for setting up the Fe/MgO system. The geometry of the electrode is set up based on the calculated equilibrium lattice constant of Fe.

Fe atoms, each located at the symmetry points of a body-centered cubic Bravais lattice, and the crystal is oriented with the (001) surfaces aligned parallel to the xy -plane.

When performing electrode calculations atoms in one electrode cell interact only with atoms in neighboring cells (due to model-specific details [64]). In order to allow interactions with atoms other than nearest neighbors several atoms must therefore be included in the electrode cell. The number of atoms to be used can be found by observing the range of the basis states of the atoms used in the geometry, but is most often chosen based on experience. We use six based on our experience, and consider this number conservative.

Defining initial central region geometry

The initial central region geometry is set up based on experimental data found using surface x-ray diffraction analysis [104]. It includes five atomic layers of MgO, and the Fe screening layers included in the central region are set up using the calculated equilibrium lattice constant. Seven screening layers are included on the left side of the barrier and six are included on the right¹. The unit cell of the central region is shown in Figure 4.2.

Optimizing central region geometry

The initial central region geometry is optimized as bulk using the Quasi-Newton algorithm [74, 105]. The Mg and O atoms in the barrier and the six Fe atoms

¹The screening layers are required by the software to “screen” the electrodes from the barrier. The difference in the number of screening layers is necessary to accommodate optimization of the system as bulk, since there is an odd number of barrier layers.

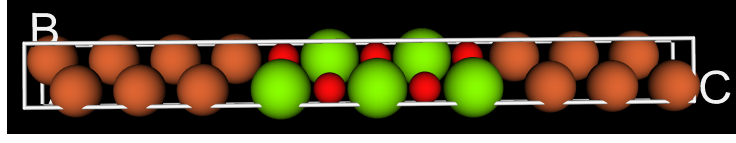


Figure 4.2: Central region used for setting up the Fe/MgO system. The geometry of the central region is optimized before use.

closest to this are allowed to relax in the direction perpendicular to the interfaces, while the remaining Fe atoms are fixed. The coordinates in the plane of the interfaces are maintained at the values determined by the calculated equilibrium lattice constant of Fe. Furthermore, the length of the central region cell in the perpendicular direction is “compressed” relative to the initial configuration in steps of 0.2231 \AA , which means that the distances to the layers that are not fixed are decreased from 1% to 8% in steps of 1%.

The energies for each of the optimization steps for each of the compressed cell lengths are shown in Figure 4.3. The energy goes down rapidly during the first

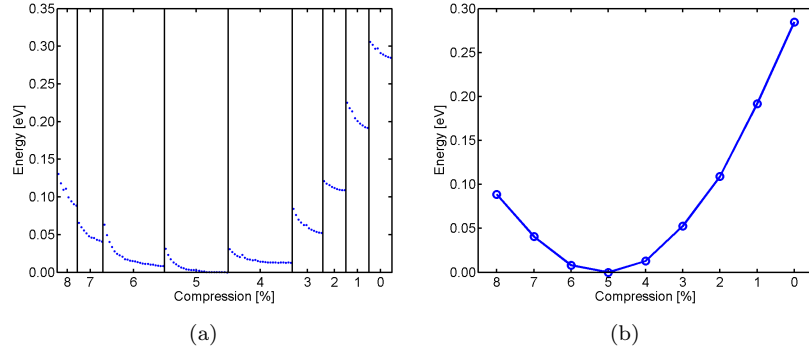


Figure 4.3: Energy after each optimization step for different cell lengths in the Fe/MgO system (a) along with the minimum energy obtained for each cell length (b).

steps, but converges after 10 to 15 steps². After this number of steps is reached it is apparent which cell lengths are “candidates” as the minimum-energy system, and the optimizations that are not stopped to save computational resources (hence the relatively small number of steps for the optimizations of cells that are not candidates). The optimizations with cell lengths decreased by 4%, 5%, and 6% are candidates for this system, and the 5% geometry turns out to have the smallest energy. The system is optimized until the forces perpendicular to the interfaces are all below 0.05 eV/\AA for the atoms that are allowed to move.

²The figure actually shows the second of two optimizations. To save computer resources and time the geometry is first optimized using fast (but poor) model parameters, after which the resulting geometries are optimized using good parameters.

Sandwiching central region between electrodes

The optimized central region geometry is sandwiched between two instances of the electrode cell. On the left side the left-most Fe atom in the central region is aligned one electrode cell length to the right of the left-most Fe atom in the electrode cell. On the right side the right-most atom in the electrode is aligned with the right-most atom in the central region by the same approach. All of this is taken care of automatically by the software. The resulting two-probe geometry is shown in Figure 4.4. The software used in this work uses periodic

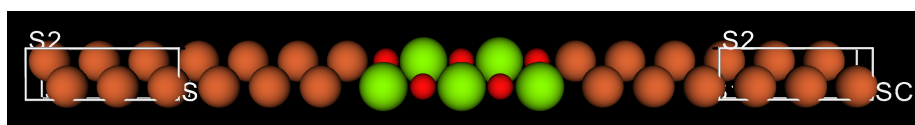


Figure 4.4: The Fe/MgO system geometry, consisting of the optimized central region sandwiched between two instances of the electrode cell.

boundary conditions in the plane of the interfaces, so the cell shown in Figure 4.4 is repeated indefinitely in this plane.

The reason the inner Fe atoms are allowed to move is to include the effects of surface reconstruction in the calculations. The choice of using three surface atoms (and four/three screening atoms) is based on experience. The numbers are chosen conservatively, which is supported by the observation that only the distance between the two Fe atoms closest to the barrier changes significantly while the rest of the distances remain at approximately the bulk values. An analysis of the structural properties of the optimized geometries is provided later in this chapter.

4.1.2 Set up of systems using Co and FeCo electrodes

Having set up the Fe/MgO system the Co/MgO and FeCo/MgO systems are easily set up. The approach is analogous to that described in the previous section:

1. The electrode geometries are defined. The Co electrode has body-centered cubic structure and the FeCo electrode has B2 structure. The equilibrium lattice constant found for Co (2.794 Å) is used for the Co electrode while that of Fe (2.795 Å) is used for the FeCo electrode.
2. The initial central region geometries are defined based on the optimized Fe/MgO geometry (this saves computer resources and time).
3. The central region geometries are optimized.
4. The central regions are sandwiched between the electrodes.

All systems are optimized until the forces perpendicular to the interfaces are below 0.05 eV/Å for the atoms that are allowed to move.

4.2 Structural properties of the three systems

The structural properties of the three optimized systems are discussed presently, and results are compared with data from the literature. For the Fe/MgO system References [1], [84], and [86] report on the results of structural optimizations, but for the systems employing Co and FeCo electrodes no reference data has been found. Zhang and Butler have investigated a Co/MgO system and an FeCo/MgO system numerically [66], but have done so without optimizing the geometries, and therefore offer no structural data with which to compare.

The central regions of the three systems are shown in Fig. 4.5. The figure

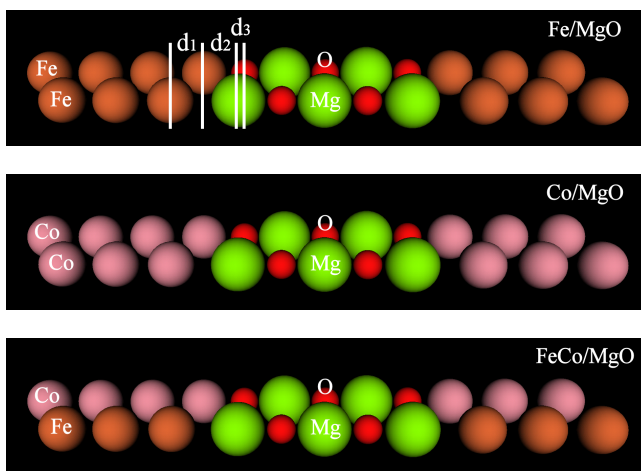


Figure 4.5: Central regions of the three magnetic tunnel junctions with identification of interface distances (top plot). Fe atoms are represented by brown spheres, Co atoms are purple, Mg atoms are green, and O atoms are red.

also identifies three inter-layer distances.

The structural properties resulting from the optimizations are summarized in Table 4.1. The distance between the Mg and O atoms in the outer-most layers

	d_1	d_2	d_3
Fe/MgO	-2%	2.17 Å	+0.07 Å
Co/MgO	-4%	2.16 Å	+0.09 Å
FeCo/MgO	-7%	2.16 Å	+0.08 Å

Table 4.1: Main structural parameters for the systems considered in this work (see text). d_1 is the distance between the two electrode layers closest to the barrier given in percentile variation with respect to the corresponding bulk distance of 2.795 Å (Fe and FeCo) or 2.794 Å (Co). d_2 is the distance between the closest electrode and oxygen layers. d_3 is the displacement of the outermost Mg atoms towards the electrodes, *cf.* Fig. 4.5.

in the barrier is approximately +0.08 Å for all three systems and the distance between the barrier O atoms and the closest screening atoms is approximately 2.17 Å. The distance between the screening layers closest to the barrier varies slightly for the three systems but remains close to the bulk values.

These structural properties are compared with results from the literature for the Fe/MgO system in Table 4.2. In agreement with results reported by

	d_1	d_2	d_3
This work (LSDA)	-2%	2.17 Å	0.07 Å
Butler <i>et al.</i> [1] (LSDA)	-2%	2.17 Å	0.05 Å
Waldron <i>et al.</i> [84] (LSDA)		2.24 Å	
Wortmann <i>et al.</i> [86] (GGA)	-6%	2.21 Å	0.06 Å

Table 4.2: Comparison of the structure of the Fe/MgO system with studies reported in References. [1, 84, 86]. The exchange-correlation potential used in each study is listed in parenthesis. The distances d_1 , d_2 , and d_3 are defined as in Table 4.1.

Butler *et al.* [1], Waldron *et al.* [84], and Wortmann *et al.* [86] we find an Fe-O distance of 2.17 Å. Also in agreement with the two former references we find a displacement (towards the interfaces) of the Mg atoms closest to the interfaces of 0.07 Å relative to the O atoms. The displacement of the Mg atoms in the second and fourth layers is much smaller (0.01 Å, away from the interfaces), and there is no displacement in the center layer. Consistent with the results reported by Butler *et al.* we find that the distance between the Fe layers closest to the interfaces is decreased by approximately 2% relative to that of the second- and third Fe layers from the barrier, which remain very close to the bulk value.

We have not been able to find any experimental reference data to compare with. Reference [104] provides all the relevant data, but reports on a system which includes a monolayer of FeO in the Fe/MgO interface. Such interface layers caused problems in initial studies, as they almost completely destroy the tunneling magnetoresistance [88]. We have reported on investigations of this effect in References [13] and [15].

The remaining systems have been studied much less extensively than the Fe/MgO system, and no reference data is available on system geometries. The distance between the surface electrode atom and the surface O atom is similar for all systems ($d_2 \approx 2.17$ Å), as is the splitting between the surface O and Mg atoms ($d_3 \approx 0.08$ Å). The distance between the electrode layers closest to the barrier (d_1) is slightly different for the systems but remain close to the bulk values.

4.3 Charge redistribution and surface magnetic moments of the systems

All three systems show the same charge redistribution trends in and near the barrier as the systems analyzed in the previous chapter (see Figure 3.10). For the Co/MgO and FeCo/MgO systems this is consistent with the results reported in Reference [66].

The magnetic moment on the Fe atoms closest to the barrier is $2.67 \mu_B$, which is somewhat smaller than the value found in the previous chapter, and almost 10% smaller than that of a free Fe surface ($2.96 \mu_B$ [102]). The value is, however, still much larger than the calculated bulk value of $2.06 \mu_B$, which is recovered in the screening layers not facing the barrier. The difference in

value between the systems discussed earlier and the systems discussed here are probably due to the much higher number of screening layers used in our system (7/6 layer *vs.* 4/4 layers). Using more screening layers provides more reliable results, and the electronic interaction between the Fe electrodes and the MgO barrier is probably not as weak as deduced based on the results discussed in Reference [1] and in the previous chapter. This conclusion is supported by the observation that the magnetic moment for the systems discussed earlier never reaches the calculated bulk value, but remains approximately 5% higher in the outer layers of the central region. Using four screening layers is, it seems, not sufficient to screen the electrodes.

The magnetic moment on the Co atoms closest to the barrier is $1.76 \mu_B$, which — as opposed to that of the Fe/MgO system — is close to the bulk value of $1.68 \mu_B$. This finding is consistent with the experimental results reported in Reference [106]³. The same is true for the systems using FeCo electrodes, in which the magnetic moment on the Co atoms closest to the barrier is $1.65 \mu_B$ (bulk value: $1.73 \mu_B$) and the magnetic moment on the Fe atoms closest to the barrier is $2.78 \mu_B$ (bulk value: $2.73 \mu_B$).

4.4 Summary

We have in this chapter described how we have set up and optimized the geometries of the three magnetic tunnel junctions to be analyzed in this thesis, and have investigated their structural, charge redistribution, and magnetic properties.

The optimization results for the Fe/MgO system are consistent with those obtained by Butler *et al.* [1]. For all three systems we find that the distance between the surface electrode atom and the surface O atom is approximately 2.17 \AA , and that the splitting between the surface O and Mg atoms is approximately 0.08 \AA . The distance between the electrode layers closest to the barrier is slightly different for the three systems but remains close to the bulk distances.

The three systems show the same charge redistribution trends in and near the barrier as the systems discussed in the previous chapter, while their surface magnetic moments differ. For the Fe/MgO system the magnetic moment on the atoms closest to the barrier is found to be in between that in bulk and that of a free Fe surface. For the systems using Co and FeCo electrodes the surface magnetic moments are close to the bulk values.

³The authors of Reference [106] are not sure whether the measured increase in magnetic moment in a monolayer of Co embedded between an Fe(001) surface and two monolayers of MgO is caused by the influence of the Fe or the MgO. Our results indicate that the main influence is from the Fe, and that the MgO only increases the moment slightly.

Chapter 5

Tunneling mechanisms in MgO-based tunnel junctions

As we have seen in Chapter 3 the zero-bias spin-transport properties of magnetic tunnel junctions with Magnesium oxide (MgO) barriers and Iron (Fe) electrodes are dominated by tunneling with $\mathbf{k}_{\parallel} \approx \mathbf{0}$ in the parallel magnetization configuration while the properties in the anti-parallel configuration are dominated by tunneling with $\mathbf{k}_{\parallel} \neq \mathbf{0}$. The conductance in the former configuration (G_P) is larger than in the latter (G_{AP}) and the tunneling magnetoresistance (TMR) is therefore large.

In this chapter we discuss the zero-bias spin-transport properties of the three magnetic tunnel junctions that were set up in the previous chapter. The systems are modeled by five-layer insulating MgO barriers sandwiched between ferromagnetic Fe, Cobalt (Co), or Iron-Cobalt (FeCo) electrodes. The MgO barriers have rock salt crystal structure and their (001) planes interface the (001) planes of the electrodes, which have body-centered cubic structure (Fe and Co) or B2 structure (FeCo). The [001] direction in the electrodes is parallel to the [110] direction in the barriers. The systems are shown in Figure 5.1. We focus on the qualitative understanding of the tunneling mechanisms in the systems, but also mention the quantitative results of conductance calculations and the resulting values of the TMR.

The Fe/MgO system has been extensively studied and numerical calculations of the zero-bias conductance are available in the literature [1, 2, 84, 85, 86, 87, 90]. Only a single numerical study exists for the Co/MgO and FeCo/MgO systems [66]. Following the elegant phenomenological description of tunneling with $\mathbf{k}_{\parallel} = \mathbf{0}$ in the initial work on Fe/MgO systems (Reference [1]) and Co/MgO and FeCo/systems (Reference [66]) there is a strong focus on $\mathbf{k}_{\parallel} = \mathbf{0}$ physics in the literature. Transport in the anti-parallel magnetization configuration of MgO-based magnetic tunnel junctions, however, occurs through tunneling with non-zero values of the in-plane k-vector [1, 2, 38, 84, 85, 90]. This tunneling mechanism gives rise to a small (but measurable) conductance, which limits the TMR. We therefore focus on describing tunneling with $\mathbf{k}_{\parallel} \neq \mathbf{0}$ in the anti-parallel configuration.

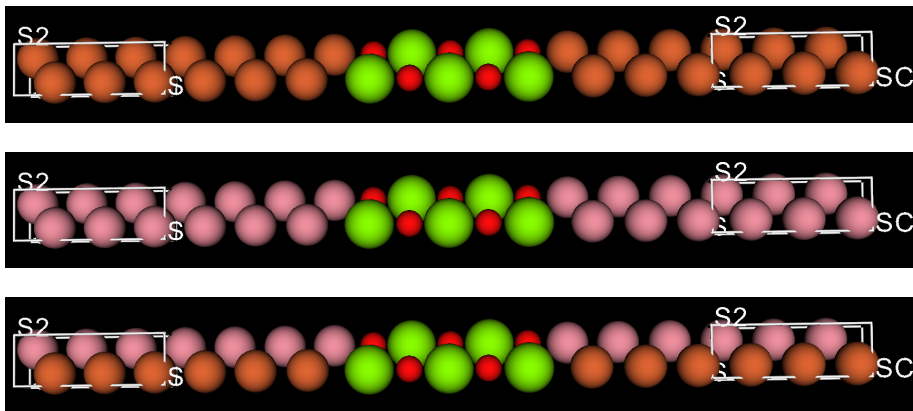


Figure 5.1: The three magnetic tunnel junctions studied in this work. Fe atoms are represented by brown spheres, Co atoms are purple, Mg atoms are green, and O atoms are red.

We continue to discuss the so-called “optimistic” TMR, which is defined $(I_P - I_{AP})/I_{AP}$, as opposed to the so-called “pessimistic” TMR, which is defined $(I_P - I_{AP})/(I_P + I_{AP})$, since most experimental and numerical studies report on this quantity. The calculated “optimistic” TMR is several thousand percent in numerical studies [1, 2, 84, 85, 86, 87, 90] and the “pessimistic” TMR seems a more appropriate measure of the difference in conductance. For historic reasons the “optimistic” TMR is measured, calculated, and discussed in the literature, and we use the conventional definition to ensure that our results can be used for comparison.

All three systems have similar zero-bias spin-transport properties. Tunneling in the parallel configuration occurs from Δ_1 states to Δ_1 states with maximum transmission probability at $\mathbf{k}_{\parallel} = \mathbf{0}$. Tunneling in the anti-parallel configuration occurs from states with Δ_1 features to states with Δ_5 , $\Delta_{2'}$, and Δ_2 features. The transmission probability is maximum along the lines where $|\mathbf{k}_x| = |\mathbf{k}_y|$ in the Fe/MgO and Co/MgO systems and along the lines where $\mathbf{k}_x = 0$ and $\mathbf{k}_y = 0$ in the FeCo/MgO system. The tunneling mechanism is significantly more efficient in the parallel configuration than in the anti-parallel configuration and the TMR is therefore large.

5.1 Conductance trends of the three tunnel junctions

The zero-bias conductance was calculated for each of the three magnetic tunnel junctions from Equation 2.45, and the results are listed in Table 5.1 along with the calculated and experimental values of the TMR. A 301×301 grid of k-points was used to sample the two-dimensional Brillouin zone. Figure 5.2 shows the conductance in the Fe/MgO system calculated using different k-point resolutions. The figure shows that the conductance in the parallel configuration is converged for a fairly small number of k-points while the anti-parallel configuration requires a slightly larger number. We estimate that using 301×301

	G_P	G_{AP}	TMR	TMR (exp.)
Fe/MgO	239	3.23	$\approx 7300\%$	247% [42]
Co/MgO	179	4.88	$\approx 3600\%$	507% [31]
FeCo/MgO	106	1.54	$\approx 6800\%$	300% [5]

Table 5.1: Zero-bias conductance with parallel (G_P) and anti-parallel (G_{AP}) magnetization of the electrodes along with calculated values of the TMR for the three magnetic tunnel junctions. The conductances are in units of $\text{mS}/\mu\text{m}^2$ and the TMR values are listed along with experimental results measured at low temperature. The experimental systems have approximately twice the number of layers as the systems discussed in this work.

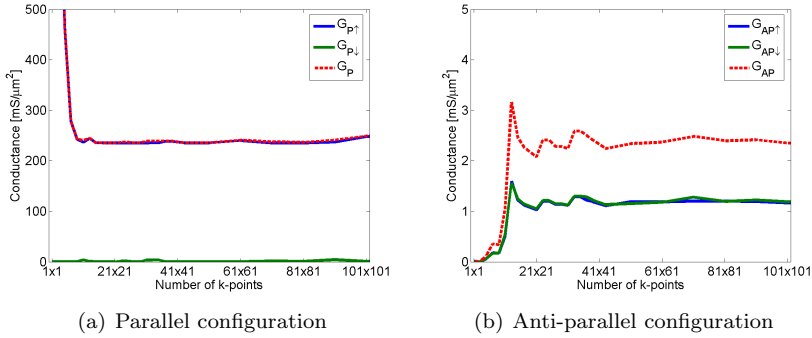


Figure 5.2: Calculated zero-bias conductance in the parallel- and anti-parallel configurations of the Fe/MgO system for different resolutions of the k-point sampling. The two-dimensional Brillouin zone is sampled using $N \times N$ k-points, where N is the number of k-points specified. Conductance values obtained sampling with up to 101×101 k-points are shown.

k-points results in a numerical accuracy of 2% in the calculated conductance.

Figure 5.2 shows that the conductance in the majority-spin channel ($G_{P\uparrow}$) in the parallel configuration of the Fe/MgO system is much larger than in the minority-spin channel ($G_{P\downarrow}$). The conductance in the two channels ($G_{AP\uparrow}$ and $G_{AP\downarrow}$) is identical in the anti-parallel configuration. These features are representative for all three systems. Table 5.1 shows that the conductance is much larger in the parallel magnetization configuration of the three systems than in the anti-parallel configuration, and that the TMR is therefore very large. We stress that the conductance in the anti-parallel configuration, while small, is of finite value and is routinely measured in experiments. The TMR values are of similar size for the three systems, which is consistent with the experimental data. Consistent with other studies [1, 2, 66, 84, 85] the numerical results are significantly larger than the experimental results, which is generally attributed to the presence of defects in the barrier and/or interfaces of experimental systems [85].

Table 5.1 also shows that the measured TMR is higher for the Co/MgO and FeCo/MgO systems reported in References [5, 31] than for the Fe/MgO system reported in Reference [42] while we find the largest magnetoresistance for the Fe/MgO system. We attribute the higher values in the (experimental) Co/MgO and FeCo/MgO systems to a higher epitaxial quality of the junctions. This is supported by investigations of the conductance of an FeCo/MgO system with Fe/MgO interfaces. The calculated conductance for such a system, which — apart from the difference in electrode/barrier interface layers — is identical to the system discussed in this work, is significantly larger for Fe/MgO interfaces than for Co/MgO interfaces. We attribute the differences in conductance to differences in the electrode/barrier coupling, and conclude that the Fe/MgO interface offers stronger coupling than the Co/MgO interface.

The above observations are summarized as follows:

- $G_P \gg G_{AP}$
- $G_{P\uparrow} \gg G_{P\downarrow}$
- $G_{AP\uparrow} = G_{AP\downarrow}$

5.2 Tunneling mechanisms in the parallel configuration

Figure 5.3 shows the \mathbf{k}_{\parallel} -resolved transmission spectra for the majority-spin channel in the parallel magnetization configuration of the magnetic tunnel junctions. The spectra were calculated at the Fermi energy and show similar trends for the three systems: the transmission spectra are dominated by broad peaks in the center of the two-dimensional Brillouin zone ($\mathbf{k}_{\parallel} = \mathbf{0}$). A number of spikes are present in the spectra near the corners of the Brillouin zone (especially in the Fe/MgO system). They are attributed to tunneling through interface resonances, as discussed in Chapter 3, and are present in most spectra discussed in this work. They are very sharp and do not contribute significantly to the conductance in either of the magnetization configurations ($< 5\%$). They contribute to the conductance in the minority-spin channel in the parallel configuration (not shown in Figure 5.3), but — as shown in Figure 5.2 — the conductance in

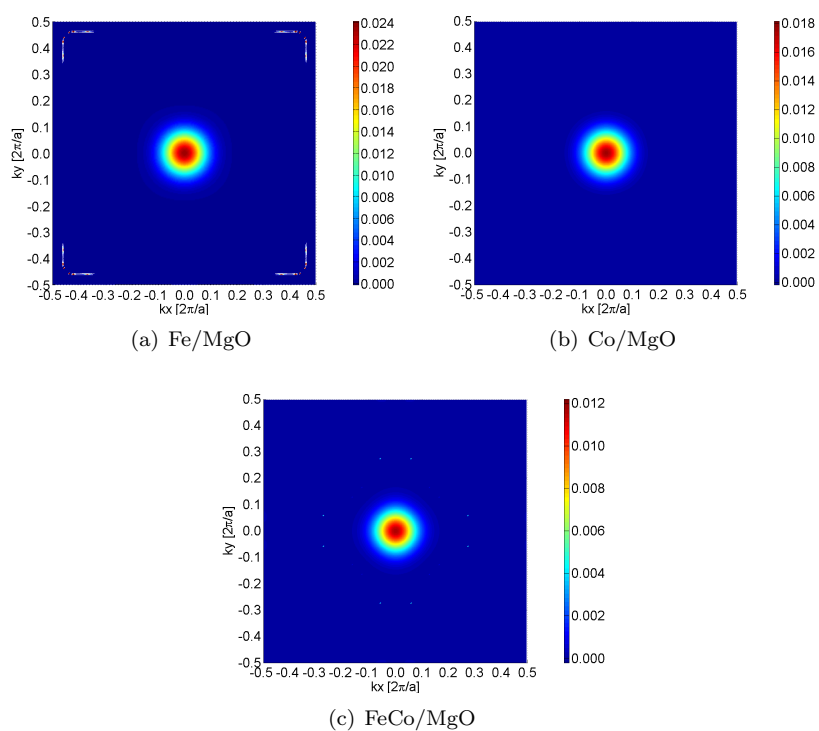


Figure 5.3: Transmission spectra for the majority-spin channel in the parallel magnetization configuration of the magnetic tunnel junctions. A peak is located in the center of the two-dimensional Brillouin zone. (a is the width of the central cell in the plane parallel to the interfaces).

this channel is insignificant compared to the conductance in the majority-spin channel.

The spin-dependent band structures of the three electrode materials are shown again in Figure 5.4. The symmetries of the Bloch states are visualized

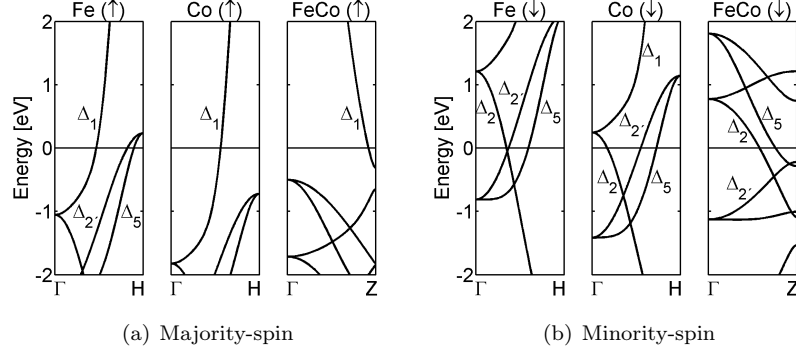


Figure 5.4: Majority- and minority-spin band structures of the Fe, Co, and FeCo electrodes in the [001] direction for $\mathbf{k}_{\parallel} = \mathbf{0}$. The energies are relative to the Fermi energy. (Identical to Figure 3.6).

in Figure 5.5. The band structures show that the electrode states listed in

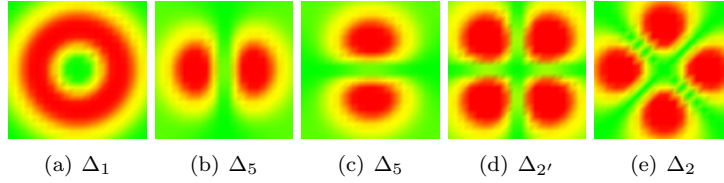


Figure 5.5: Symmetries of the Bloch states with $E = E_F$ and $\mathbf{k}_{\parallel} = \mathbf{0}$. The states are visualized on the plane parallel to the interfaces through an electrode atom. Red color indicates a high absolutely value of the wave function, yellow indicates a medium value, and green indicates zero value.

Table 5.2 are available for zero-bias spin-transport with $E = E_F$ and $\mathbf{k}_{\parallel} = \mathbf{0}$. The table shows, in agreement with References [1] and [66], that Δ_1 bands cross

	Fe		Co		FeCo	
	majority	minority	majority	minority	majority	minority
Δ_1	✓		✓		✓	
Δ_5	✓	✓		✓		✓
$\Delta_{2'}$	✓	✓		✓		✓
Δ_2		✓		✓		

Table 5.2: Bloch states propagating in the [001] direction with $\mathbf{k}_{\parallel} = \mathbf{0}$ at the Fermi energy in the Fe, Co, and FeCo electrodes. The Δ_5 states are doubly degenerate. A Δ_1 state is available for majority-spin electrons in all three electrodes.

the Fermi level for majority-spin electrons in all three electrodes.

Resolving the transmission coefficient for $\mathbf{k}_{\parallel} = 0$ into transmission eigenstates, according to Equation 2.47, the conductance is found to be dominated by tunneling from Δ_1 states to Δ_1 states for all three systems. Table 5.3 lists the transmission eigenvalues of the transmission eigenstates contributing most to the zero-bias conductance in the parallel magnetization configuration. The

System	$\mathbf{k}_{\parallel} [2\pi/a]$	τ	Left	Right
Fe/MgO	(0.0000, 0.0000)	$2 \cdot 10^{-2}$	Δ_1	Δ_1
Co/MgO	(0.0000, 0.0000)	$2 \cdot 10^{-2}$	Δ_1	Δ_1
FeCo/MgO	(0.0000, 0.0000)	$1 \cdot 10^{-2}$	Δ_1	Δ_1

Table 5.3: Values of \mathbf{k}_{\parallel} at which the transmissions are maximum in the parallel magnetization configuration of the three systems. Also listed are the largest transmission eigenvalues, τ , and the symmetries of the corresponding transmission eigenstates in the two electrodes. Tunneling occurs primarily from Δ_1 states to Δ_1 states.

electrode Bloch states are damped when propagating through the MgO barrier, and the rate of decay depends on the symmetries of the states: nodes in the plane parallel to the interfaces results in increased damping [101]. Since the Δ_1 state has no nodes in this plane it propagates with less damping than the other states.

The tunneling of the Δ_1 state through the 12-layer Fe/MgO system discussed in Chapter 3 is visualized in Figure 5.6¹. The figure shows how the

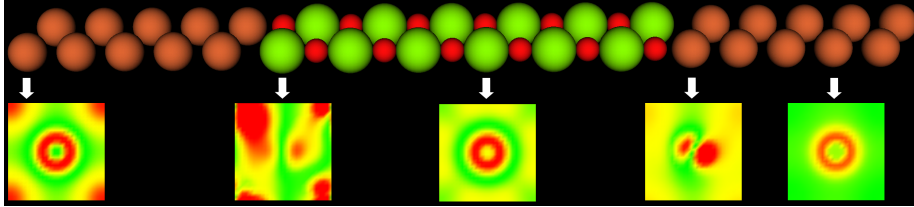


Figure 5.6: Dominating transmission eigenchannel for an Fe/MgO magnetic tunnel junction with 12 barrier layers in the parallel configuration. The system is identical to that discussed in Reference [1].

state enters the system with Δ_1 symmetry (first cut-plane from left), scatters on the electrode/barrier interface (second cut-plane), recovers the symmetry in the middle of the barrier (third cut-plane), scatters on the barrier/electrode interface (fourth cut-plane), and recovers the symmetry in the right electrode (last cut-plane). For $\mathbf{k}_{\parallel} = 0$ states of different symmetry do not couple, and the Δ_1 state inbound from the left electrode couples only to the Δ_1 state in the right electrode (for $\mathbf{k}_{\parallel} \neq 0$ there is no such “symmetry conservation” [101]).

¹Tunneling is visualized for the system with 12 barrier layers as the barriers in the systems with fewer layers are not thick enough for the transmission eigenstate to fully recover its symmetry inside the barriers.

5.3 Tunneling mechanisms in the anti-parallel configuration

Figure 5.7 shows the \mathbf{k}_{\parallel} -resolved transmission spectra for one of the two spin-channels in the anti-parallel configuration (the spectra are identical for the two channels). The spectra were calculated at the Fermi energy and show simi-

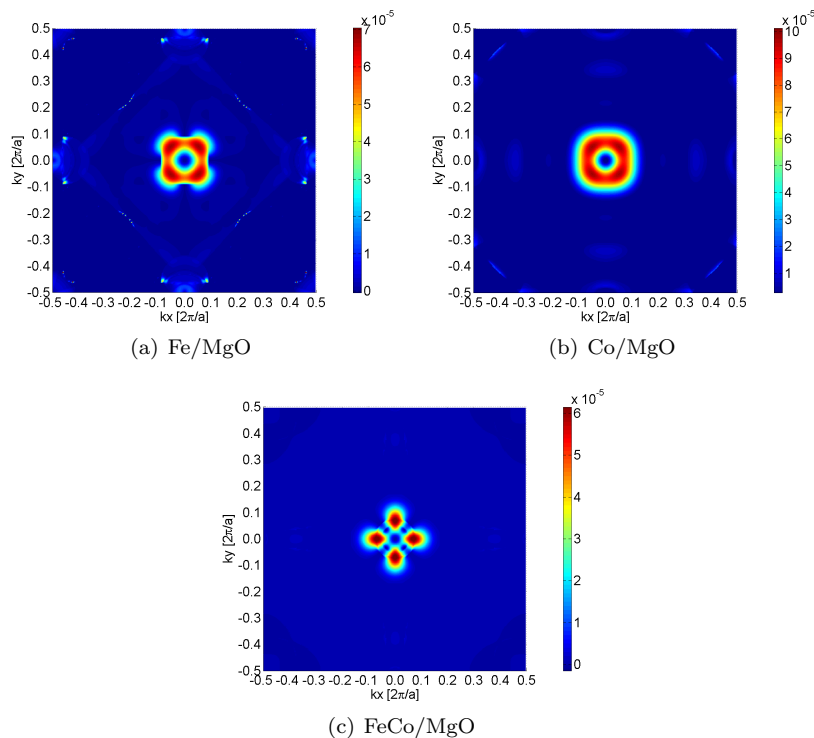


Figure 5.7: Transmission spectra for a single spin-channel in the anti-parallel magnetization configuration of the magnetic tunnel junctions. Four peaks are located away from the center of the two-dimensional Brillouin zone. (a is the width of the central cell in the plane parallel to the interfaces).

lar trends for the three systems: the transmission is dominated by four peaks located away from $\mathbf{k}_{\parallel} = \mathbf{0}$. The peaks are centered along the lines where $|\mathbf{k}_x| = |\mathbf{k}_y|$ in the Fe/MgO and Co/MgO systems and along the lines where $\mathbf{k}_x = 0$ and $\mathbf{k}_y = 0$ in the FeCo/MgO system.

In the anti-parallel configuration the transport mechanism is more complex than in the parallel configuration. Tunneling occurs from majority-spin to minority-spin bands when the electrodes are magnetized in opposite directions. Since there are no minority-spin Δ_1 bands available at the Fermi energy tunneling from Δ_1 states to Δ_1 states is not possible. Tunneling of states other than Δ_1 is inefficient at $\mathbf{k}_{\parallel} = \mathbf{0}$ so the transmission in the center of the two-dimensional Brillouin zone is close to zero in the Fe/MgO system, in which both majority- and minority-spin Δ_5 and Δ_2 states are available, and identically zero in the Co/MgO and FeCo/MgO systems, in which the majority- and

minority-spin states all have different symmetries (*cf.* Table 5.2).

The transmission probability for a given spin at given values of E and \mathbf{k}_{\parallel} depends on three parameters: 1) the coupling of the majority-spin Δ_1 state to slowly decaying barrier wave functions at the electrode/barrier interface, 2) the decay of these wave functions when propagating through the barrier, and 3) the coupling of the wave functions to the minority-spin electrode states at the barrier/electrode interface. For $\mathbf{k}_{\parallel} \neq \mathbf{0}$ the symmetries of the states are different from the ones visualized in Figure 5.5. The states that have Δ_1 symmetry at $\mathbf{k}_{\parallel} = \mathbf{0}$ largely maintain their symmetry for $\mathbf{k}_{\parallel} \neq \mathbf{0}$ and the bands with this symmetry appear similar for $\mathbf{k}_{\parallel} = \mathbf{0}$ and $\mathbf{k}_{\parallel} \neq \mathbf{0}$. The Δ_5 , $\Delta_{2'}$, and Δ_2 states change more and the bands appear different. The Δ_5 , $\Delta_{2'}$, and Δ_2 features can, however, be recognized in states with $\mathbf{k}_{\parallel} \neq \mathbf{0}$. Figure 5.8 shows the spin-dependent band structures for the FeCo electrode at the k -vector where the transmission is maximum in the FeCo/MgO system. The figure shows that the

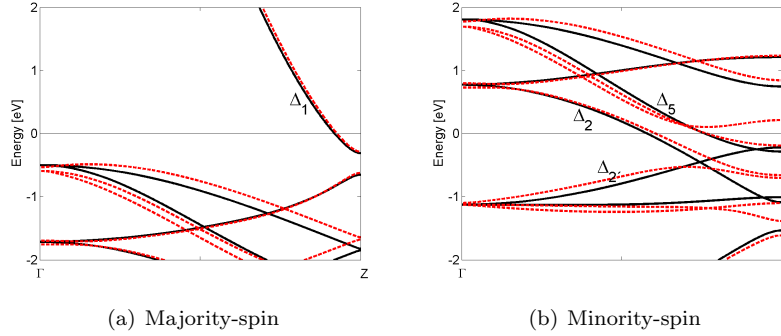


Figure 5.8: Majority-spin and minority-spin band structures of the FeCo electrode for $\mathbf{k}_{\parallel} = \mathbf{0}$ (black lines) and $\mathbf{k}_{\parallel} = (0.0681, 0.0000)$ (red lines).

Δ_1 band appears largely unchanged while the Δ_5 , $\Delta_{2'}$, and Δ_2 bands change significantly.

The transmission eigenvalues for the transmission eigenstates contributing most to the zero-bias conductance are listed in Table 5.4. The eigenstates are

System	$\mathbf{k}_{\parallel} [2\pi/a]$	τ	Left	Right
Fe/MgO	(0.0515, 0.0515)	$7 \cdot 10^{-5}$	Δ_1	$\Delta_5, \Delta_{2'}, \Delta_2$
Co/MgO	(0.0515, 0.0515)	$1 \cdot 10^{-4}$	Δ_1	$\Delta_5, \Delta_{2'}, \Delta_2$
FeCo/MgO	(0.0681, 0.0000)	$6 \cdot 10^{-5}$	Δ_1	$\Delta_5, \Delta_{2'}, \Delta_2$

Table 5.4: Values of \mathbf{k}_{\parallel} at which the transmission coefficients are maximum in the anti-parallel magnetization configuration of the three systems. Also listed are the largest transmission eigenvalues, τ , and the symmetries of the corresponding transmission eigenstates in the two electrodes. Tunneling occurs primarily from states with Δ_1 features to states with Δ_5 , $\Delta_{2'}$, and Δ_2 features.

calculated at the k -vectors where the transmission coefficients are maximum in the anti-parallel configuration of the three systems. The table shows that tunneling occurs from majority-spin states with Δ_1 features to minority-spin states

with features similar to Δ_5 , $\Delta_{2'}$, and Δ_2 states. Fig. 5.9 shows the symmetries of the transmission eigenstates with the highest tunneling probabilities for anti-parallel magnetization of the electrodes. The transmission eigenstates show

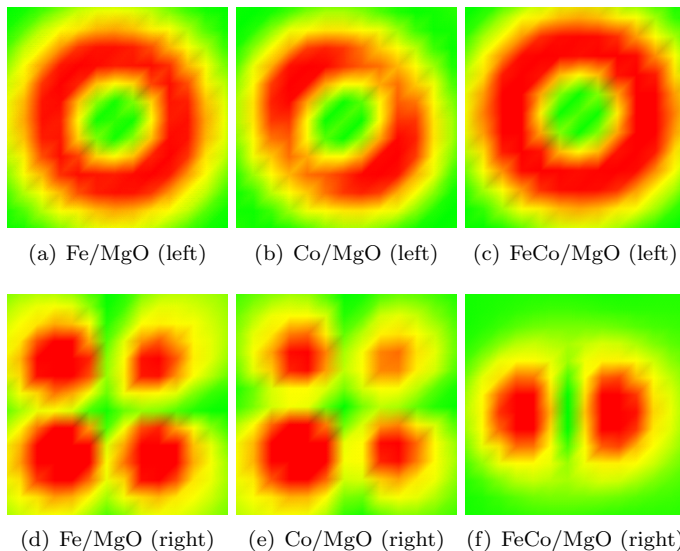


Figure 5.9: Symmetries of the transmission eigenstates with the highest tunneling probabilities in the anti-parallel magnetization configuration of the three systems. The transmission eigenstates are calculated at the values of \mathbf{k}_{\parallel} where the transmission coefficients are maximum. Δ_1 features are apparent in the left electrodes and Δ_5 and $\Delta_{2'}$ features are apparent in the right.

clear signs of Δ_1 symmetry in the left electrode and Δ_5 and $\Delta_{2'}$ symmetries in the right electrode. While the states with Δ_1 features can couple to states with Δ_5 , $\Delta_{2'}$, and Δ_2 features when $\mathbf{k}_{\parallel} \neq \mathbf{0}$ the coupling is inefficient, and the transmission probability is therefore significantly smaller than for tunneling from Δ_1 states to Δ_1 states. The conductance is therefore smaller in the anti-parallel configuration than in the parallel configuration.

We wish to emphasize the importance of tunneling with $\mathbf{k}_{\parallel} \neq \mathbf{0}$ when the electrodes are magnetized in opposite directions. It has been argued that the zero-bias TMR in Co/MgO systems is higher than in Fe/MgO systems since there are no minority-spin Δ_1 bands at the Fermi energy in the Co electrode while there is *only* a Δ_1 band for majority-spin electrons [66] since this leads to total reflection of incoming Bloch states with $\mathbf{k}_{\parallel} = \mathbf{0}$ (in the Fe electrodes both majority- and minority-spin Δ_5 and Δ_2 states are available). Most arguments found in the literature are based on such $\mathbf{k}_{\parallel} = \mathbf{0}$ physics phenomena. Raza and Raza [107] have, for example, implemented a single-band tight-binding model which includes terms representing the Δ_1 and Δ_5 bands and assumes constant transmission across the two-dimensional Brillouin zone. Using this model they have reproduced the results of first-principles calculations and measurements.

The results reported in this thesis are not consistent with such $\mathbf{k}_{\parallel} = \mathbf{0}$ arguments. Transport in the parallel configuration is well described by the $\mathbf{k}_{\parallel} = \mathbf{0}$ phenomenology developed by Butler *et al.* [1]. As we have shown, however,

and in agreement with the results reported in References [1, 2, 38, 84, 85, 90], spin-transport in the anti-parallel magnetization configuration of MgO-based magnetic tunnel junctions occurs through tunneling with non-zero values of the in-plane \mathbf{k} -vector. In this configuration $\mathbf{k}_{\parallel} = \mathbf{0}$ physics cannot explain observed phenomena. We note that the model of Raza and Raza cannot reproduce the characteristics measured (and calculated) for Co/MgO systems at low voltages (as discussed in the following chapter).

5.4 Summary

We have in this chapter analyzed the tunneling mechanisms in the three magnetic tunnel junctions which were set up and optimized in the previous chapter (Fe/MgO, Co/MgO, and FeCo/MgO).

For parallel alignment of the electrode magnetizations the zero-bias conductance is dominated by tunneling from Δ_1 states to Δ_1 states with maximum transmission probability for $\mathbf{k}_{\parallel} = \mathbf{0}$. For anti-parallel alignment the conductance is dominated by tunneling from states with Δ_1 features to states with features similar to Δ_5 , $\Delta_{2'}$, and Δ_2 states and the transmission maximum is found for $\mathbf{k}_{\parallel} \neq \mathbf{0}$.

The conductance is significantly larger in the parallel configuration than in the anti-parallel configuration, so the TMR is large. It is of similar size for all three systems.

Chapter 6

Influence of a bias voltage in MgO-based tunnel junctions

We have seen in the previous chapter that tunneling in the parallel magnetization configuration of Fe/MgO, Co/MgO, and FeCo/MgO magnetic tunnel junctions occurs from Δ_1 states to Δ_1 states with maximum transmission probability for $\mathbf{k}_{\parallel} = \mathbf{0}$. Tunneling in the anti-parallel configuration occurs from states with Δ_1 features to states with Δ_5 , $\Delta_{2'}$, and Δ_2 features with maximum transmission probability for $\mathbf{k}_{\parallel} \neq \mathbf{0}$.

In this chapter we examine the influence of a finite bias voltage on these tunneling mechanisms, investigate the current/voltage characteristics of the three systems, and discuss the voltage dependence of the tunneling magnetoresistance. Voltages in the range 0 – 0.5 V are studied. We do this using the density functional theory, non-equilibrium Green's functions approach described in Section 2.6, and make use of a non-self-consistent ramp approximation due to Zhang *et al.* [89].

We note that the finite-bias spin-transport properties of Fe/MgO systems have been modeled by several groups [84, 85, 86, 87, 90] but that no numerical studies exist for the Co/MgO and FeCo/MgO systems.

The current in the parallel magnetization configuration of the three systems increases linearly with the bias voltage. In the FeCo/MgO system the differential conductance decreases above $V \approx 0.3$ V when the bottom of the Δ_1 band enters the energy integration window contributing to the current. The current in the anti-parallel configuration increases super-linearly in the Fe/MgO and Co/MgO systems and linearly in the FeCo/MgO system. These characteristics give rise to decreasing values of the tunneling magnetoresistance in the Fe/MgO and Co/MgO systems. In the FeCo/MgO system the TMR remains constant below $V \approx 0.3$ V above which it decreases.

The tunneling mechanisms resulting in these current/voltage characteristics and TMR trends are primarily governed by the electronic structure of the electrodes. The main features in the current/voltage characteristics are not related to the voltage drop, but arise from the energy dependence of the transmission coefficient.

6.1 Current/voltage characteristics of the three tunnel junctions

The current/voltage characteristics of the three magnetic tunnel junctions were calculated from Equation 2.44, and the results are shown in Figure 6.1. The

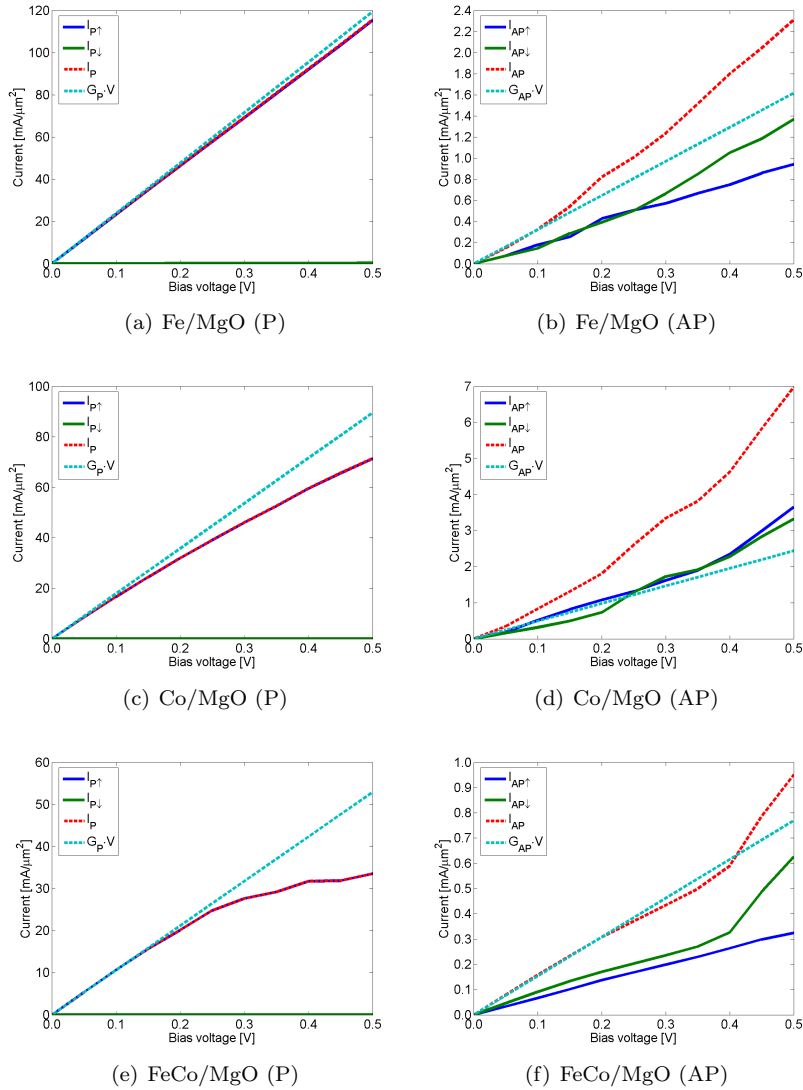


Figure 6.1: Current/voltage characteristics of the three magnetic tunnel junctions showing the current in the two spin-channels of the parallel- and anti-parallel configurations as well as the total current and the current calculated from the zero-bias conductance.

current was calculated with an electron temperature parameter of 1 mK by sampling the two-dimensional Brillouin zone using a 21×21 grid of k-points.

We estimate that using this k-point sampling results in a numerical accuracy of 2% for the current in the parallel configuration and 8% in the anti-parallel configuration. We calculated the current for a small number of bias voltages using 51×51 k-points and found that the results were similar to those found using 21×21 k-points.

The transmission spikes due to tunneling through interface resonance states, discussed in Chapter 3, remain in the transmission spectra calculated for $V > 0$ V. This is contrary to the results reported in Reference [84], in which the spikes are found to disappear at a small bias voltage. The influence of the spikes on the calculated current, however, remains small ($< 5\%$).

To save computational resources and time we performed the current calculations using a non-self-consistent ramp approximation used for magnetic tunnel junctions by Zhang *et al.* in Reference [89] and by Heiliger *et al.* for their investigations in Reference [87]. Within this approximation the total out-of-equilibrium Kohn-Sham potential is written as an equilibrium part and an induced-potential part, $\delta V(V)$,

$$V^{eff}(V) = V^{eff}(V=0) + \delta V(V) \quad (6.1)$$

The induced part is $-eV/2$ in the left electrode, $eV/2$ in the right electrode, and falls off linearly in the barrier. Zhang *et al.* compared the results obtained using the ramp approximation with results obtained using a fully self-consistent calculation of the tunneling current in an Fe/MgO system with an FeO interface layer. For the parallel configuration they found a good agreement between the two approaches in the low bias regime, $V < 0.1$ V. For larger voltages the approximation deviates significantly, reaching about twice the self-consistent results at $V = 0.5$ V. In the anti-parallel configuration the results agreed for most of the voltage range. We have conducted a small comparison study and found similar results. The approximation includes the rigid shift of the asymptotic electrode band structures necessary to correctly describe scattering in a biased low-transmission junction. We use the approximation and note that we therefore expect our results for voltages higher than 0.1 V to overestimate the current in the parallel configuration and thereby also the TMR compared to results found using a fully self-consistent method.

The current in the parallel magnetization configuration (I_P) is dominated by the majority-spin channel ($I_{P\uparrow}$), in which the current increases linearly with the bias voltage. This is consistent with the experimental results reported for Fe/MgO systems in Reference [108] and the numerical results in References [84, 85, 87]. In the FeCo/MgO system the differential conductance becomes small above $V \approx 0.3$ V. In the anti-parallel magnetization configuration the currents in the two spin-channels ($I_{AP\uparrow}$ and $I_{AP\downarrow}$) contribute equally at $V = 0$ V but differently at finite bias. The total current (I_{AP}) increases super-linearly with the voltage in the Fe/MgO and Co/MgO systems, *i.e.* with increasing differential conductance, and linearly in the FeCo/MgO system. For the Fe/MgO system this is consistent with the numerical results reported in Reference [84]. The current in the parallel configuration is much larger than in the anti-parallel configuration throughout the voltage range, and the current/voltage characteristics reproduce the linear response values in the limit where $V \rightarrow 0$ V. We again stress that the current in the anti-parallel configuration is small but measurable. The above observations are summarized as follows:

- $I_P \gg I_{AP}$
- I_P increases linearly (Fe/MgO, Co/MgO)
- I_P increases sub-linearly (FeCo/MgO)
- I_{AP} increases super-linearly (Fe/MgO, Co/MgO)
- I_{AP} increases linearly (FeCo/MgO)

The observations are made for the voltage range 0 – 0.5 V.

For each system the tunneling magnetoresistance, resulting from the current/voltage characteristics, is shown in Figure 6.2. Also shown are the ex-

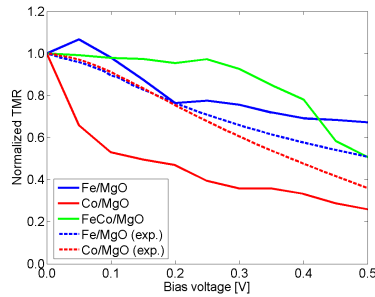


Figure 6.2: Voltage dependence of the TMR in the three magnetic tunnel junctions, normalized by the values found at $V = 0$ V. The experimental results reported in Reference [31] are shown with dashed lines.

perimental results from Reference [31]. In the Fe/MgO and Co/MgO systems the TMR decreases with increasing bias voltage throughout the voltage range 0 – 0.5 V, while the TMR remains constant in the FeCo/MgO system below $V \approx 0.3$ V (above which it decreases).

The decrease in TMR is in agreement with other numerical and experimental results. At a voltage of $V = 0.5$ V the TMR in the Fe/MgO system decreases to a value of 0.7 times the zero-bias value. This agrees with experimental measurements which find values between 0.5 and 0.8 [42, 31, 109]. Numerically, a decrease to approximately 0.3 has been reported [84]. For the Co/MgO system the TMR decreases to 0.3 times its zero-bias value at $V = 0.5$ V, in agreement with an experimental value of approximately 0.4 [31]. As mentioned above, the TMR remains constant for voltages below $V \approx 0.3$ V in the FeCo/MgO system. Above this voltage the TMR falls off and reaches approximately 0.5 times the zero-bias value at $V = 0.5$ V. This is in agreement with experimental results which find a decrease to approximately 0.5 [5].

We note that the tunneling magnetoresistance of the Fe/MgO and Co/MgO systems, reported in Reference [31] and shown in Figure 6.2, decrease at a similar rate for small voltages while our results decrease at different rates. The experimental results show significant asymmetry for positive and negative bias voltages, due to differences in the top- and bottom electrodes, and the rate of decrease at small voltages differs more in the bias direction not shown.

6.2 Influence of a bias voltage in the parallel configuration

The free-electron-like transport mechanism for majority-spin Δ_1 states in the parallel configuration of the systems gives rise to the linear current/voltage characteristics observed in the three systems. Figure 6.3 shows transmission spectra for the parallel magnetization configuration, calculated along the line where $\mathbf{k}_x = \mathbf{k}_y$. Figure 6.3a shows the majority-spin transmission spectra in the Fe/MgO system for different bias voltages. The spectrum for a given voltage represents the average of a series of spectra calculated for different energies in the energy integration window contributing to the current (see discussion in relation to Equation 2.43). The energies range from $-eV/2$ to $eV/2$ in steps of 0.05 eV. The height of the peaks in the averaged spectra remains constant with the voltage. Figure 6.3b shows that the height of the Δ_1 peak, calculated at $\mathbf{k}_{\parallel} = \mathbf{0}$, remains almost constant as a function of the energy in the integration window. The transmission probability is, in other words, almost independent of the bias voltage and the energy. In the Co/MgO system (Figures 6.3c and d) the height of the peak decreases slightly with the bias voltage (it increases slightly with the energy) giving rise to a slight sub-linearity in the current increase. The same is true in the FeCo/MgO system (Figures 6.3e and f), in which the height goes to zero for small energies when $V > 0.3$ V when the bottom of the Δ_1 band enters the integration window. The results for the FeCo/MgO are discussed presently.

Fall off in differential conductance in the FeCo/MgO system

Figure 6.4 shows the Δ_1 bands in the two FeCo electrodes for different voltages. The figure shows how the Δ_1 band is raised in one electrode and lowered in the other by the bias voltage. The bottom of the Δ_1 band is located 0.32 eV below the Fermi energy and enters the energy integration window contributing to the current when $V \approx 0.32$ V. Above this “turn-off” voltage, V_c , the raised Δ_1 band occupies V_c/V of the energy integration window and the contribution from the band becomes increasingly smaller.

To confirm that the drop-off in transmission in Figure 6.3f is caused by the disappearance of the Δ_1 band we plot the \mathbf{k}_{\parallel} -resolved transmission spectrum near the drop-off energy for $V = 0.5$ V in Figure 6.5. The figure shows that both the height and the width of the Δ_1 peak decreases when the energy goes from -0.05 eV to -0.07 eV, and we note that the peak is completely gone for $E = -0.08$ eV (not shown).

6.3 Influence of a bias voltage in the anti-parallel configuration

Figure 6.6 shows the averaged transmission spectra for a single spin-channel in the Fe/MgO system in the anti-parallel magnetization configuration, calculated along the line where $\mathbf{k}_x = \mathbf{k}_y$, and the transmission spectra at different energies for $V = 0.5$ V. The figure shows that the height of the averaged transmission peak increases with the voltage, and that the height is different for different

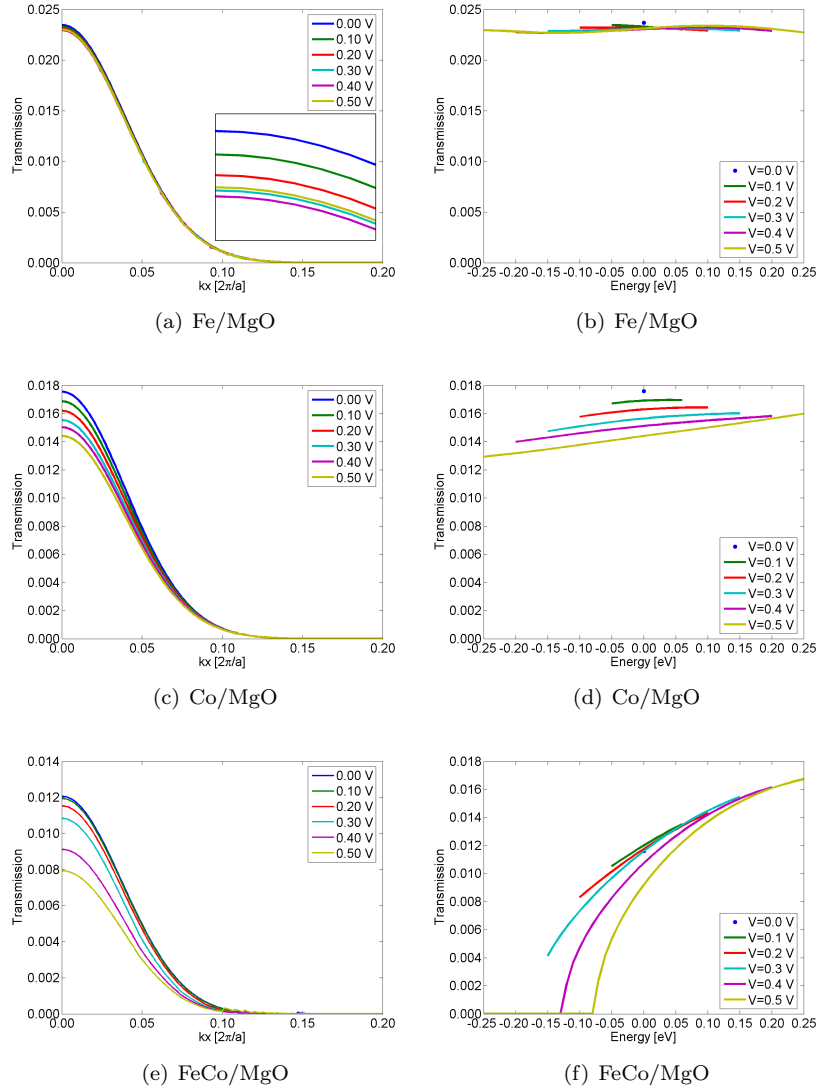


Figure 6.3: Left: k_{\parallel} -resolved averaged transmission spectra for the majority-spin channel in the parallel magnetization configuration of the systems, calculated along the line where $k_x = k_y$ for different voltages. Right: E -resolved transmission spectra calculated for $k_{\parallel} = \mathbf{0}$. The height of the Δ_1 peak remains almost constant with the voltage in all three systems, but decreases above $V \approx 0.3$ V in the FeCo/MgO system.

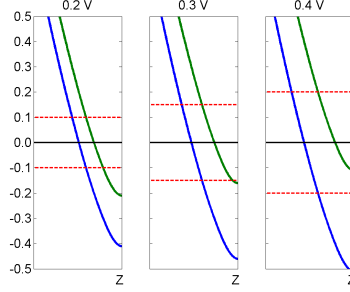


Figure 6.4: Spin-dependent band structure of majority-spin electrons with $\mathbf{k}_{\parallel} = 0$ in the FeCo electrode under the influence of a finite bias voltage, V . Only the $1/5$ of the Brillouin zone closest to the Z-point is shown. The Δ_1 band in one electrode is raised by $eV/2$, while the corresponding band in the other electrode is lowered by the same amount. The current is calculated over the energy window from $-eV/2$ to $eV/2$ (e is the elementary charge). The Δ_1 band ends 0.32 eV below the Fermi energy, which becomes visible in the current/voltage characteristics above 0.32 V.

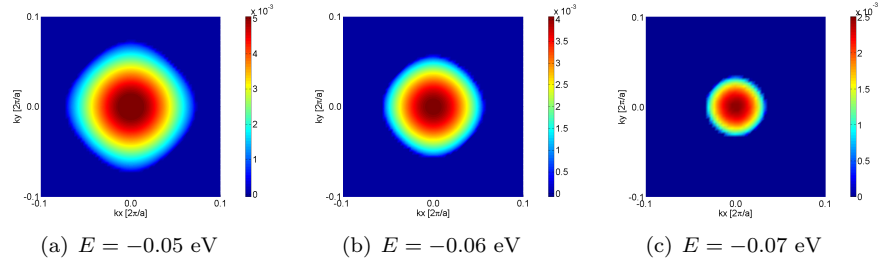


Figure 6.5: Transmission spectrum for the majority-spin channel in the parallel magnetization configuration of the FeCo/MgO magnetic tunnel junction with Fe/MgO interfaces at $V = 0.5$ V for energies near the drop-off energy. The height and width of the Δ_1 peak decrease when the energy decreases and the peak disappears for $E \approx -0.08$ eV.

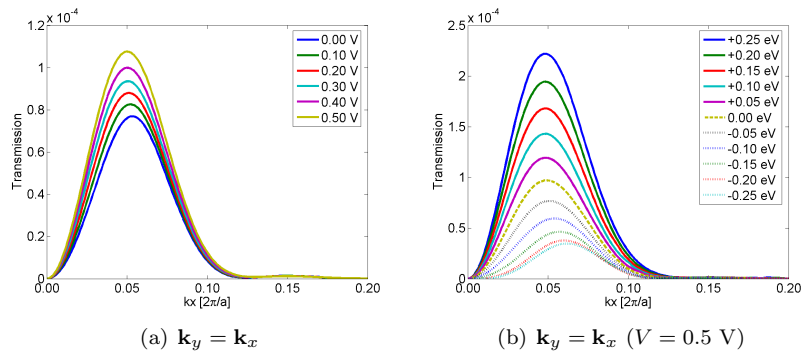


Figure 6.6: Transmission spectra for a single spin-channel in the anti-parallel magnetization configuration of the Fe/MgO system calculated along the line where $\mathbf{k}_x = \mathbf{k}_y$.

energies at a given voltage¹. Generally the heights and positions of the transmission peaks in the anti-parallel configuration of the three systems vary with the voltage and the energy. The tunneling mechanisms are complex and no simple model exists. In the Fe/MgO system, for example, the transmission peaks change position from being located along the lines where $|\mathbf{k}_x| = |\mathbf{k}_y|$ for $V < 0.3$ V to being located along the lines where $\mathbf{k}_x = 0$ and $\mathbf{k}_y = 0$ when $V > 0.3$ V. Figure 6.7 compares the averaged transmission along the line where $\mathbf{k}_x = \mathbf{k}_y$ (Figure 6.6a) with the averaged transmission along the line where $\mathbf{k}_y = 0$. The transmission increases with the voltage in both directions, but

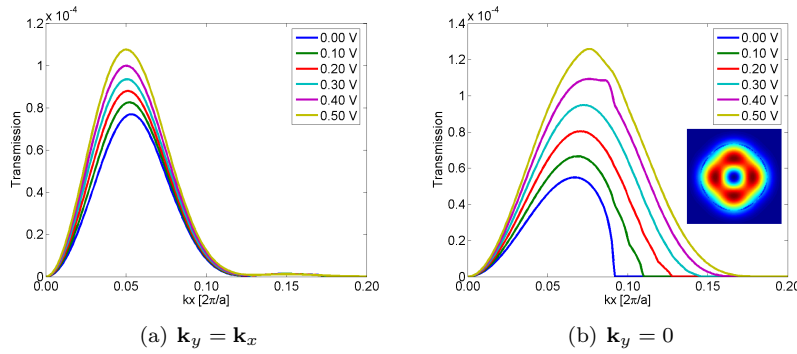


Figure 6.7: Transmission spectra for a single spin-channel in the anti-parallel magnetization configuration of the Fe/MgO system calculated along the line where $\mathbf{k}_x = \mathbf{k}_y$ (identical to Figure 6.6a) and along the line where $\mathbf{k}_y = 0$. The insert shows the \mathbf{k}_\parallel -resolved transmission spectrum for $E = E_F$ at $V = 0.5$ V (only the center of the two-dimensional Brillouin zone is shown). The transmission increases more along $\mathbf{k}_y = 0$ than along $\mathbf{k}_x = \mathbf{k}_y$.

increases more along $\mathbf{k}_y = 0$ than along $\mathbf{k}_x = \mathbf{k}_y$.

We note that the single-band tight-binding model by Raza and Raza [107], which is based on $\mathbf{k}_\parallel = \mathbf{0}$ phenomenology, cannot reproduce the characteristics measured (and calculated) for Co/MgO systems at low voltages. The model finds an infinite value of the TMR below $V \approx 0.24$ V since the majority- and minority-spin bands for $\mathbf{k}_\parallel = \mathbf{0}$ have different symmetries (above $V \approx 0.24$ V a minority-spin Δ_1 band enters the energy integration window contributing to the current, as discussed below). Again we emphasize the importance of tunneling with $\mathbf{k}_\parallel \neq \mathbf{0}$ when the electrodes are magnetized in opposite directions. We discuss the influence of the minority-spin Δ_1 band presently.

Influence of minority-spin Δ_1 band in the Co/MgO system

The Co electrode has a minority-spin Δ_1 band which has its bottom 0.24 eV above the Fermi energy. This band enters the energy integration window when the bias voltage reaches 0.24 V and Δ_1 to Δ_1 tunneling becomes possible. Below this “turn-on” voltage, V_c , the band does not occupy any fraction of the window, while it occupies $1 - V_c/V$ above the “turn-on” voltage. The spin-dependent band structures of the Co electrode are shown again in Figure 6.8. Only the

¹Waldron *et al.* [84] observe a similar increase in the height of the peaks along the lines where $|\mathbf{k}_x| = |\mathbf{k}_y|$ for a similar magnetic tunnel junction at $V = 0.05$ V.

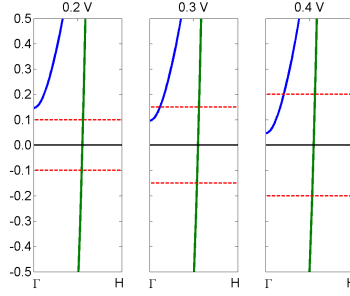


Figure 6.8: Majority-spin (green) and minority-spin (blue) Δ_1 bands in the Co electrode under the influence of a finite bias voltages. The majority-spin band of one electrode is raised $eV/2$ by the voltage while the minority-spin band of the other electrode is lowered correspondingly. The minority-spin Δ_1 band begins 0.24 eV above the Fermi energy at zero bias and enters the energy window contributing to the current when $V \approx 0.24$ V.

Δ_1 bands are shown, and the effect of applying a bias voltage is visualized. To demonstrate the effect of the gradual increase in the contribution from Δ_1 to Δ_1 tunneling Figure 6.9 shows the transmission at different energies for $V = 0.5$ V. The figure shows how only the transmissions for $E > (eV_c - eV/2)$ show

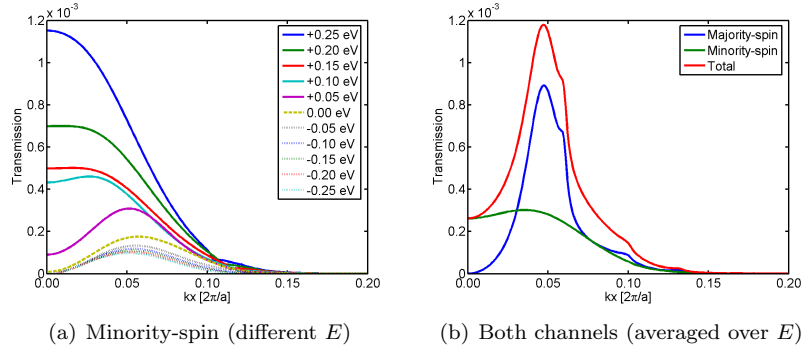


Figure 6.9: Transmission along $\mathbf{k}_x = \mathbf{k}_y$ in the anti-parallel configuration of the Co/MgO magnetic tunnel junction for $V = 0.5$ V. Left: minority-spin channel for different energies. Right: Both spin-channels, averaged over energies. The transmission is affected by the minority-spin Δ_1 band above $E = eV_c - eV/2$.

sign of the Δ_1 state, and that only the top $1 - V_c/V$ fraction of the energy window therefore has contribution from the Δ_1 band. The figure also shows the averaged transmission in the two spin-channels. The band leads to an increase in transmission at $\mathbf{k}_{\parallel} \approx \mathbf{0}$ but does not influence the current significantly in the voltage range examined in this work. At $V = 0.5$ V the band only occupies 40% of the integration window, and combined with a relatively low coupling between the majority-spin Δ_1 state in one electrode and the minority-spin Δ_1 state in the other electrode the transmission due to this band is small.

6.4 Voltage dependence of the tunneling mechanisms

Having discussed the tunneling mechanisms under zero-bias conditions in the previous chapter, and discussed the influence of a bias voltage on the \mathbf{k}_{\parallel} -resolved transmission spectra in the previous sections, we proceed to analyze the voltage dependence of the tunneling mechanisms. To this end we investigate the origin of the main features in the current/voltage characteristics shown in Figure 6.1, *i.e.* the reasons underlying the bias-induced changes in transmission discussed in the previous sections. In Figure 6.10 we show the energy dependence of the transmission coefficients, calculated at zero bias using a 21×21 k-point sampling of the two-dimensional Brillouin zone, together with the current/voltage characteristics calculated using a simplified version of Equation 2.43 in which $T_{\sigma}(V, E) \approx T_{\sigma}(0, E)$,

$$I_{\sigma}(V) \approx \frac{e}{h} \int_{-eV/2}^{eV/2} T_{\sigma}(0, E) dE \quad (6.2)$$

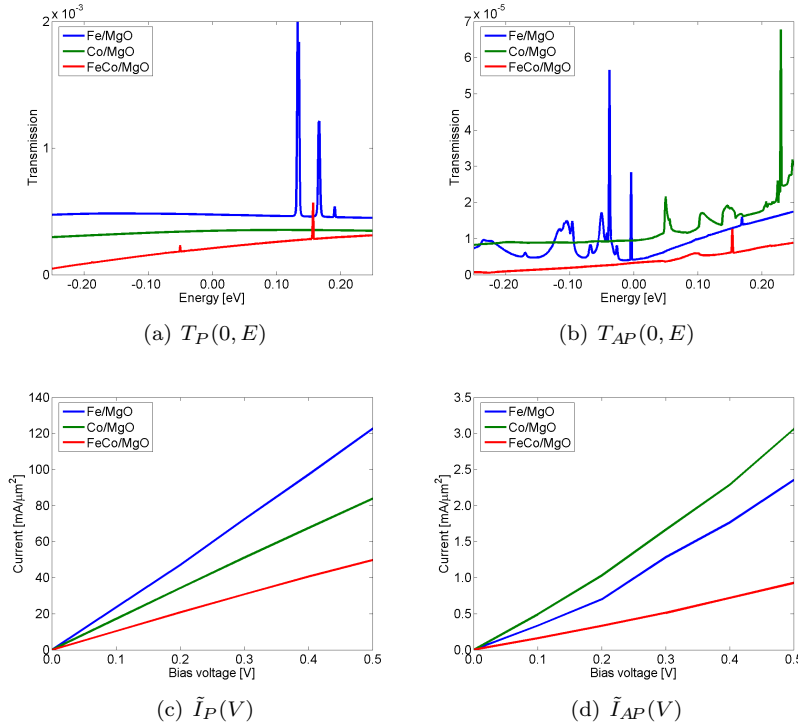


Figure 6.10: Zero-bias transmission spectra, $T(0, E)$, for the three systems in the parallel configuration (a) and anti-parallel configuration (b) along with the corresponding current/voltage characteristics (c and d) obtained from Equation 6.2.

The current/voltage characteristics obtained using Equation 6.2 are in agreement with the ones shown in Figure 6.1. In the Fe/MgO and Co/MgO systems

the current increases linearly with increasing bias voltage in the parallel configuration and super-linearly in the anti-parallel configuration. In the FeCo/MgO system the current increases linearly in both configurations.

Generally, the current depends on the transmission function, $T_\sigma(V, E)$, which is a function of both V and E . In the simplified version of Equation 2.43 (Equation 6.2) the transmission function at finite bias is approximated by the zero-bias transmission function, $T_\sigma(V, E) \approx T_\sigma(0, E)$. Since the current/voltage characteristics found using the two equations are similar (compare Figures 6.1 and 6.10) we therefore conclude that the main features in the current/voltage characteristics arise from the energy dependence of the transmission coefficient (not from the voltage dependence).

For all three systems the transmission coefficient, $T(0, E)$, in the parallel configuration is approximately a linear function of energy (Figure 6.10), which is due to the simple tunneling of Δ_1 states. The transmission function gives rise to a linear increase in current with the voltage. We note that the current/voltage characteristics for the FeCo/MgO system in the parallel configuration shown in Figure 6.10 do not agree with those shown in Figure 6.1 above $V \approx 0.3$ V. At this voltage the differential conductance decreases in Figure 6.1 when the bottom of the majority-spin Δ_1 band, which is located approximately 0.3 eV below the Fermi energy, enters the energy integration window (see the discussion earlier in this chapter). In the approximation defined by Equation 6.2 the bottom enters when $V \approx 0.6$ V, *i.e.* at twice the voltage, since the shifting of the bands by the bias voltage has been ignored. The decrease in differential conductance when the Δ_1 band enters the energy integration window is responsible for the decrease in TMR in the FeCo/MgO system above $V \approx 0.3$ V.

In the anti-parallel configuration the energy dependence of the transmission coefficient is more complex. The complexity arises from a strong energy dependence of the coupling between the barrier wave functions with Δ_1 features and the outgoing Bloch states with Δ_5 , $\Delta_{2'}$, and Δ_2 features. In the Fe/MgO system the transmission increases both above and below the Fermi energy, and in the Co/MgO system it increases above while remaining constant below. This leads to a super-linear increase in current with increasing bias voltage. In the FeCo/MgO system the transmission increases linearly with the energy, resulting in a linear increase in current with increasing voltage. The details of the current/voltage characteristics are related to the complex symmetries of the electrode states with Δ_5 , $\Delta_{2'}$, and Δ_2 features, which change with both E and \mathbf{k}_\parallel .

6.5 Summary

We have in this chapter examined the current/voltage characteristics of the three magnetic tunnel junctions which were set up and optimized in Chapter 4 (Fe/MgO, Co/MgO, and FeCo/MgO).

The current increases linearly with the voltage in the parallel magnetization configuration of the Fe/MgO and Co/MgO systems. In the FeCo system the differential conductance decreases above $V \approx 0.3$ V. In the anti-parallel configuration the current increases super-linearly in the Fe/MgO and Co/MgO systems and linearly in the FeCo/MgO system. These current/voltage characteristics result in a decreasing value of the tunneling magnetoresistance with

voltage in all three systems, although the TMR remains almost constant below $V \approx 0.3$ V in the FeCo system.

These characteristics are due to the differences in tunneling mechanisms discussed in the previous chapter. In the parallel configuration the transmission coefficient is approximately a linear function of energy, while the energy dependence of the transmission coefficient in the anti-parallel configuration shows more structure.

Calculating the current based on a simple model, in which the only effect of the bias voltage is to increase the size of the energy integration window, we find results with trends similar to those found in the more full calculations. We therefore conclude that the main features in the current/voltage characteristics are not related to the voltage drop, but arise from the energy dependence of the transmission coefficient.

Chapter 7

Conclusions and perspectives

In this thesis we have described the results of first-principles calculations of the structural, zero-bias, and finite-bias properties of Magnesium oxide (MgO) based magnetic tunnel junctions with Iron (Fe), Cobalt (Co), and Iron-Cobalt (FeCo) electrodes. In the system with FeCo electrodes a Co layer interfaces the MgO barrier.

In Chapter 1 we introduced magnetic tunnel junctions and discussed the current status of the research field and the commercial efforts to use these spintronic systems in the read heads of hard disk drives and magnetic random access memory. In Chapter 2 we gave an overview of the many-electron theory and quantum transport formalism used for calculations in this work.

In Chapter 3 we used the density functional theory/non-equilibrium Green's functions methods implemented in the software package Atomistix ToolKit to study the bulk properties of body-centered cubic Fe and Co as well as rock salt MgO. The calculation results were found to be in agreement with experimental and numerical reference data found in the literature. We also used the software to model the spin-transport properties of the Fe/MgO/Fe magnetic tunnel junctions analyzed by Butler *et al.* in Reference [1]. The results were consistent with those found in the original work.

In Chapter 4 we set up three magnetic tunnel junctions consisting of five-layer insulating MgO barriers sandwiched between ferromagnetic Fe, Co, or FeCo electrodes. The geometries of the systems were optimized and the structural properties were examined. In Chapter 5 we studied the tunneling conductance and tunneling mechanisms of the three magnetic tunnel junctions under zero-bias conditions, and in Chapter 6 we studied the current/voltage characteristics of the systems.

We here summarize the main results of the work, draw conclusions, and set the work in perspective.

7.1 Conclusions

Structural properties

The MgO barriers of the three magnetic tunnel junctions have rock salt crystal structure and their (001) planes interface the (001) planes of the electrodes, which have body-centered cubic structure (Fe and Co) and B2 structure (FeCo). The [001] direction in the electrodes is parallel to the [110] direction in the barriers. The systems are shown for convenience in Figure 7.1. They are referred to

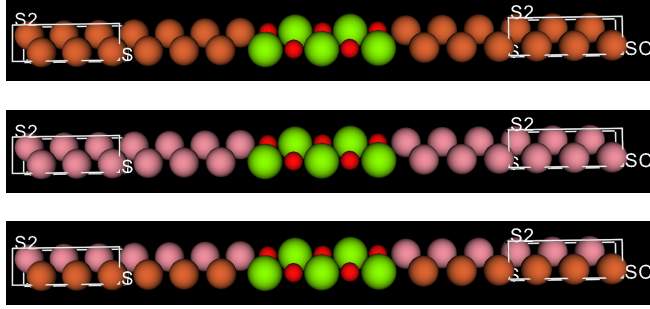


Figure 7.1: The three magnetic tunnel junctions studied in this work. Fe atoms are represented by brown spheres, Co atoms are purple, Mg atoms are green, and O atoms are red. (Identical to Figure 4.5).

as Fe/MgO, Co/MgO, and FeCo/MgO. The structural properties of the systems are summarized in Table 7.1. The distances between the Mg and O atoms in the

	d_1	d_2	d_3
Fe/MgO	-2%	2.17 Å	+0.07 Å
Co/MgO	-4%	2.16 Å	+0.09 Å
FeCo/MgO	-7%	2.16 Å	+0.08 Å

Table 7.1: Main structural parameters for the systems considered in this work (see text). d_1 is the distance between the two electrode layers closest to the barrier given in percentile variation with respect to the corresponding bulk distance of 2.795 Å (Fe and FeCo) or 2.794 Å (Co). d_2 is the distance between the closest electrode and oxygen layers. d_3 is the displacement of the outermost Mg atoms towards the electrodes, cf. Figure 7.1. (Identical to Table 4.1).

outer-most layers in the barrier is approximately +0.08 Å for all three systems. The distance between the barrier O atoms and the closest electrode layers is approximately 2.17 Å. The distances between the electrode layers closest to the barrier varies slightly for the three systems but remains close to the bulk values.

Tunneling conductance and current/voltage characteristics

For each system the calculated tunneling conductance (G) is listed in Table 7.2 along with the calculated and experimental values of the tunneling magnetoresistance (TMR). We observe the following for the conductance in the parallel- and anti-parallel magnetization configurations:

	G_P	G_{AP}	TMR	TMR (exp.)
Fe/MgO	239	3.23	$\approx 7300\%$	247% [42]
Co/MgO	179	4.88	$\approx 3600\%$	507% [31]
FeCo/MgO	106	1.54	$\approx 6800\%$	300% [5]

Table 7.2: Zero-bias conductance with parallel (G_P) and anti-parallel (G_{AP}) magnetization of the electrodes along with calculated values of the TMR for the three magnetic tunnel junctions. The conductances are in units of $\text{mS}/\mu\text{m}^2$ and the TMR values are listed along with experimental results measured at low temperature. The experimental systems have approximately twice the number of layers as the systems discussed in this work. (Identical to Table 5.1).

- $G_P \gg G_{AP}$
- $G_{P\uparrow} \gg G_{P\downarrow}$
- $G_{AP\uparrow} = G_{AP\downarrow}$

G_P and G_{AP} are the conductances in the two configurations, $G_{P\uparrow}$ and $G_{P\downarrow}$ are the majority- and minority-spin conductances in the parallel configuration, and $G_{AP\uparrow}$ and $G_{AP\downarrow}$ are the corresponding conductances in the anti-parallel configuration. We note that the conductance is largest is the system with Fe electrodes and, supported by studies of an FeCo/MgO system with Fe/MgO interfaces, we conclude that Fe couples more efficiently to the barrier than Co. The TMR has similar size in the three systems. It is significantly larger than measured experimentally.

The calculated current/voltage characteristics are shown in Figure 7.2. We

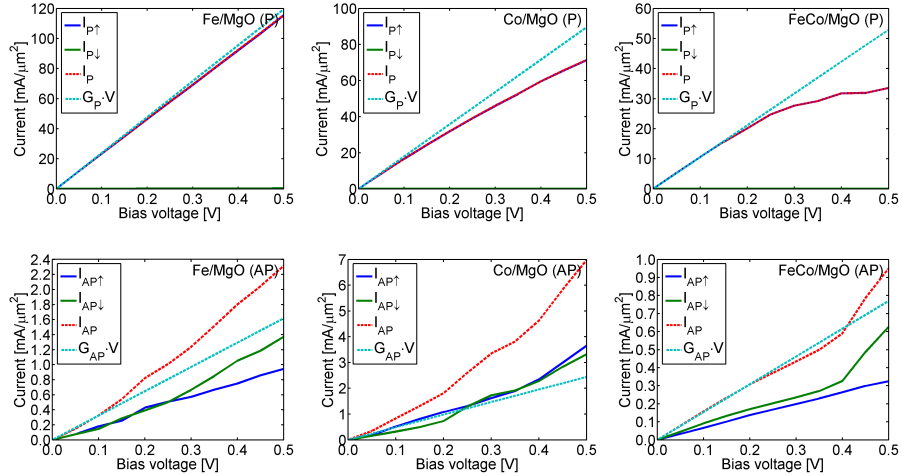


Figure 7.2: Current/voltage characteristics of the three magnetic tunnel junctions showing the current in the two spin-channels of the parallel- (left column) and anti-parallel magnetization configurations (right column) as well as the total current and the current calculated from the zero-bias conductance. (Identical to Figure 6.1).

observe the following for the current in the parallel- and anti-parallel configurations:

- $I_P \gg I_{AP}$
- I_P increases linearly with V (Fe/MgO, Co/MgO)
- I_P increases sub-linearly (FeCo/MgO)
- I_{AP} increases super-linearly (Fe/MgO, Co/MgO)
- I_{AP} increases linearly (FeCo/MgO)

I_P and I_{AP} are the currents in the two configurations. The observations are made for the voltage range 0 – 0.5 V.

The tunneling magnetoresistance resulting from these current/voltage characteristics, shown in Figure 7.3, decreases with the applied bias voltage. It

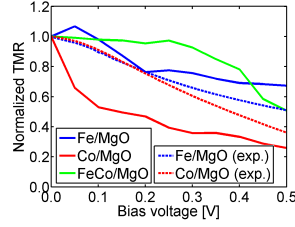


Figure 7.3: Voltage dependence of the TMR in the three magnetic tunnel junctions, normalized by the values found at $V = 0$ V. The experimental results reported in Reference [31] are shown with dashed lines. (Identical to Figure 6.2).

remains almost constant in the FeCo/MgO system below $V \approx 0.3$ V, however.

Spin-transport in the parallel magnetization configuration

Figure 7.4 shows the \mathbf{k}_{\parallel} -resolved transmission spectra for the majority-spin channels in the parallel magnetization configuration in the three magnetic tunnel junctions. The transmission spectra show similar trends for the three systems:

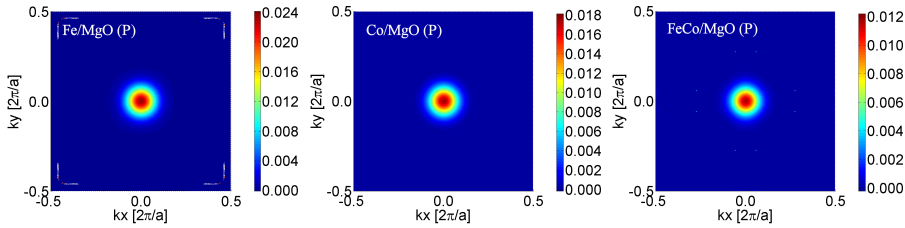


Figure 7.4: Transmission spectra for the majority-spin channels in the parallel magnetization configuration of the three magnetic tunnel junctions. (Identical to Figure 5.3).

they are dominated by broad peaks in the center of the two-dimensional Brillouin zone ($\mathbf{k}_{\parallel} = \mathbf{0}$). Spin-transport is dominated by tunneling from majority-spin Δ_1 states to majority-spin Δ_1 states, for which the decay rate in the barrier is much smaller than for other states.

The transmission maxima in the parallel magnetization configuration remain almost constant when a bias voltage is applied, and the current therefore increases almost linearly with the voltage. In the FeCo/MgO system the bottom of the Δ_1 band enters the energy integration window contributing to the current when $V \approx 0.3$ V and the differential conductance decreases.

Spin-transport in the anti-parallel magnetization configuration

The tunneling mechanisms in the anti-parallel magnetization configuration of the three magnetic tunnel junctions are more complex. The transmission spectra, shown in Figure 7.5, have four maxima away from the center of the Brillouin zone. The peaks are located along the lines where $|\mathbf{k}_x| = |\mathbf{k}_y|$ in the Fe/MgO

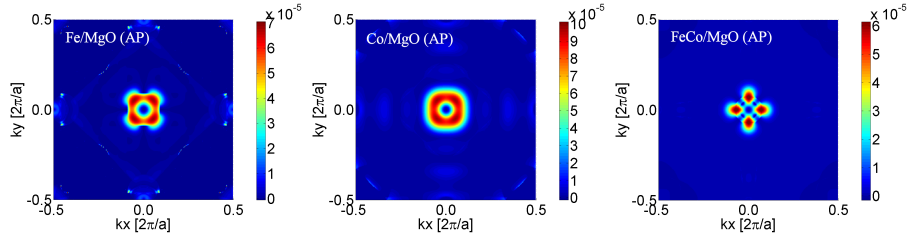


Figure 7.5: Transmission spectra for a single spin-channel in the anti-parallel magnetization configuration of the magnetic tunnel junctions. Four peaks are located away from the center of the two-dimensional Brillouin zone. (Identical to Figure 5.7).

and Co/MgO systems and along the lines where $\mathbf{k}_x = 0$ and $\mathbf{k}_y = 0$ in the FeCo/MgO system.

For $\mathbf{k}_\parallel \neq \mathbf{0}$ the Δ_1 bands found at $\mathbf{k}_\parallel = \mathbf{0}$ remain largely unchanged while the remaining bands change significantly. Tunneling occurs primarily from Δ_1 -like bands to bands with different symmetries. The transmission coefficients depend on the coupling of the Δ_1 state into the barrier wave functions, the decay rates of these, and the coupling to the states in the other electrode.

The height, shape, and location of the peaks in the transmission spectra change with the bias voltage and the energy. In the Fe/MgO and Co/MgO systems the average height increases with the bias voltage, leading to a super-linear increase in the current with the voltage. This is shown for the Fe/MgO system in Figure 7.6. In the FeCo/MgO system the peaks maintain their height and the current increases linearly.

Voltage dependence of the tunneling mechanisms

Figure 6.10 shows the energy-resolved zero-bias transmission spectra for the three systems. In the parallel configuration the transmission coefficient is an almost linear function of energy, which may be understood from the simple tunneling of the Δ_1 states involving only a single band in the left and right electrodes. In the anti-parallel configuration the energy dependence of the transmission coefficient shows more structure. The structure arises from a strong energy dependence of the coupling between incoming states with Δ_1 features to

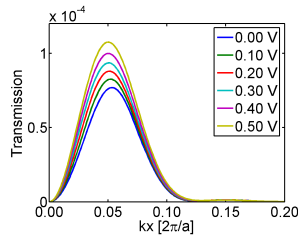


Figure 7.6: Transmission spectra for a single spin-channel in the anti-parallel magnetization configuration of the Fe/MgO system calculated along the line where $k_x = k_y$. (Identical to Figure 6.6).

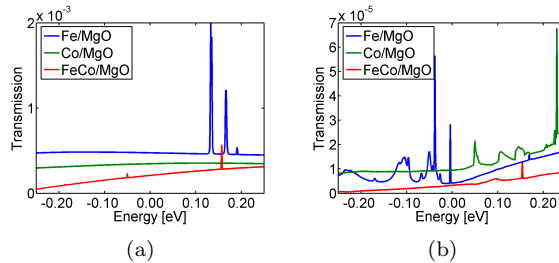


Figure 7.7: Zero-bias transmission spectra, $T(0, E)$, for the three systems in the parallel- (a) and anti-parallel configurations (b). (Identical to Figure 6.10).

outgoing states with Δ_5 , $\Delta_{2'}$, and Δ_2 features. The coupling is related to the shape of the wavefunctions with Δ_5 , $\Delta_{2'}$, and Δ_2 features.

A simple model for the current, in which the effect of the bias voltage is to sample an energy window in the spectra in Figure 7.7, gives trends similar to the more full calculations. We conclude that the main features in the current/voltage characteristics are not related to the voltage drop, but arise from the energy dependence of the transmission coefficient.

7.2 Perspectives

Prior to this work Fe/MgO systems have been extensively modeled. Structural optimizations [1, 84, 86] and studies of zero-bias [1, 2, 84, 85, 86, 87, 90] and finite-bias [84, 85, 87, 90] spin-transport properties have been performed and results are available in the literature. To our knowledge, only a single numerical zero-bias study is available for Co/MgO and FeCo/MgO systems [66] and no structural optimizations or finite-bias studies have been conducted. Our work includes studies of both the structural, zero-bias, and finite-bias properties of all three systems, and we thereby contribute to the overall knowledge base of the scientific field.

Our emphasis on tunneling with $k_{\parallel} \neq 0$ when the electrodes are magnetized in opposite directions breaks with the current paradigm of the field, which has a strong focus on $k_{\parallel} = 0$ physics. For $k_{\parallel} = 0$ the Bloch states in the electrodes have Δ_1 , Δ_5 , $\Delta_{2'}$, or Δ_2 symmetry and the tunneling mechanisms are well un-

derstood. For $\mathbf{k}_{\parallel} \neq \mathbf{0}$ the electrode states do not have “pure” Δ symmetries, and the tunneling mechanisms are more complex. In the parallel magnetization configuration the conductance is dominated by tunneling with $\mathbf{k}_{\parallel} \approx \mathbf{0}$, and $\mathbf{k}_{\parallel} = \mathbf{0}$ phenomenology provides an elegant and accurate description of the transport processes. In the anti-parallel configuration the conductance is dominated by tunneling with $\mathbf{k}_{\parallel} \neq \mathbf{0}$, and $\mathbf{k}_{\parallel} = \mathbf{0}$ phenomenology does not capture the most significant processes. The $\mathbf{k}_{\parallel} = \mathbf{0}$ model of Raza and Raza [107], for example, cannot capture the properties of Co/MgO or FeCo/MgO systems for low voltages.

Our results show that mainly the electronic structure of the electrodes and the electrode/barrier coupling determine the spin-transport properties of MgO-based magnetic tunnel junctions. Band engineering and control of interface properties are therefore tools that can be used to develop systems suitable for applications. A junction with the following properties will offer high TMR and low resistance:

- A majority-spin Δ_1 band spans a broad energy window centered on E_F .
- No minority-spin Δ_1 band is available in this window.
- The Δ_1 state couples strongly to slowly decaying barrier wave functions.
- The barrier wave functions couple weakly to minority-spin states.

In such a junction the conductance in the parallel magnetization configuration will be much larger than in the anti-parallel configuration, and the TMR will remain large at finite bias.

In commercial use of magnetic tunnel junctions, in the read heads of hard disk drives and the memory cells in magnetic random access memory devices, crude sputtering techniques are used for device fabrication in order to keep costs down. This leads to non-crystalline junctions with different kinds of defects. Furthermore, electrode materials are doped in order to provide the required magnetic properties. FeCo electrodes are, for example, doped with Boron (B) in order to decrease the magnetostriction coefficient and make the electrode sufficiently “free” to respond to external magnetic fields [10]. In numerical studies, such as those discussed in this work, system geometries are idealized and without defects, doping, or other “non-ideal” features. This gives rise to fundamental differences between experimental and numerical data, and direct comparison is often impossible. In order to “bridge the gap” numerical models must take into account such features. The density functional theory/non-equilibrium Green’s functions approach used in this work is useful for providing insights into tunneling mechanisms and to predict and understand the trends of device components during initial development phases. Other tools, which require fewer computational resources and less time, and which take into account the effects of defects, doping, *etc.*, will be useful for modeling at the device level during later phases of development. Such models are currently under development in both academic and commercial organizations.

There is no doubt that MgO-based magnetic tunnel junctions will appear in commercial storage and memory products in the near future. This work provides a little piece of understanding useful in the development of such technologies. It is the Author’s hope that others will pick up where this work leaves off, and

that the content of the thesis — along with future work — will help pave the way for commercial devices useful in common consumer products.

Bibliography

- [1] *Spin-dependent tunneling conductance of Fe-MgO-Fe sandwiches*
by W. H. Butler, X.-G. Zhang, T. C. Schulthess, and J. M. MacLaren
Physical Review B, Volume 63, January 2001
- [2] *Theory of tunneling magnetoresistance of an epitaxial Fe/MgO/Fe(001) junction*
by J. Mathon and A. Umerski
Physical Review B, Volume 63, May 2001
- [3] *Single-crystal magnetotunnel junction*
by W. Wulfhekkel, M. Klaua, D. Ullmann, F. Zavaliche, J. Kirschner, R. Urban, T. Monchesky, and B. Heinrich
Applied Physics Letters, Volume 78, Number 4, January 2001
- [4] *Geometrical and compositional structure at metal-oxide interfaces: MgO on Fe(001)*
by H. L. Meyerheim, R. Popescu, J. Kirschner, N. Jedrecy, M. Sauvage-Simkin, B. Heinrich, and R. Pinchaux
Physical Review Letters, Volume 87, Number 7, August 2001
- [5] *Giant tunnelling magnetoresistance at room temperature with MgO(100) tunnel barriers*
by Stuart S. P. Parkin, Christian Kaiser, Alex Panchula, Philip M. Rice, Brian Hughes, Mahesh Samant, and See-Hun Yang
Nature Materials, Volume 3, December 2004
- [6] *230% room-temperature magnetoresistance in CoFeB/MgO/CoFeB magnetic tunnel junctions*
by David D. Djayaprawira, Koji Tsunekawa, Motonobu Nagai, Hiroki Maehara, Shinji Yamagata, Naoki Watanabe, Shinji Yuasa, Yoshishige Suzuki, and Koji Ando
Applied Physics Letters, Volume 86, February 2005
- [7] *Development of the magnetic tunnel junction MRAM at IBM: From first junctions to a 16-Mb MRAM demonstrator chip*
by W. J. Gallagher and S. S. P. Parkin
IBM Journal of Research and Development, Volume 50, Number 1, January 2006
- [8] *Atomic and electronic structure of the CoFeB/MgO interface from first principles*

- by J. D. Burton, S. S. Jaswal, E. Y. Tsymbal, O. N. Mryasov, and O. G. Heinonen
Applied Physics Letters, Volume 89, October 2006
- [9] *Significant reduction of coercivity without reduction of tunneling magnetoresistance ratio of CoFeB/MgO/CoFeB-based magnetic tunnel junction using sandwich-structured free layer*
by Young-suk Choi and Koji Tsunekawa
Applied Physics Letters, Volume 91, October 2007
- [10] *Magnetic tunnel junctions*
by Jian-Gang Zhu and Chando Park
Materials Today, Volume 9, Number 11, November 2006
- [11] *Giant tunnel magnetoresistance in magnetic tunnel junctions with a crystalline MgO(001) barrier*
by S. Yuasa and D. D. Djayaprawira
Journal of Physics D: Applied Physics, Volume 40, October 2007
- [12] *Magnetoresistance in MgO-based tunnel junctions with Fe, Co, and FeCo electrodes*
by Morten Stilling, Hector Mera, Davide Ricci, Søren Smidstrup, Jeremy Taylor, and Kurt Stokbro
Under preparation
- [13] *First-principles Modeling of Magnetic Memory Components — Preliminary Results on the Effects of Interface Oxides*
by Morten Stilling and Kurt Stokbro
Proceedings of NSTI-Nanotech 2007, Volume 1, May 2007
- [14] *Electronic transport in crystalline magnetotunnel junctions: effects of structural disorder*
by Morten Stilling, Kurt Stokbro, and Karsten Flensberg
Journal of Computer-Aided Materials Design, Volume 14, January 2007
- [15] *Crystalline magnetotunnel junctions: Fe-MgO-Fe, Fe-FeOMgO-Fe and Fe-AuMgOAu-Fe*
by Morten Stilling, Kurt Stokbro, and Karsten Flensberg
Molecular Simulation, Volume 33, Number 7, June 2007
- [16] The Nobel Prize in Physics 1956
Announcement on nobelprize.org
Link to online document (pdf version only)
- [17] *Transistor technology evokes new physics*
by William Shockley
Nobel Lecture, December 1956
- [18] *Semiconductor research leading to the point contact transistor*
by John Bardeen
Nobel Lecture, December 1956

-
- [19] *Surface properties of semiconductors*
by Walter H. Brattain
Nobel Lecture, December 1956
- [20] The Nobel Prize in Physics 2000
Announcement on nobelprize.org
Link to online document (pdf version only)
- [21] *Turning potential into realities: The invention of the integrated circuit*
by Jack S. Kilby
Nobel Lecture, December 2000
- [22] *Cramming more components onto integrated circuits*
by Gordon E. Moore
Electronics, Volume 38, Number 8, April 1965
- [23] *No exponential is forever — but we can delay “forever”*
by Gordon E. Moore
Slide show on intel.com
Link to online document (pdf version only)
- [24] 60 years of the transistor: 1947–2007
Document on intel.com
Link to online document (pdf version only)
- [25] World’s First 2-Billion Transistor Microprocessor
Announcement on intel.com
Link to online document (pdf version only)
- [26] Random access memory
Article on wikipedia.org
Link to online document (pdf version only)
- [27] *Spintronics — A retrospective and perspective*
by S. A. Wolf, A. Y. Chtchelkanova, and D. M. Treger
IBM Journal of Research and Development, Volume 50, Number 1, January 2006
- [28] Cheetah 15K.6 Hard Drives
Press Releases on seagate.com
Link to online document (pdf version only)
- [29] *Spintronics*
by the Engineering and Physical Sciences Research Council
Report on epsrc.ac.uk, June 2006
Link to online document (pdf version only)
- [30] *Atomistix Introductory Training Course — Handout*
by the Technology Consulting Department
Atomistix A/S, June 2007
- [31] *Giant tunneling magnetoresistance up to 410% at room temperature in fully epitaxial Co/MgO/Co magnetic tunnel junctions with bcc Co(001) electrodes*

- by Shinji Yuasa, Akio Fukushima, Hitoshi Kubota, Yoshishige Suzuki, and Koji Ando
Applied Physics Letters, Volume 89, July 2006
- [32] *Prize for Industrial Applications of Physics*
Announcement on aip.org
Link to online document (pdf version only)
- [33] The Nobel Prize in Physics 2007
Announcement on nobelprize.org
Link to online document (pdf version only)
- [34] *The Origin, the Development and the Future of Spintronics*
by Albert Fert
Nobel Lecture, December 2007
- [35] *From Spinwaves to Giant Magnetoresistance (GMR) and Beyond*
by Peter Grünberg
Nobel Lecture, December 2007
- [36] *CPP Read-Head Technology Enables Smaller Form Factor Storage*
Fujitsu whitepaper, 2006
Link to online document (pdf version only)
- [37] *Tunneling between ferromagnetic films*
by M. Julliere
Physics Letters, Volume 54A, Number 3, September 1975
- [38] *Band structure, evanescent states, and transport in spin tunnel junctions*
by X.-G. Zhang and W. H. Butler
Journal of Physics: Condensed Matter, Volume 15, October 2003
- [39] *Validity of the Julliere model of spin-dependent tunneling*
by J. M. MacLaren, X.-G. Zhang, and W. H. Butler
Physical Review B, Volume 56, Number 18, November 1997
- [40] *Large magnetoresistance at room temperature in ferromagnetic thin film tunnel junctions*
by J. S. Moodera, Lisa R. Kinder, Terrilyn M. Wong, and R. Meservey
Physical Review Letters, Volume 74, Number 16, April 1995
- [41] *70% TMR at room temperature for SDT sandwich junctions with CoFeB as free and reference Layers*
by Wang Dexin, C. Nordman, J. M. Daughton, Qian Zhenghong, and J. Fink
IEEE Transactions on Magnetics, Volume 40, Issue 4, July 2004
- [42] *Giant room-temperature magnetoresistance in single-crystal Fe/MgO/Fe magnetic tunnel junctions*
by Shinji Yuasa, Taro Nagahama, Akio Fukushima, Yoshishige Suzuki, and Koji Ando
Nature Materials, Volume 3, December 2004

- [43] *Effect of electrode composition on the tunnel magnetoresistance of pseudo-spin-valve magnetic tunnel junction with a MgO tunnel barrier*
by Y. M. Lee, J. Hayakawa, S. Ikeda, F. Matsukura, and H. Ohno
Applied Physics Letters, Volume 90, May 2007
- [44] *Hitachi achieves nanotechnology milestone for quadrupling terabyte hard drive*
Hitachi press release, October 2007
Link to online document (pdf version only)
- [45] *2006 hard disk drive capital equipment market and technology report*
by Coughlin Associates
San Jose, California, June 2006
Link to online document (pdf version only)
- [46] *Conquering the Market for Spintronics Modeling Tools*
by Morten Stilling
Atomistix A/S, March 2007
- [47] *Is nonvolatile MRAM right for your consumer embedded device application?*
by Tom Lee
Article on embedded.com, February 2007
Link to online document (pdf version only)
- [48] *Expectations of MRAM in comparison with other non-volatile memory technologies*
by K.-M.H. Lenssen, G.J.M. Dormans, R. Cuppens
Non-volatile Memory Technology Symposium Proceedings, 2000
- [49] *The Budding Market for MRAM: An Analysis*
by Lawrence Gasman
Magnetics Business & Technology, Winter 2005
- [50] *'Universal' memory market to hit \$75 billion in 2019, says iSuppli*
Article on mram-info.com, July 2005
Link to online document (pdf version only)
- [51] *Classical Nuclear Motion in Quantum Transport*
by Claudio Verdozzi, Gianluca Stefanucci, and Carl-Olof Almbladh
Physical Review Letters, Volume 97, July 2006
- [52] *Modern Quantum Chemistry — Introduction to Advanced Electronic Structure Theory*
by Attila Szabo and Neil S. Ostlund
Dover Publications, 1996
ISBN: 0-486-69186-1
- [53] *The SIESTA method for ab initio order-N materials simulation*
by José M Soler, Emilio Artacho, Julian D. Gale, Alberto García, Javier Junquera, Pablo Ordejón, and Daniel Sánchez-Portal
Journal of Physics: Condensed Matter, Volume 14, March 2002

- [54] *Molecular Quantum Mechanics*, Fourth edition
by Peter Atkins and Ronald Friedman
Oxford University Press, 2005
ISBN: 0-19-927498-3
- [55] *Nobel Lecture: Electronic structure of matter — wave functions and density functionals*
by W. Kohn
Reviews of Modern Physics, Volume 71, Number 5, October 1999
- [56] *Density-Functional Theory of Atoms and Molecules*
by Robert G. Parr and Weitao Yang
Oxford University Press, 1989
ISBN: 0-19-504279-4
- [57] *Inhomogeneous electron gas*
by P. Hohenberg and W. Kohn
Physical Review, Volume 136, Number 3B, November 1964
- [58] *Multicomponent Density-Functional Theory for Electrons and Nuclei*
by T. Kreibich and E. K. U. Gross
Physical Review Letters, Volume 86, Number 14, April 2001
- [59] *Self-consistent equations including exchange and correlation effects*
by W. Kohn and L. J. Sham
Physical Review, Volume 140, Number 4A, November 1965
- [60] *Generalized gradient approximation made simple*
by John P. Perdew, Kieron Burke, and Matthias Ernzerhof
Physical Review Letters, Volume 77, Number 18, October 1996
- [61] *Molecular and Solid-State Tests of Density Functional Approximations: LSD, GGAs, and Meta-GGAs*
by Stefan Kurth, John P. Perdew, and Peter Blaha
International Journal of Quantum Chemistry, Volume 75, 1999
- [62] *Density Functional Theory: Basics, New Trends and Applications*
by J. Kohanoff and N.I. Gidopoulos
Handbook of Molecular Physics and Quantum Chemistry, 2003
Volume 2, Part 5, Chapter 26, pages 532–568
ISBN: 0-471-62374-1
- [63] *Ab-initio modelling of transport in atomic scale devices*
by Jeremy Taylor
Ph.D. Thesis, 2000
- [64] *Ab initio modeling of quantum transport properties of molecular electronic devices*
by Jeremy Taylor, Hong Guo, and Jian Wang
Physical Review B, Volume 63, June 2001
- [65] *Density-functional method for nonequilibrium electron transport*
by Mads Brandbyge, José-Luis Mozos, Pablo Ordejón, Jeremy Taylor, and Kurt Stokbro
Physical Review B, Volume 65, March 2002

- [66] *Large magnetoresistance in bcc Co/MgO/Co and FeCo/MgO/FeCo tunnel junctions*
by X.-G. Zhang and W. H. Butler
Physical Review B, Volume 70, November 2004
- [67] *A local exchange-correlation potential for the spin polarized case: I*
by U von Barth and L Hedin
Journal of Physics C: Solid State Physics, Volume 5, 1972
- [68] *Tests of a ladder of density functionals for bulk solids and surfaces*
by Viktor N. Staroverov, Gustavo E. Scuseria, Jianmin Tao, and John P. Perdew
Physical Review B, Volume 69, February 2004
- [69] *Ultrasoft spin-dependent pseudopotentials*
by Vincent Cocula, Chris J. Pickard, Emily A. Cartera
The Journal of Chemical Physics, Volume 123, December 2005
- [70] *Density-functional theory modeling of bulk magnetism with spin-dependent pseudopotentials*
by Frank Starrost, Hanchul Kim, Stuart C. Watson, Efthimios Kaxiras, and Emily A. Carter
Physical Review B, Volume 64, November 2001
- [71] *Ultrasoft pseudopotentials applied to magnetic Fe, Co, and Ni: From atoms to solids*
by E. G. Moroni, G. Kresse, J. Hafner, and J. Furthmüller
Physical Review B, Volume 56, Number 24, December 1997
- [72] *Quasiparticle band structure based on a generalized Kohn-Sham scheme*
by F. Fuchs, J. Furthmüller, F. Bechstedt, M. Shishkin, and G. Kresse
Physical Review B, Volume 76, September 2007
- [73] *Accurate Exchange-Correlation Potential for Silicon and Its Discontinuity on Addition of an Electron*
by R. W. Godby, M. Schlüter, and L. J. Sham
Physical Review Letters, Volume 56, Number 22, June 1986
- [74] Atomistix ToolKit — Online Manual
User's manual on atomistix.com
Link to online document (pdf version only)
- [75] *Quantum ballistic and adiabatic electron transport studied with quantum point contacts*
by B. J. van Wees, L. P. Kouwenhoven, E. M. M. Willems, C. J. P. M. Harman, J. E. Mooij, H. van Houten, C. W. J. Beenakker, J. G. Williamson, and C. T. Foxon
Physical Review B, Volume 43, Number 15, May 1991
- [76] *Formation and manipulation of a metallic wire of single gold atoms*
by A. I. Yanson, G. Rubio Bollinger, H. E. van den Brom, N. Agraït, and J. M. van Ruitenbeek
Nature, Volume 395, October 1998

- [77] *Electronic Transport in Mesoscopic Systems*
by Supriyo Datta
Cambridge University Press, 1995
ISBN: 0-521-59943-1
- [78] *Transmission eigenchannels from nonequilibrium Green's functions*
by Magnus Paulsson and Mads Brandbyge
Physical Review B, Volume 76, September 2007
- [79] *Direct calculation of the tunneling current*
by C. Caroli, R. Combescot, P. Nozieres, and D. Saint-James
Journal of Physics C: Solid State Physics, Volume 4, June 1971
- [80] *Time-dependent quantum transport: An exact formulation based on TDDFT*
by G. Stefanucci and C.-O. Almbladh
Europhysics Letters, Volume 67, Number 1, July 2004
- [81] *Quantum Kinetics in Transport and Optics of Semiconductors*
by H. Haug and A.-P. Jauho
Springer, 1996
ISBN: 3-540-61602-0
- [82] Applications of McDCal, TranSIESTA, TranSIESTA-C, Atomistix ToolKit
List of references on atomistix.com
Link to online document (pdf version only)
- [83] *TranSIESTA: A Spice for Molecular Electronics*
by Kurt Stokbro, Jeremy Taylor, Mads Brandbyge, and Pablo Ordejón
Molecular Electronics, Annals of the New York Academy of Sciences, Volume 1006, 2003
- [84] *Ab initio simulation of magnetic tunnel junctions*
by Derek Waldron, Lei Liu, and Hong Guo
Nanotechnology, Volume 18, September 2007
- [85] *Electronic transport through Fe/MgO/Fe(100) tunnel junctions*
by Ivan Rungger, Alexandre Reily Rocha, Oleg Mryasov, Olle Heinonen, and Stefano Sanvito
Journal of Magnetism and Magnetic Materials, Volume 316, March 2007
- [86] *Ab initio calculations of interface effects in tunnelling through MgO barriers on Fe(100)*
by D. Wortmann, G. Bihlmayer, and S. Blügel
Journal of Physics: Condensed Matter, Volume 16, November 2004
- [87] *Interface structure and bias dependence of Fe/MgO/Fe tunnel junctions: Ab initio calculations*
by Christian Heiliger, Peter Zahn, Bogdan Yu. Yavorsky, and Ingrid Mertig
Physical Review B, Volume 73, June 2006
- [88] *Effects of the iron-oxide layer in Fe-FeO-MgO-Fe tunneling junctions*
by X.-G. Zhang, W. H. Butler, and Amrit Bandyopadhyay
Physical Review B, Volume 68, September 2003

- [89] *Electronic structure and spin-dependent tunneling conductance under a finite bias*
by C. Zhang, X.-G. Zhang, P. S. Krstić, Hai-ping Cheng, W. H. Butler, and J. M. MacLaren
Physical Review B, Volume 69, April 2004
- [90] *Effect of interface states on spin-dependent tunneling in Fe/MgO/Fe tunnel junctions*
by K. D. Belashchenko, J. Velev, and E. Y. Tsymbal
Physical Review B, Volume 72, October 2005
- [91] *Pride, Prejudice, and Penury of ab initio transport calculations for single molecules*
by F. Evers and K. Burke
Unpublished, February 4 2008
arXiv:cond-mat/0610413v1 [cond-mat.mes-hall]
- [92] *Elastic constants of body-centered-cubic cobalt films*
by G. A. Subramanian, R. Sooryakumar, G. A. Prinz, B. T. Jonker, and Y. U. Idzerda
Physical Review B, Volume 49, Number 24, June 1994
- [93] *Magnetism in bcc cobalt*
by D. J. Singh
Physical Review B, Volume 45, Number 5, February 1992
- [94] *Ab initio lattice dynamics and charge fluctuations in alkaline-earth oxides*
by O. Schütt, P. Pavone, W. Windl, K. Karch, and D. Strauch
Physical Review B, Volume 50, Number 6, August 1994
- [95] *Magnetic properties of bcc Co films*
by J. A. C. Bland, R. D. Bateson, P. C. Riedi, R. G. Graham, H. J. Lauter, J. Penfold, and C. Shackleton
Journal of Applied Physics, Volume 69, Number 8, April 1991
- [96] *Band structure of bcc cobalt*
by D. Bagayoko, A. Ziegler, and J. Callaway
Physical Review B, Volume 27, Number 12, June 1983
- [97] *Ab initio wave function-based methods for excited states in solids: Correlation corrections to the band structure of ionic oxides*
by L. Hozoi, U. Birkenheuer, P. Fulde, A. Mitrushchenkov, and H. Stoll
Physical Review B, Volume 76, August 2007
- [98] *The conduction bands of MgO, MgS and HfO₂*
by P. K. de Boer and R. A. de Groot
Journal of Physics - Condensed Matter, Volume 10, 1998
- [99] *Handbook of the band structure of elemental solids*
by D. A. Papaconstantopoulos
Plenum Press, 1986
ISBN: 0-306-42338-3

- [100] *Self-consistent band structures, charge distributions, and optical-absorption spectra in MgO, α -Al₂O₃, and MgAl₂O₄*
by Yong-Nian Xu and W. Y. Ching
Physical Review B, Volume 43, Number 5, February 1991
- [101] *Reduction of electron tunneling current due to lateral variation of the wave function*
by W. H. Butler, X.-G. Zhang, T. C. Schulthess, and J. M. MacLaren
Physical Review B, Volume 63, January 2001
- [102] *Giant monolayer magnetization of Fe on MgO: A nearly ideal two-dimensional magnetic system*
by Chun Li and A. J. Freeman
Physical Review B, Volume 43, Number 1, January 1991
- [103] *Interface scattering and the tunneling magnetoresistance of Fe(001)-MgO(001)-Fe(001) junctions*
by M. E. Eames and J. C. Inkson
Applied Physics Letters, Volume 88, June 2006
- [104] *Surface x-ray diffraction analysis of the MgO/Fe(001) interface: Evidence for an FeO layer*
by H. L. Meyerheim, R. Popescu, N. Jedrecy, M. Vedpathak, M. Sauvage-Simkin, R. Pinchaux, B. Heinrich, and J. Kirschner
Physical Review B, Volume 65, April 2002
- [105] *A quasi-Newton algorithm for first-order saddle-point location*
by P. Culot, G. Dive, V. H. Nguyen, and J. M. Ghuysen
Theoretica Chimica Acta, Volume 82, 1992
- [106] *Electronic properties of Fe, Co, and Mn ultrathin films at the interface with MgO(001)*
by M. Sicot, S. Andrieu, F. Bertran, and F. Fortuna
Physical Review B, Volume 72, October 2005
- [107] *Non-equilibrium Green's function based single-band tight-binding model for Fe-MgO-Fe magnetic tunnel junction devices*
by Tehseen Raza and Hassan Raza
In preparation
Link to online document (pdf version only)
- [108] *High tunnel magnetoresistance in epitaxial Fe/MgO/Fe tunnel junctions*
by J. Faure-Vincent, C. Tiusan, E. Jouguelet, F. Canet, M. Sajjeddine, C. Bellouard, E. Popova, M. Hehn, F. Montaigne, and A. Schuhl
Applied Physics Letters, Volume 82, June 2003
- [109] *Static and dynamic aspects of spin tunnelling in crystalline magnetic tunnel junctions*
by C. Tiusan, M. Sicot, J. Faure-Vincent, M. Hehn, C. Bellouard, F. Montaigne, S. Andrieu, and A. Schuhl
Journal of Physics: Condensed Matter, Volume 18, January 2006

This is not the end. It is not even the beginning of the end. But it is, perhaps,
the end of the beginning.

- *Churchill*

Magnetoresistance in MgO-based Magnetic Tunnel Junctions with Fe, Co, and FeCo Electrodes

by
Ph.D. Student Morten Stilling

This thesis describes the work done in my Ph.D. project, performed in cooperation with the Nano-Science Center at Copenhagen University and Atomistix from May 2004 to May 2008.

Three magnetic tunnel junctions, consisting of five-layer Magnesium oxide barriers sandwiched between ferromagnetic Iron, Cobalt, or Iron-Cobalt electrodes, have been set up and optimized. The structural properties of the systems have been analyzed, and the zero-bias conductance and tunneling magnetoresistance have been calculated. The tunneling mechanisms have been examined, and the finite-bias current/voltage characteristics and tunneling magnetoresistance have been investigated.

It has been found that the tunneling magnetoresistance is very large in these systems, but that it falls off when a finite bias voltage is applied. The high values are due to differences in tunneling mechanism when the electrodes are magnetized in the same direction and when they are magnetized in opposite directions. In the Fe/MgO and Co/MgO systems the fall-off is due to a linear increase in the current with increasing bias voltage in the parallel magnetization configuration combined with a super-linear increase in the anti-parallel configuration. In the FeCo/MgO system it is due to a sub-linear increase in the parallel configuration combined with a linear increase in the anti-parallel configuration.



Ph.D. Student Morten Stilling
mortenstilling@mortenstilling.com
www.mortenstilling.com